Sapphire Ultraoptics for

Sub-meV ^{121}Sb and ^{125}Te Phonon Spectroscopy

Faculté des Sciences - Université de Liège

&

Jülich Centre for Neutron Science (JCNS-2) and Peter Grünberg Institute (PGI-4)

&

The European Synchrotron Radiation Facility

Année académique 2016-2017

Dissertation présentée par
Atefeh Jafari
en vue de l'obtention du grade de
Docteur en Sciences

*This thesis is dedicated to my Mother
for her endless love and support.*

Abstract

Nuclear resonance scattering of synchrotron radiation enables probing hyperfine interactions and element specific vibrational modes of nuclei that exhibit a Mössbauer transition. A prerequisite for this method is a monochromator with narrow bandwidth. Silicon, as the most commonly used crystal in monochromators, is not suitable for experiments above 30 keV photon energy. Using a sapphire single crystal in backscattering geometry is an alternative. An x-ray beam with narrow bandwidth can be obtained from a back-reflection with a Bragg angle of a few arcsec to a few arcmin smaller than $\pi/2$. The development of a sapphire backscattering monochromator with high energy resolution, better than 1 meV, would permit detailed lattice dynamics characterization of novel functional materials.

Sapphire is a very rigid material with desirable optical properties, high chemical resistance, and high heat conduction. Crystals of large size with high quality are of interest for many industrial applications, and suited for optics and optoelectronics operating under ambient condition or extreme conditions.

The purpose of the work in this dissertation is twofold. First, study the quality of sapphire single crystals by modern high-resolution characterization techniques in order to acquire microstructural information and thereby a better understanding of the origin of lattice defects. The second goal is the study of the lattice dynamics in materials based on tellurium and antimony with Mössbauer energies of 35.49 keV and 37.13 keV using nuclear resonance scattering with energy resolution given by one of the highest quality sapphires.

White beam topography of more than thirty crystals, grown at the Shubnikov Institute of Crystallography in Moscow, revealed qualitative information about the distribution of lattice defects of which linear defects, *i.e.* dislocations, are the majority type. The lowest dislocation density of ~ 10^2 -10^5 cm^{-2} was found in *C*-plane crystals grown by the Kyropoulos and Bridgman techniques. We carried out rocking curve imaging in backscattering geometry to estimate the lattice parameter variation and energy resolution from back-reflections. Minimum variations of the lattice parameters on the order of 10^{-8} were observed from spots with an edge length of 0.2-0.5 mm. There are a few spots with such a quality in one crystal which makes it suitable as backscattering monochromator in nuclear resonance scattering or as analyzer in resonant inelastic x-ray scattering.

The use of very high energy resolution nuclear inelastic scattering with 0.7 meV at the energy of the nuclear transition in ^{121}Sb and ^{125}Te enables valuable insight into the phonon scattering of thermoelectric materials, that convert heat to prvide electricity and vice versa, composed of Sb and Te. A careful study is done on heat carrying acoustic modes in the partial density of states of (PbTe)$_m$AgSbTe$_2$, so called LAST-*m* alloys. An impressive mismatch in the phonon group velocities in the 2-5 meV range and difference in the force constants for the Sb and Te density of phonon states is observed, a phonon mismatch predicted to be responsible for low lattice thermal conductivity in LAST-*m*.

An in-depth understanding of the element-specific dynamic properties of cubic and orthorhombic antimony trioxides was achieved using nuclear resonance scattering with an energy resolution of ~ 1 meV at the nuclear transition energy of ^{121}Sb. A softening of the Sb bonds upon transformation from cubic molecular structured in α-Sb$_2$O$_3$ to chain structured orthorhombic in β-Sb$_2$O$_3$

is observed. Furthermore, results on the lattice dynamics on α-TeO$_2$, with quasi molecular structure, demonstrate strong interatomic Te bonds, comparable with the strong bonds in molecular structured α-Sb$_2$O$_3$. The nuclear resonance data is complemented with inelastic neutron scattering data that reveals the oxygen vibrational modes. In addition, the experimental results validate the calculations of the vibrational modes in these types of materials and serve as benchmark for the calculation.

Résumé

La diffusion nucléaire résonante de rayonnement synchrotron permet de sonder les interactions hyperfines et les modes vibrationnel avec une spécificité élémentaire pour les noyaux qui possèdent une transition Mössbauer. Un prérequis pour cette méthode est un monochromateur avec une bande passante étroite. Le silicium, en tant que cristal utilisé communément pour des monochromateurs, n'est pas adapté pour des expériences avec une énergie de photon supérieure à 30 keV. L'utilisation de saphir monocristallin en géométrie de rétrodiffusion est une alternative. Un faisceau de rayons-x avec un bande passante étroite peut être obtenu d'une réflexion de Bragg à un angle de quelques secondes jusqu'à quelques minutes d'arc plus petit que $\pi/2$. Le développent d'un monochromateur saphir avec une haute résolution en énergie, meilleure que 1 meV, permettrait une caractérisation détaillée de la dynamique de réseau dans de nouveaux matériaux fonctionnels.

Le saphir est un matériau très rigide avec des propriétés optiques intéressantes, une grande résistance chimique et une très bonne conductivité thermique. Des cristaux de grande tailles et de bonne qualité sont intéressants pour de nombreuses applications industrielles et sont adaptés pour des optiques et des optoélectroniques sous conditions ambiantes ou conditions extrêmes.

L'objectif du travail présenté dans cette dissertation est double. Le premier objectif est d'étudier la qualité de monocristaux de saphir par des techniques modernes à haute résolution afin d'obtenir une information microstructurale et donc une meilleure compréhension de l'origine des défauts de maille. Le second objectif est l'étude de la dynamique de réseau de matériaux composés de tellure et d'antimoine par diffusion nucléaire résonante aux énergies Mössbauer de 35.49 keV et 37.13 keV avec une résolution en énergie fournie par un de saphir de meilleur qualité disponible.

La topographie en faisceau blanc de trente cristaux, dont la croissance fut réalisée à l'Institut Shubnikov de Cristallographie, Moscou, fournit des informations qualitatives sur la distribution de défauts de maille, dont les défauts linéaires, des dislocations, sont le type majoritaire. La concentration de dislocations la plus faible est de ~10^2 -10^5 cm^{-2} dans des cristaux de plan-C obtenus par croissances de type Kyropoulos et Bridgman. Nous avons utilisé l'imagerie de courbes de réflectivité en géométrie de rétrodiffusion pour estimer les variations de paramètres de maille et la résolution en énergie des retro-réflexions. Des variations relatives minimales des paramètres de maille de l'ordre de 10^{-8} ont été observées pour des régions avec des côtés de 0.2-0.5 mm. Quelques régions de hautes qualité sont observées dans un cristal, ce qui le rend utilisable comme monochromateur pour la diffusion nucléaire résonante ou comme analyseur pour la diffusion résonante inélastique de rayons-x.

L'utilisation de la diffusion nucléaire inélastique avec une résolution de 0.7 meV pour les transitions nucléaires de ^{121}Sb et ^{125}Te permet d'obtenir des informations précieuses sur les mécanismes de diffusion de phonons dans des matériaux thermoélectriques contenant de l'antimoine ou du tellure, qui convertissent la chaleur en électricité et vice-versa. Nous avons conduit une étude détaillée des modes acoustiques conducteurs de chaleur dans les densités d'états de phonons partielles de (PbTe)$_m$AgSbTe$_2$, appelés alliage LAST-m. Les vitesses de groupes des phonons dans la gamme de 2-5 meV et les constantes de forces sont inégales de façon impressionnante pour Sb et Te, une inégalité de vitesse de phonons qui avait été prédite comme

étant responsable de la faible conductivité thermique dans LAST-*m*.

Nous avons obtenu une compréhension détaillée des propriétés dynamique, avec une spécificité élémentaire, pour les formes cubique et orthorhombique du trioxyde d'antimoine par diffusion nucléaire résonante avec une résolution en énergie de ~ 1 meV pour la transition nucléaire de ^{121}Sb. Nous observons un assouplissement des liaisons de Sb lors de la transformation depuis le cristal moléculaire cubique α-Sb$_2$O$_3$ vers la structure en chaine orthorhombique de β-Sb$_2$O$_3$. De plus, les résultats sur la dynamique de réseau dans α-TeO$_2$, avec une structure quasi-moléculaire, démontrent la présence de liaisons interatomiques fortes, comparables aux liaisons dans le cristal moléculaire α-Sb$_2$O$_3$. Les données de résonance nucléaire sont complétées par des données de diffusion inélastiques de neutrons qui permettent de visualiser les modes vibrationnels de l'oxygène. Nos résultats expérimentaux valident les calculs de modes vibrationnels et servent de jauge pour ces calculs.

Kurzbeschreibung

Resonante Kernstreuung mit Synchrotronstrahlung erlaubt Untersuchungen zur Hyperfeinwechselwirkung und zu den dynamischen Eigenschaften von Proben mit Mössbauerkernen. Voraussetzung für solche Experimente ist für gewöhnlich ein Monochromator mit exzellenter Energieauflösung. Silizium Einkristalle werden meistens zur Monochromatisierung von Synchrotronstrahlung benutzt. Oberhalb Energien von 30 keV werden sie jedoch weniger effektiv als Saphireinkristalle in Rückstreugeometrie. In dieser Anordnung, mit einem Braggwinkel nahe 90°, können mit ihnen Energieauflösungen kleiner als 1 meV und hohem Durchsatz erreicht werden. Damit eröffnet sich die Möglichkeit, detaillierte Untersuchungen zur Gitterdynamik von neuen funktionellen Materialien durchzuführen.

Saphir ist ein sehr hartes und beständiges Material mit wünschenswerten optischen Eigenschaften, großer chemischer Widerstandskraft und hoher Wärmeleitfähigkeit. Große Kristalle mit hervorragender Qualität sind für viele industrielle Anwendungen interessant wie zum Beispiel für optische und optoelektronische Anwendungen unter atmosphärischen und extremen Bedingungen.

Diese Doktorarbeit hat zwei Schwerpunkte. Zum einen stehen Untersuchungen zur Qualität von Saphireinkristallen mit modernen hochauflösenden Charakterisierungtechniken im Fokus um mikrostrukturelle Informationen zu sammeln und damit ein besseres Verständnis zum Entstehen von Gitterstörungen zu erlangen. Zum anderen wurden Untersuchungen mit Hilfe resonanter Kernstreuung zur Gitterdynamik neuer funtioneller Materialen basierend auf Tellur- und Antimonverbindungen durchgeführt. Dazu wurden Saphireinkristalle mit höchster Qualität zur Monochromatisierung der Synchrotronstrahlung bei den Energien der entsprechenden Mössbauerübergänge des Tellur (35.49 keV) und Antimon (37.13 keV) eingesetzt.

Weißlicht-Topographie von mehr als dreißig Kristallen, gezogen im Shubnikov Institute of Crystallography in Moskau, liefert qualitative Informationen über die Verteilung der Gitterstörungen, dabei treten lineare Versetzungen am häufigsten auf. Die geringste Versetzungsdichte von etwa $10^2 - 10^5$ cm^{-2} wurde in "C-Schnitt Kristallen" gefunden, die mit der Kyropoulos- und Bridgman-Technik hergestellt wurden. Zur Bestimmung der Variation der Kristallparameter und der Energieauflösung führten wir "Rocking-Kurven Bildgebung" Messungen in Rückstreugeometrie durch. Die kleinsten Änderungen der Kristallparameter, in der Größenordnung 10^{-8}, wurden in Bereichen zwischen 0.2 und 0.5 mm Kantenlänge gefunden. Es gibt einige solcher Bereiche in einem Kristall, die für Rückstreumonochromatoren für resonante Kernstreuung und als Analysator für unelastische resonante Röntgenstreuung geeignet erscheinen.

Zur Untersuchung der Phononenstreuung in thermoelektrischen Materialien, basierend auf Sb und Te, wird eine hohe Energieauflösung (~ 0.7 meV) bei den Übergangsenergien der Mössbauerkerne ^{121}Sb und ^{125}Te benötigt. Diese Materialien konvertieren Wärme in Elektrizität oder umgekehrt. Eine detaillierte Untersuchung der akustischen Moden in der Phononenzustandsdichte, verantwortlich für den Wärmetransport, wurde für die LAST-Legierung $(PbTe)_m AgSbTe_2$ durchgeführt. Deutliche Unterschiede in den Phonon-Gruppengeschwindigkeiten im Bereich 2-5 meV und der Kraftkonstanten für Sb und Te

wurden beobachtet. Es wurde vorhergesagt, dass diese Unterschiede für die geringe Gitter-Wärmeleitfähigkeit der LAST-m Legierungen verantwortlich seien.

Ein umfassendes Verständnis der elementspezifischen dynamischen Eigenschaften der kubischen und orthorhomischen Antimontrioxide konnte erreicht werden unter Ausnutzung der resonanten Kernstreuung mit einer Energieauflösung von etwa 1 meV im Fall von ^{121}Sb. Ein Weichwerden der Antimonbindung wurde beim Übergang von der kubischen Molekularstruktur in α-Sb$_2$O$_3$ zu der orthorhombischen Kettenstruktur in β-Sb$_2$O$_3$ beobachtet. Weiterhin weisen die elementspezifischen mittleren Kraftkonstanten auf stärkere Antimonbindungen in α-Sb$_2$O$_3$ als in β-Sb$_2$O$_3$ hin. Die Ergebnisse zur Gitterdynamik in α-TeO$_2$ mit einer quasi-molekularen Struktur zeigen starke interatomische Tellurbindungen, vergleichbar mit denen in der Molekularstruktur von α-Sb$_2$O$_3$. Die resonanten Kernstreudaten wurden ergänzt mit unelastischen Neuronenstreudaten, welche Zugang zu den Sauerstoffschwingungsmoden erlauben. Letztendlich halfen theoretische Berechnungen der Vibrationsmoden bei der Zuordnung der gemessenen Moden. Unsere Daten dienten als Bezugsgröße für diese Rechnungen.

Реферат

Ядерное резонансное рассеяние синхротронного излучения предоставляет возможность исследований сверхтонкого взаимодействия и колебательных состояний ядер с Мессбауэровскими ядерными переходами. Для того чтобы проводить данные исследования, требуются монохроматоры с узкой энергетической полосой пропускания. Наиболее распространённым кристаллом для монохроматоров является кремний. Однако, он непригоден для экспериментов с фотонами, энергия которых лежит выше 30 кеВ. Альтернативой кремнию является использование кристаллов сапфира в геометрии обратного рассеяния. Геометрия обратного рассеяния с углом Брэгга отличающимся от $\pi/2$ на несколько угловых секунд или угловых минут позволяет получить рентгеновские пучки с узкой энергетической полосой. Разработка сапфирового монохроматора обратного рассеяния с высоким – лучше чем 1 мэВ – энергетическим разрешением позволила бы проводить подробные исследования атомной динамики новых функциональных материалов.

Сапфир является очень жёстким материалом, с хорошими оптическими свойствами, высокой химической инертностью и высокой теплопроводностью. Большие и высококачественные кристаллы сапфира представляют интерес для многих приложений в индустрии, а также для оптики и оптоэлектроники, как в нормальных, так и в экстремальных условиях.

Работа изложенная в данной диссертации имеет две цели. Это, во-первых, изучение качества монокристаллов сапфира современными методами исследования с высоким разрешением для получения микро-структурной информации и, таким образом, для более полного понимания причин вызывающих дефекты кристаллической решетки. Второй целью работы являются исследования атомной динамики материалов на основе теллура и сурьмы с Мессбауэровскими ядерными переходами с энергией 35.49 кэВ и 37.13 кэВ, соответственно, используя ядерное резонансное рассеяние с энергетическим разрешением, получаемым при использовании одного из самых высококачественных кристаллов сапфира.

Работы по рентгеновской топографии с использованием рентгеновского излучения с широким энергетическим спектром, проведённые с более чем тридцатью кристаллами сапфира выращенными в Институте Кристаллографии им. Шубникова позвлили получить качественную информацию о распределении в кристаллах дефектов, большинство из которых являются линейными дефектами, то есть – дислокациями. Наименьшая – порядка 10^2-10^5 см$^{-2}$ – плотность дислокаций была получена для С-срезов кристаллов выращенных методами Киропулоса и Бриджмана. Используя метод визуализации параметров кривых качаний в геометрии обратного рассеяния, нам удалось провести количественные оценки распределения параметров кристаллической решетки и получаемого энергетического разрешения. Наиболее узкое – порядка 10^{-8} – распределение параметров кристаллической решетки было зарегистрировано для небольших участков поверхности с поперечным размером около 0.2 – 0.5 мм. На одном из кристаллов было выявлено несколько участков данного качества, что позволяет использовать этот кристалл в качестве монохроматора обратного рассеяния для экспериментов по ядерному резонансному рассеянию, либо в

качестве анализатора в экспериментах по резонансному неупругому рассеянию рентгеновских лучей.

Эксперименты по ядерному неупругому рассеянию с очень высоким – 0.7 мэВ – энергетическим разрешением с использованием ядерных переходов в ^{121}Sb и ^{125}Te позволили получить важную информацию о рассеянии фононов в термоэлектрических материалах – материалах конвертирующих тепло в электричество и наоборот – состоящих из Sb и Te. Было проведено тщательное исследование аккустических мод – то есть, мод, наиболее ответственных за перенос тепла – в парциальных плотностях фононных состояний образца $(PbTe)_mAgSbTe_2$, известного также под названием "LAST"-сплав. В частности, для фононов с энергиями 2-5 мэВ, была выявлена значительная разница в групповых скоростях и силовых константах для Sb- и Te-парциальных плотностей фононных состояний. По современным представлениям, именно эта разница в групповых скоростях считается ответственной за низкую теплопроводность "LAST"-сплава.

В работах по ядерному неупругому рассеянию с энергетическим разрешением около 1 мэВ с использованием ядерного перехода в ^{121}Sb и ^{125}Te было достигнуто хорошее понимание динамики атомных колебаний для разных элементов составляющих кубическую и орторомбическую решетки триоксида сурьмы. Полученные данные по средним силовым константам указывают на то, что при переходе из молекулярной кубической структуры α-Sb_2O_3 в цепочечную орторомбическую структуру β-Sb_2O_3 наблюдается смягчение химических связей сурьмы. Кроме того, результаты по исследованию атомной динамики образца α-TeO_2 с квази-молекулярной структурой указывают на сильные химические связи, сравнимые связями в образце α-Sb_2O_3 с молекулярной структурой. Помимо понимания атомной динамики исследованных образцов, результаты полученные в данной работе имеют также большое значение для анализа компютерных расчетов атомной динамики.

Acknowledgements

Mehdi, Fariba, Hadi, and Mehrnoosh for their emotional support and helping in whatever they could no matter what path I choose.

Contents

Chapter 1

1

Introduction

1.1 General Introduction

1.1.1 Nuclear resonance scattering of x-rays with sub-meV resolution

Nuclear resonance scattering (NRS) of synchrotron radiation provides very useful information on hyperfine interactions and vibrational dynamics of materials containing at least one of the so-called Mössbauer active isotopes [1–3]. The NRS takes advantage of the discovery of the recoilless emission of gamma rays by radioactive nuclei in crystalline solids, and the subsequent absorption of the emitted rays by other nuclei of the same type, referred to as the Mössbauer effect. The radioactive source in conventional Mössbauer spectrsocopy is substituted by the pulsed synchrotron radiation in NRS, more details on these techniques will be given later in this chapter.

NRS experiments using synchrotron radiation date back to the late 20th century, when the first successful experiment has been carried with 14.4 keV radiation and an ^{57}Fe enriched sample [4]. Since then, this technique has been applied to various fields like physics, chemistry, and geophysics with a rapidly growing literature. A comprehensive review of NRS is presented in Ref. [3].

NRS requires a third generation synchrotron radiation source which provides a high quality of radiation, called brilliance, which is expressed by:

$$\text{brilliance} = \frac{\text{flux}}{\text{angular spread of radiation} \times \text{size of electron beam} \times 0.001\text{BW}} \quad , \quad (1.1.1)$$

where BW is the radiation bandwidth in energy units. In order to get high brilliance, a small source size with a small beam divergence is needed. In third generation synchrotron sources, special arrays of magnets called insertion devices, mainly undulators, are used to achieve high brilliance and low emittance of the beam. The ESRF was the first third-generation hard x-ray sources to be constructed and has been operated since 1994 [5–7].

NRS, with great benefits of brilliance, polarization and time structure of the radiation from the third generation synchrotron source, enables us to investigate the elastic and inelastic scattering from samples. Elastic nuclear scattering, for example, the nuclear forward scattering (NFS) technique, measures hyperfine interactions [3], whereas the nuclear inelastic scattering (NIS) method probes the vibrational dynamics of specific atoms and yields the partial density of phonon states (DPS) for the Mössbauer nuclei [1, 2].

The first NIS experiments with ^{57}Fe have been done with a resolution of ~ 6 meV in 1995 [8, 9].

Since, then the resolution has been improved to better than 1 meV [10]. NIS measurements with [57]Fe and [119]Sn isotopes are the most common experiments at a NRS beamline. In contrast, to the best of our knowledge, there is only little of knowledge of the lattice dynamical and thermodynamical properties of materials composed of other Mössbauer isotopes such as Sb and Te, which are the subject of this thesis. This lack is due to the limited performance of the available monochromators in NIS. Clearly, there is a huge number of materials bearing Sb or Te that are widely used in industrial applications and also could be of interest for scientists.

The monochromator is the part of the NIS setup that reduces the bandwidth of the synchrotron radiation by using crystal reflections according to Bragg's law. Bragg's law provides the condition for diffraction of a wave by a family of lattice planes. In the kinematical theory of diffraction, it is described by the well know equation $2d\sin(\theta) = n\lambda$, where n is a positive integer, d is the interplanar spacing, λ the x-ray wavelength, θ the angle of the incident wave, see Fig.1.1a. In this approximation, the incoming photons are assumed to be only scattered once and the so called the multiple scattering is not considered. The spectral reflectivity curve is Dirac's delta function. The dynamical theory, with consideration of the interactions between the diffracted waves and the crystalline matter, reveals a different shape of the reflectivity curve with finite width, called the Darwin width (ω_D), see Fig.1.1b.

From a derivative of Bragg's law in the dynamical theory of x-ray diffraction, the relative energy resolution $\delta E/E$ is obtained by the relation [11]:

$$(\frac{\delta E}{E})^2 = (\frac{\delta d}{d})^2 + (\delta\theta_{app}^2 + \omega_D^2)cot^2\theta, \tag{1.1.2}$$

where ω_D is the Darwin width (i.e. the angular acceptance) and $\delta d/d$ is the lattice parameter variation that is related to the perfection of the crystal, $\delta\theta_{app}$ is the beam angular divergence which is the angular divergence of the beam emitted by source, possibly modified by any optics before the crystal [12]. Obviously, the Darwin width must be larger than the angular divergence of the incident beam to obtain the maximum reflectivity.

By replacing the interplanar spacing in the Bragg equation with the Miller indices (h, k, l), and the unit cell dimension (a) e.g. for a cubic structure, we get:

$$\sin\theta = \frac{\lambda}{2a}(h^2 + k^2 + l^2)^{1/2}. \tag{1.1.3}$$

The high-order refections minimize the Darwin width and as described by Eq.1.1.2 and Eq.1.1.3, results in high energy resolutions. Also, an asymmetrically cut crystals has a small Darwin width [13], hence using reflections of high quality crystals such as silicon or germanium with this condition fulfils the requirements for high energy resolution for energies less than 30 keV. However, for higher energies, this approach becomes inefficient because the Darwin widths of the high-order reflections become very small [14]. An alternative monochromatization scheme based on a single high-order Bragg reflection in backscattering geometry (Fig.1.1c) can be used [15, 16]. The energy bandwidth of the reflections with Bragg angles close to $\pi/2$ reaches its smallest value, while the angular width is at the maximum, as shown in Fig.1.1d.

(a)

$0° < \theta < 90°$

λ

θ 2θ

d (d_H)

dsinθ dsinθ

(c)

$\theta \sim 90°$

θ

d_e

N_e reflecting planes

(b)

1

0

Reflectivity

Darwin reflectivity curve

FWHM:
Darwin width

0

$\theta - \theta_B$

(d)

10

$\frac{E}{E_H}$

$\Delta E/E_H$

1

0

90

θ [degrees]
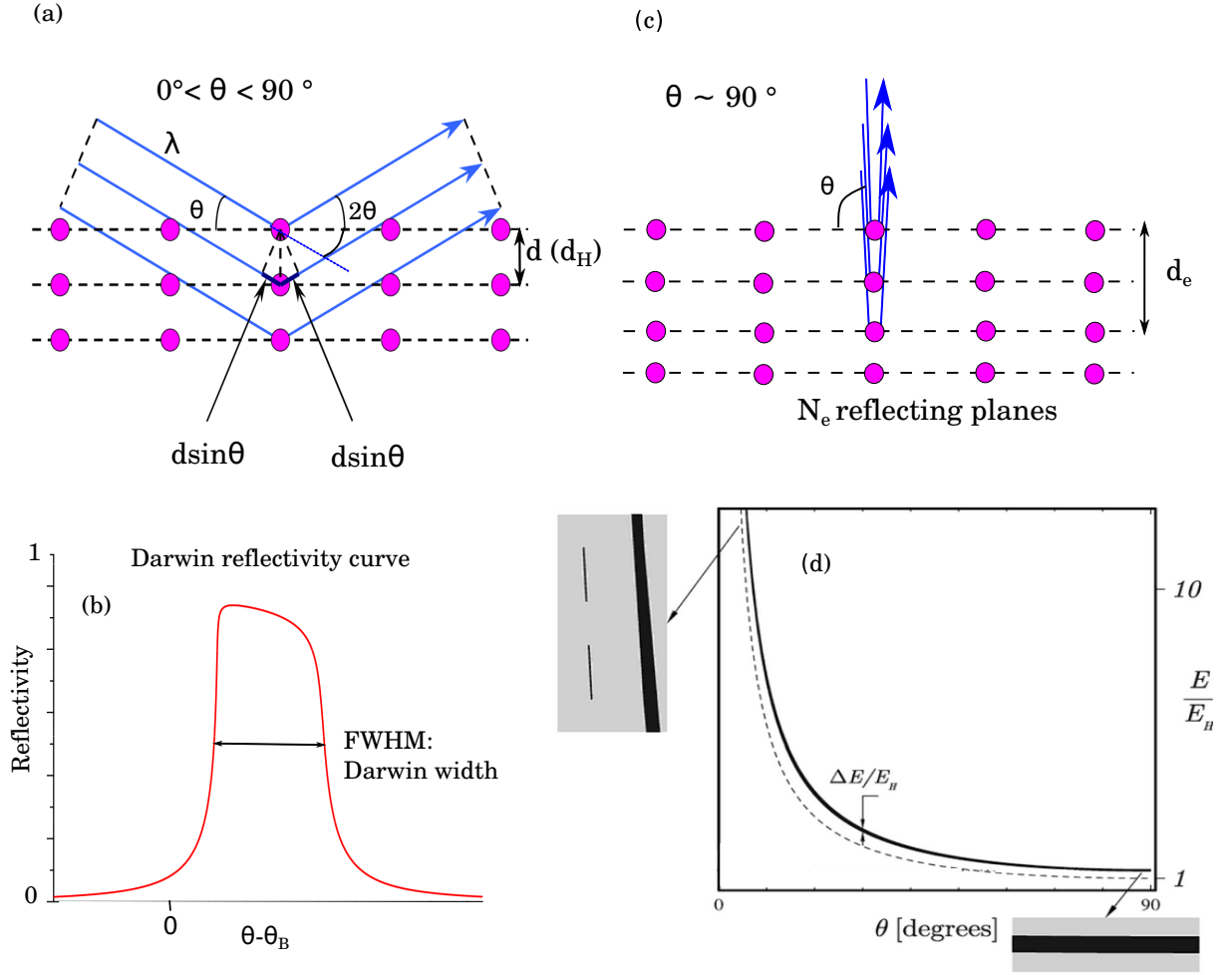
Figure 1.1: (a) Schematic description of Bragg's diffraction law. Light (x-rays) reflected from adjacent crystal planes will undergo constructive interference only when the path difference between them is an integer number of the wavelength of the incident beam. (b) The Darwin (reflectivity) curve used in the dynamical approximation. The deviation from the Bragg angle θ_B is due to the refraction effect, which is neglected in kinematical approximation.(c) Bragg backscattering occurs when the angle between the incident beam and the normal (θ) to the atomic plane is $\sim 90°$. This is near-backscattering and forms so called back reflections. In this figure the extinction length (N_e numbers of reflecting atomic planes $\times d$) is smaller than the thickness of the crystal. (d) A plot of crystal peak reflectivity for x-rays versus incident angle (0°-90°) in the symmetric Bragg scattering geometry. The dashed line and solid line present the results corresponding to Bragg's law under kinematical and dynamical conditions, respectively. The relative spectral width $\Delta E/E_H$, where E is the energy of x-ray photons and E_H is the Bragg energy, is constant under kinematical conditions. On the contrary, it varies under dynamical conditions and it becomes largest and constant when θ is close (or equal) to 90°, from Ref.[17].

The high resolution monochromator also prevents overloading of the electronics and detectors in the time-resolved NFS technique. The bandwidth of the radiation after the high heat load monochromator (HHLM) is reduced to eV-range. Under those conditions, 10^{14} photons per second at the ^{57}Fe energies and 10^6-10^9 at higher energy will be obtained. This number of photons per second can easily overload the silicon avalanche photo-diodes detector, APD [18]. Thus, using x-rays with (sub-) meV energy bandwidth in a NFS measurement is strongly recommended to reduce the number of non-resonant photons, *i.e.* to keep the parasitic radiation reaching the sample as low as possible.

1.1.2 Choice of crystals for hard x-ray optic

The density of Bragg back reflections, see Fig 1.2b, from silicon or germanium is small due to their high symmetry crystal structures. Consequently, the gap between the Bragg energy of reflections and nuclear resonance energies (in particular those higher than 30 keV) is too big to be reduced enough by cooling or heating the crystal. Conversely, crystals with lower symmetry offer many possible reflections with abundant choices of intrinsic resolutions. White sapphire (α-Al$_2$O$_3$), lithium niobate (LiNbO$_3$), silicon carbide (SiC), gallium nitrite (GaN), and quartz (α-SiO$_2$) are several crystals with a lower symmetry as compared to silicon and germanium.

Fig.1.2 presents a map of reflections for some of these single crystals. In the top panel, the energy resolutions for near backscattering reflections from 4 to 13 keV are depicted (figure adopted from [19]). The map indicates that sapphire and lithium niobate offer high-resolution reflections at high energies. In addition, the energy resolution of silicon and sapphire at room and low temperature have been compared in the energy range of 0-50 keV, shown in the bottom panel in the same figure. All these calculated results demonstrate promising properties such as high reflectivity, small energy resolution, and large variety of choices of reflection in sapphire as compared to the most common used crystal monochromator (that is mainly silicon), particularly at high energy.
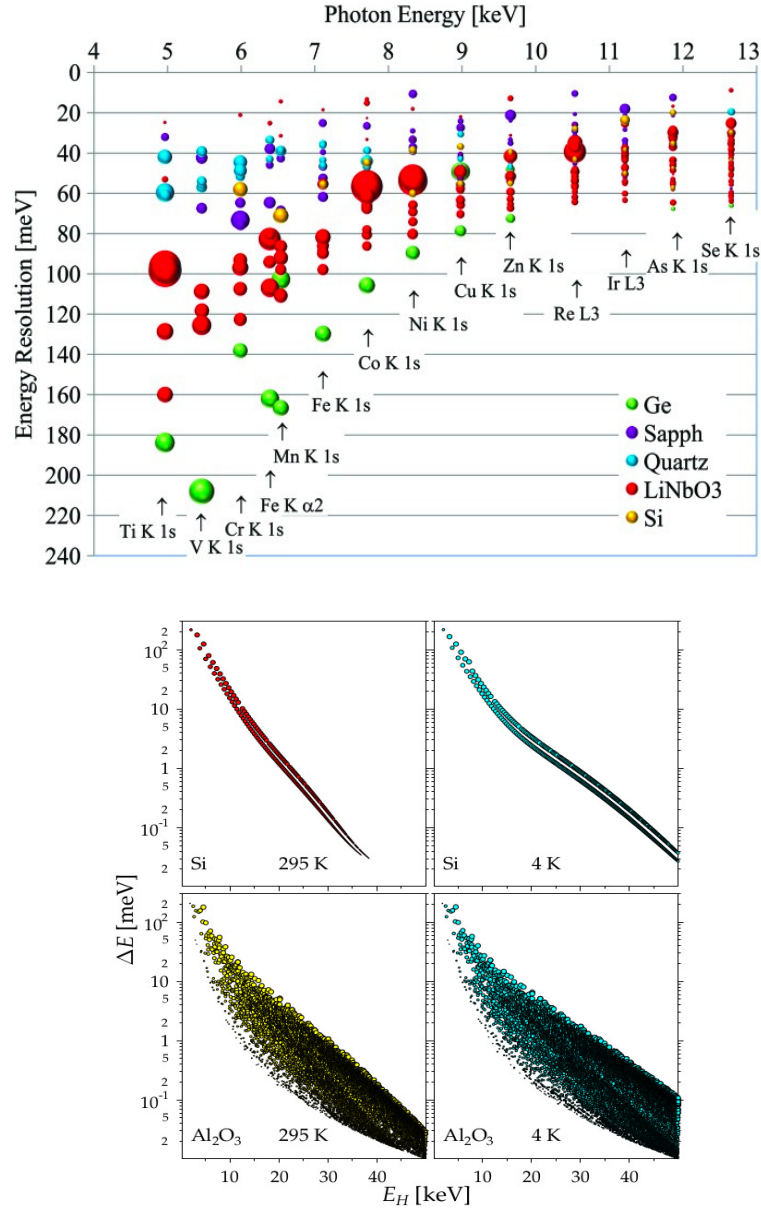
Figure 1.2: (Top) Map of the intrinsic energy resolution of near-backscattering reflections between 4 and 13 keV in several single crystals, from Ref. [19]. (Bottom) Comparison of the energy resolution of the backscattering reflections in the range of 0 to 50 keV and reflectivity larger than for silicon (Si) and sapphire (α-Al$_2$O$_3$) at low and room temperatures [17].The size of the symbols in all maps is proportional to the integrated reflectivity.

The small atomic displacements in sapphire lead to a high Debye temperature $\Theta_D \simeq 1200 K$ and a high Debye-Waller factor, $exp(-2W)$. As a result, sapphire diffracts hard x-rays with high effective reflectivity. Moreover, sapphire presents a large number of back reflections [17]. Interestingly, many of these reflections have an intrinsic energy bandwidth of sub-meV. According to calcula-

tions, a perfect sapphire provides a reflectivity of about 90 % up to 40 keV at room temperature. Silicon does not give the same reflectivity for energies above 25 keV even at low temperature [17].

On the one hand sapphire has many interesting features, but on the other hand there is no available perfect sapphire. Assuming the symmetric diffraction geometry, the spectral width of the reflection, ϵ_H, is related to the number of reflecting planes (N_e, e denotes the extinction) according to [17]:

$$\epsilon_H = d_H/\pi d_e = 1/\pi N_e, \qquad (1.1.4)$$

where d_H and d_e are interplanar spacing and the extinction length, respectively. The extinction length is the required physical distance where exp(-1) of the intensity of the incident beam is transferred to the Bragg reflected beam. For high-order reflections, the interplanar spacing is small and the extinction length is large, thereby a small spectral width can be obtained in a perfect crystal with a thickness of at least one extinction length.

In backscattering geometry, the relative energy bandwidth $\delta E/E$ is given by variations in lattice spacing, $\delta d/d$, so in order to reach a resolution better than 1 meV for 10-100 keV, a crystal with lattice spacing variation of $< 10^{-7}$-10^{-8} is required.

According to this model, a 2 mm thick perfect sapphire crystal can provide a resolution of 0.39 meV at the ^{121}Sb nuclear resonance energy, 37.1292 keV. Up to now the best available sapphire crystal gives a bandwidth of $\sim$ 1 meV [20]. This crystal has 1 mm thickness with a $\sim 300 \times 300$ μm^2 nearly perfect area. It is used in the monochromator at the nuclear resonance beamline ID18 [21] of the European Synchrotron Radiation Facility (ESRF). It should be taken into account that not only the number of perfect lattice planes or crystal thickness has an impact on the resolution but also the size of the perfect area is important.

1.1.3 On the growth of large perfect sapphire

Synthetic ruby or white (*i.e.* corundum) sapphire has being produced for more than a century using various growth techniques. Some of these well-known techniques will be introduced here. The Verneuil process, also called flame fusion, is the oldest growth method named after a French chemist, Auguste Verneuil. The first report on his work together with Frémy was published in 1891 [22]. In this technique, the burned feed material falls on the surface of an oriented seed and is crystallized, see Fig.1.3 a. This technique is still widely used for the industrial applications and is regarded as the father of synthetic corundum.

The principles of nucleation and growth control of the Verneuil method have been applied to the other growth techniques. The Bridgman technique is the second oldest method which was introduced in the USA by two physicists, Percy Williams Bridgman and Donald C. Stockbarger [23, 24]. The growth process can be performed either vertically or horizontally [25, 26]. The latter is known under another name, called Horizontal Directional Solidification Method, HDSM. It was pioneered by Bagdasarov in Moscow in the early 1970s [27] and is also widely employed. In these techniques, a melted zone is created between the seed crystal and the raw materials, it solidifies when the container is slowly moved out of the hot zone. The process can be carried out in a horizontal direction (in HDSM) or vertical direction (in Bridgman method), as shown in insets (b) and (c), respectively.

The Kyropoulos growth method of sapphire was named after Spyro Kyropoulos who introduced

this technique in 1926 [28]. This technique has been further developed by M. I. Musatov in the 1970s in St. Petersburg [29]. The molten liquid obtained from alumina powder is in a crucible and is attached to the seed crystal where at this contact area the crystallization starts initially. After a short pulling sequence during the seeding stage of the process, the temperature of the hot zone decreases very slowly, then thermal gradient controls the process of crystallization out of the melt, see inset (d). An example of a boule (large size crystal) grown by the Kyropoulos method is shown in Fig.1.3-e, from which crystals (wafers) were cut out. Examples of a few crystals are shown in inset (f). Because of its capability of growing single crystals with high quality, nowadays, a large number of the world's sapphire are produced by the Kyropoulos method [30]. In the literature, there are good reviews of crystal growth modelling for understanding the heat transfer, flow pattern, and thermal stress distribution in crystal growth processes such as Verneuil [31], Bridgman [32], HDSM [33], and Kyropoulos [34].
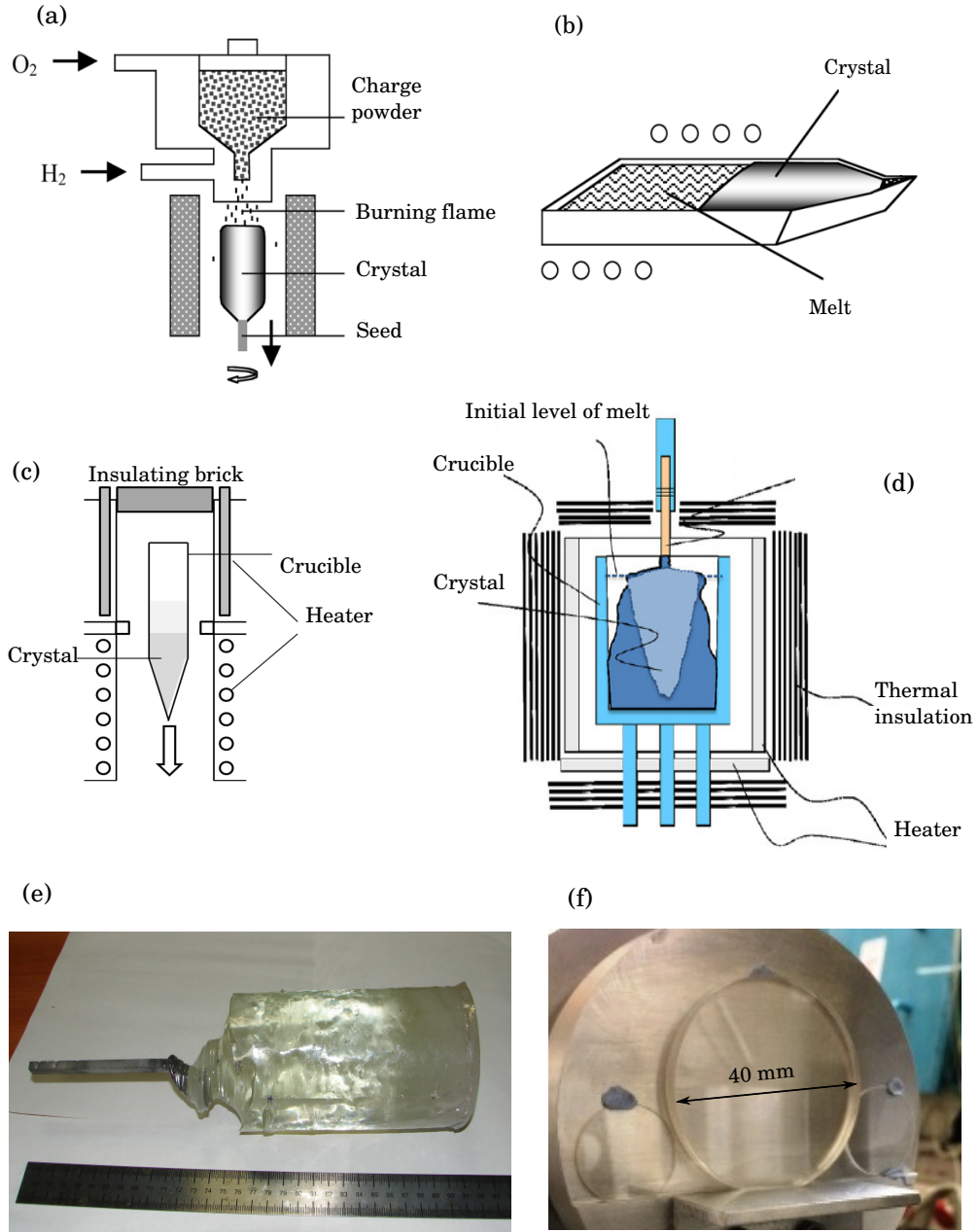
Figure 1.3: Schematic presentation of several sapphire growth techniques: (a) Verneuil, (b) horizontal solidification method, pictures taken from Ref. [35], (c) Bridgman, and (d) Kyropoulos, pictures taken from Ref. [36]. (e) An example of a Kyropoulos grown boule. (f) Three sapphire crystals were cut from different boules.

1.1.4 Motivation: An example of application of sub-meV monochromator

In this study we will investigate the interesting behaviour of the low-energy phonons in $AgSbTe_{18}Pb_{20}$, known as LAST-18 alloy, by using NIS with sub-meV resolution. LAST-18 alloys consist of Ag- and Te-rich matrix and Sb-rich secondary phases embedded in the matrix [37]. For long time, it was believed that the very low lattice thermal conductivity of this material is caused

by the presence of nanoprecipitates within the matrix. This idea was suggested on the basis of the calculated Density of Phonon States DPS of PbTe matrix and AgSbTe$_2$ nanoprecipitate [38]. NIS is the only experimental technique which gives the element specific DPS and can either confirm or reject the proposed idea from the point of view of the phonons. It is important to mention that this kind of the isotope-selectivity studies are nearly impossible with neutron scattering, because the scattering cross-section of Sb is very small in comparison to Pb and Te. In addition, the amount of Sb in this alloy is too small (~ 3.5 %) to be clearly detectable in Inelastic Neutron Scattering (INS) [39].

The first partial DPS of LAST-18 for ^{121}Sb and ^{125}Te has been obtained experimentally using NIS by P. B. Pereira in 2011 [40]. But data below 3 meV were not reliable because of the finite energy resolution, therefore phonon behaviour at low energy remained unclear. They determined a range of possible Debye levels (I and II in Fig. 1.4) from the low energy regions in the reduced DPS, $g(E)/E^2$ of ^{121}Sb. The Debye level is the contribution of sound (acoustic) modes to $g(E)/E^2$ calculated within the Debye model. We report the measurement with a better energy resolution and determine which of their estimated Debye levels is correct. The results will be shown and discussed in Chapter 4.
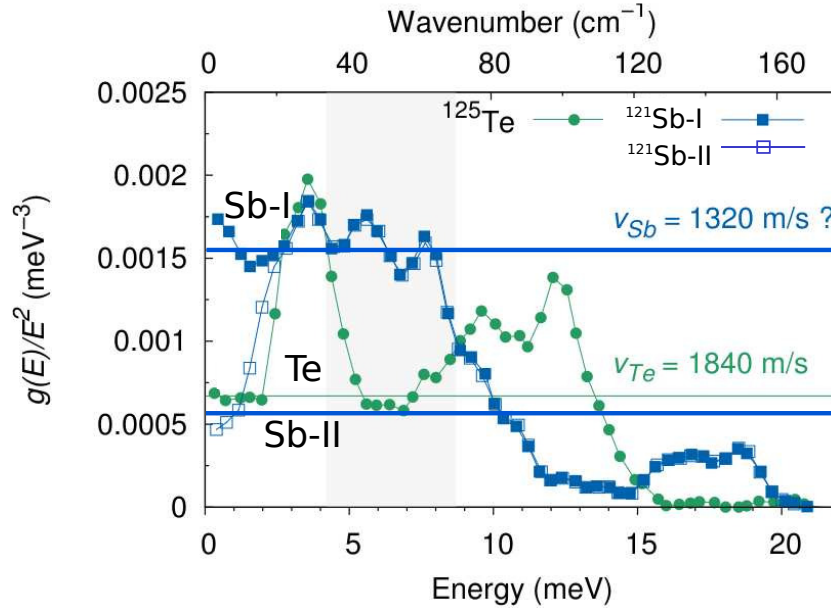
Figure 1.4: The reduced partial DPS, $g(E)/E^2$, of AgSbTe$_{18}$Pb$_{20}$, together with the estimated Debye levels. Data were collected using the monochromator with the energy resolutions of 1.3 and 1.1 meV for ^{121}Sb and ^{125}Te, respectively [20]. From the low energy region of $g(E)/E^2$ for ^{121}Sb, two possible Debye levels for the Sb contribution can be extracted: one is higher than the ^{125}Te Debye level (estimated from Sb-I) and another very close to it (estimated from Sb-II). In this particular study, estimation of the Debye level is very sensitive to the subtraction of the elastic line from the inelastic scattering data. From Ref. [40].

1.1.5 Thesis structure

In this first chapter, the experimental techniques used in this investigation will be introduced. Chapter 2 outlines the general assessments of quality crystals evaluated by white beam topography. Several crystals have been selected for further investigations from the results discussed in Chapter 2. Chapter 3 presents a quantitative analysis of the selected sapphires. Chapter 4 is concerned with lattice dynamics of $AgPb_{18}SbTe_{20}$ alloy. Chapter 5 is dedicated to the studies of vibrational properties and lattice dynamics of antimony and tellurium oxide. Chapter 6 is a brief conclusion which draws together the insights gained from the work.

1.2 Experimental Methods

The characterization of nearly perfect crystals is crucial for understanding the source and the type of defects. X-ray topography is the term used for a family of x-ray imaging techniques based on Bragg diffraction of x-rays in the crystal lattice. It can be performed using either characteristic radiation from laboratory x-ray source [41, 42] or synchrotron radiation sources [43, 44]. This method is used for the visualization of defects such as twins, dislocations, impurity distribution, and inclusions.

1.2.1 White beam topography

White beam topography is a nondestructive characterization technique by means of x-ray diffraction. The theory of x-ray topography can be explained by the dynamical theory of x-ray diffraction. A detailed description of the technique and theory is provided in Refs. [11, 45, 46]. Fundamentally, white beam topography is analogous to the classical Laue x-ray diffraction method. Out of a broad continuous spectrum containing x-ray energies from about 6 keV up to 100 keV, the lattice planes of a single crystal select the matching wavelengths λ that fulfil the condition for Bragg's law, $n\lambda = 2d\sin\theta_B$, where θ_B is the Bragg angle. A particular set of planes which fulfil the Bragg condition result in one topograph, also called the Laue spot. The Laue spot from various reflections can be collected on a photographic film or a Charge-Coupled Devices (CCD) camera, during a single exposure of a few seconds using synchrotron radiation. A well collimated synchrotron beam results in sharp and high resolution images.

The sample can be illuminated in either transmission geometry (known as Laue case) or in a reflection geometry (known as Bragg case). In this work we used white beam topography in transmission geometry in order to reveal the bulk micro-structure of the crystals. A schematic of the experimental arrangement for white beam transmission topography is shown in Fig.1.5a. A Laue spot from a perfect crystal is completely homogeneous in intensity. In crystals with angular misalignment of atomic planes (misorientation), the parallel incident beam is diffracted with some divergence, see Fig.1.5b. This divergence causes a non-homogeneous intensity distribution, called contrast. Note that contrast does not reveal the defects themselves, but rather the lattice deformations or strain field surrounding the defects.

There are two main mechanisms for contrast formation, the first type is called orientation contrast and the second is called extinction contrast. Orientation contrast can be explained by applying Bragg's law. If the misorientation caused by a defect is larger than the divergence of the incident

(a)

Laue spots

Detector or Film

Synchrotron beam

Sample

Beam stop

(b)

Defect

Diffracted beam

Contrast due to defect

One Laue spot

Direct beam

Illuminated piece
of a sample contaning
a defect
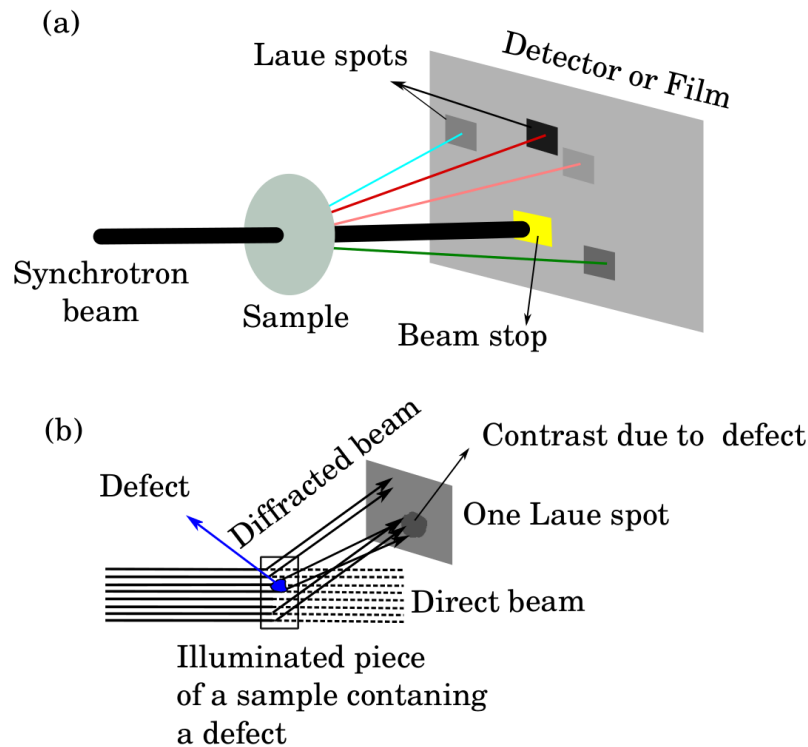
Figure 1.5: (a) Schematic setup for white beam topography in transmission geometry, *i.e.* in the Laue case. Synchrotron radiation with a continuous spectrum (white beam) transmitted through the sample is diffracted by sets of atomic planes, which match the Bragg condition for a particular wavelengths. The diffracted beams form several topographs or Laue spots defined by the corresponding Bragg angles. (b) A part of the incident beam is diffracted in forward direction and forms the normal absorbed direct beam. The diffracted beam is produced by non-deformed parts of the crystal (shown above and below the defect) and a deformed part (around the defect). Local bending of the crystal planes around the defect change the diffraction conditions and produce a contrast in a Laue spot (see text).

beam, beams with various wavelengths are diffracted with different exit angles. The diffracted beams can overlap or diverge and this results in contrast variations. In order to detect this type of contrast, one must locate the detector far from the sample in far field or Fraunhofer condition. In a white beam topography setup using synchrotron radiation, the detector is usually located close to the sample, so that this type of contrast usually is not detected.

Extinction contrast, the second type of contrast where the misorientation caused by defects is smaller than the divergence of the incident beam, is explained by means of the kinematical and dynamical theories of x-ray diffraction. The x-rays which travel through the crystal and are diffracted

only from perfect planes, without diffraction from the deformed area, cause uniform intensity, called matrix pattern. Extinction contrast can form three kinds of images on the matrix pattern, see Fig.1.6a. The first type is called direct image: x-rays which do not satisfy the Bragg condition for the perfect part of the crystal and reach the defect may be diffracted by the deformed planes around that defect. These x-rays do not suffer from primary extinction before their diffraction, so they result in an intense dark image. The second type is a dynamical image. The part of x-rays which is diffracted in perfect regions is intercepted by deformed area and creates new wavefields which are diffracted in different directions. The dynamical image arises from intensity loss in this area. The third form of image is an intermediate image which can be formed by interference of the propagating new wavefields at the exit surface with the undeviated wavefields propagating in the perfect region. This image often appears with oscillating contrast [47]. The most common type of image in synchrotron white beam topography is the direct image, *i.e.* dark intensity on the matrix pattern [46].

The formation of extinction contrast in a deformed crystal can be explained quantitatively by a parameter called the effective misorientation, $\delta\theta$. In a defective crystal, lattice distortions cause angular deviation from the Bragg condition of a perfect crystal. This deviation can be described by the following expression [11, 48]:

$$\delta\theta = -tan\theta_B \frac{\delta d}{d} \pm \delta\varphi, \tag{1.2.1}$$

where $\delta d/d$ is the local relative change of the lattice parameter and $\delta\varphi(r)$ is the local inclination angle of the reflecting lattice planes with respect to the perfect lattice. The + or - sign is chosen depending on whether the Bragg angle is increased or decreased by the deformation. In terms of the reciprocal lattice vector, $\delta\theta$ is written as:

$$\delta\theta = -\frac{\lambda}{sin2\theta} \frac{\partial(\mathbf{h} \cdot \mathbf{u})}{\partial \mathbf{S}_h}, \tag{1.2.2}$$

where $\mathbf{h}$ is the diffraction vector, $\mathbf{u}$ is the displacement vector, and $\mathbf{S}_h$ is a coordinate in the direction of the diffracted beam. A visual representation of the diffraction vector and the displacement vector is shown in Fig. 1.6b. The contrast of a dislocation is invisible if the displacement vector is perpendicular to the diffracted vector.

The effective misorientation is helpful for the interpretation of the contrasts. Although white beam topography is a powerful and simple technique with sensitivity to high lattice distortion, it is sensitive only to the local inclinations angle and not sensitive to the lattice parameter variation.

1.2.2 Monochromatic beam topography

Crystal Topography and Rocking Curve Imaging

In a double (multiple) crystal topograph (*i.e.* in monochromatic beam topography), radiation with a single wavelength can be diffracted by only one set of planes and forms one Laue spot. This technique is sensitive to both lattice parameter change and lattice inclination. A comprehensive review of this technique is presented in Ref. [49]. Herein, a brief introduction of this technique and its extension used within the scope of this thesis is given.
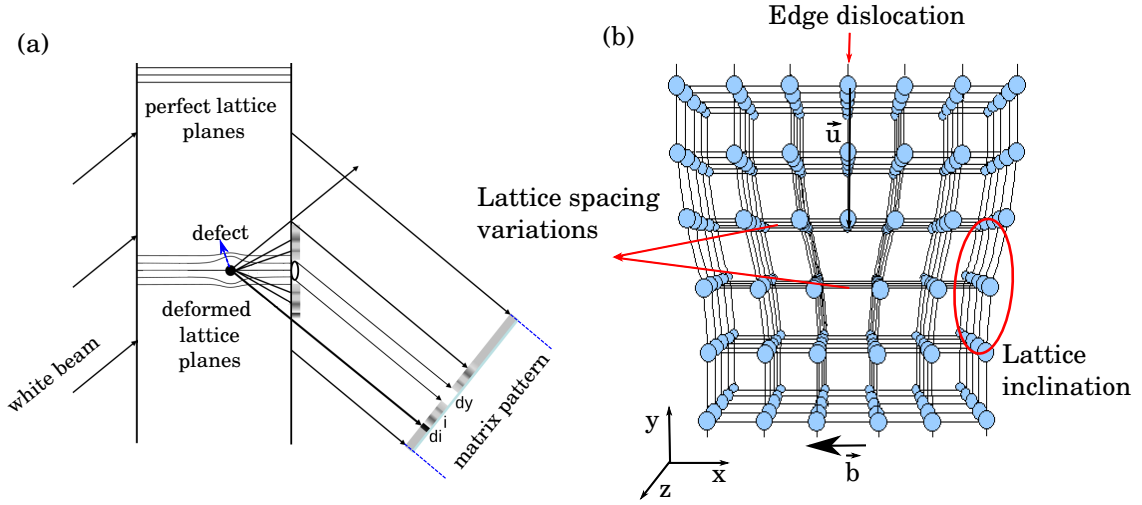
Figure 1.6: (a) Extinction contrast: formation of the three types of image around a defect: (di) direct, (i) intermediate, and (dy) dynamical images. From Ref. [49]. (b) Effective misorientation caused by an edge dislocation. Dislocation is not visible if the diffraction vector (**h**) is along z direction (**u** $\perp$ **h**), refers to Eq.1.2.2. **b** denotes the direction of the Burgers vector

Non-dispersive and dispersive setups for double (multiple) crystal topography exist. We worked in a dispersive setup, because the monochromator crystal, silicon, is different from the sample crystal, sapphire, bearing in mind the necessity for a high degree of perfection for the monochromator crystal. In general, the strain sensitivity from a dispersive setup is smaller than non-dispersive one. Fig. 1.7 presents the schematic of a dispersive setup. X-rays are diffracted by a pair of silicon crystals that select the beam with an energy of 20.0 keV. The part of the beam that fulfils the Bragg condition for sapphire planes forms a narrow topograph on a film or CCD detector. In order to get an image from all areas in the sample (sapphire), the sample needs to be rotated through its angular diffracting range, *i.e.* the rocking curve. Several topographs are recorded during the rotation and are stitched together to get a complete image of the crystal.

Each topograph (before stitching) can also be analyzed separately because the strain sensitivity in different parts of the rocking curve is not the same and the steepest part of the flank has the highest sensitivity. In Fig.1.8 an illustrative series of double crystal topographs is shown. The images have been recorded from the (0, 2, 2) reflection of silicon. Those recorded in the flanks of the rocking curve; positions *b* and *d*, reveal more information than those obtained from other parts [50]. The improved strain sensitivity in the monochromatic beam topography sometimes reveals defects that can not be detected in a white beam topograph.

As discussed, topography using monochromatic beam diffraction gives qualitative information about the perfection of a crystal where an image with high spatial resolution can be obtained using high resolution film. On the other hand, one would be interested in obtaining also a quantitative information about the lattice orientation and misorientation, for instance, by measuring rocking curve at various angular positions. In a rocking curve measurement with laboratory x-ray source, the spatial resolution is limited by the size of the slits. Moreover, the measurement is usually per-

formed slowly in order to get sufficient counts. The third generation synchrotron radiation sources enables us to take advantage of both techniques and produce a quantitative map of a crystal with high spatial and angular resolutions in a reasonable time. This technique is called Rocking Curve Imaging, RCI [51, 52]. The schematic outline of RCI setup is depicted in Fig.1.7.

A topographic map requires a large numbers of high spatial resolution images recorded with small step variation in angular position of Bragg diffraction angle. For this purpose, the sample needs to be rocked through its Bragg angle with a very precise goniometer and data must be collected by a fast detector such as a CCD detector. Because the synchrotron radiation has very small divergence, each pixel of the detector provides information of the local rocking curve, corresponding to an illuminated area in a sample. The spatial resolution is given by the CCD detector and is typically in the few tens μm range. Using a dedicated software, *e.g.* Visrock, described in Ref. [53], maps of integrated intensity, peak position and full width at half maximum (FWHM) can be generated, the latter being often used for determining crystalline quality and local distortion. RCI is used with various materials for different applications, for instance, with silicon for photovoltaics [54], with GaSb/GaAs for modern electronics devices [55] and with diamond for application as optical elements in light sources such as synchrotron and X-ray Free Electron Lasers (XFEL) [49].
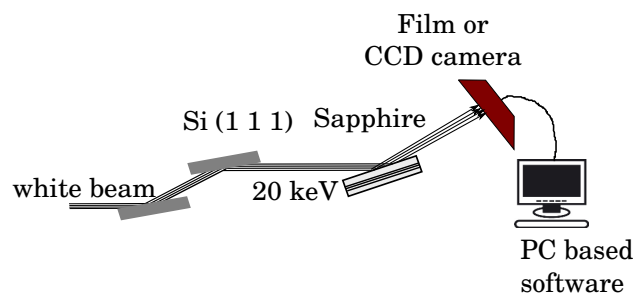
Figure 1.7: Schematic representation of a monochromatic beam topography (here is also called double crystal topography) and rocking curve imaging (RCI) setups. A pair of Si (1, 1, 1) reflection is used to adjust the energy of teh beam to 20.0 keV. The beam is diffracted in Bragg geometry and the diffracted intensity is recorded by a film or by a CCD camera. In RCI, the crystal is being rocked by a precise goniometer in small steps and a large number of topographs are recorded with a CCD camera. RCI maps will be obtained by using a software, *e.g.* Visrock [53]. The maximum beam size (H × V) is 40×8 mm^2 at BM05, ESRF

Backscattering Topography

The principle of the newly developed backscattering topography is similar to the RCI technique. The advantage of using reflections with a Bragg angle close to $\pi/2$ is the narrow spectral width of the backscattered beam and the large Darwin width. The kinematic Bragg diffraction, $\lambda = 2d\sin\theta$, with no consideration of dynamic effects does not in general give the correct angular position and reflection coefficient of Bragg reflections. The generalized form of the Bragg equation (valid for
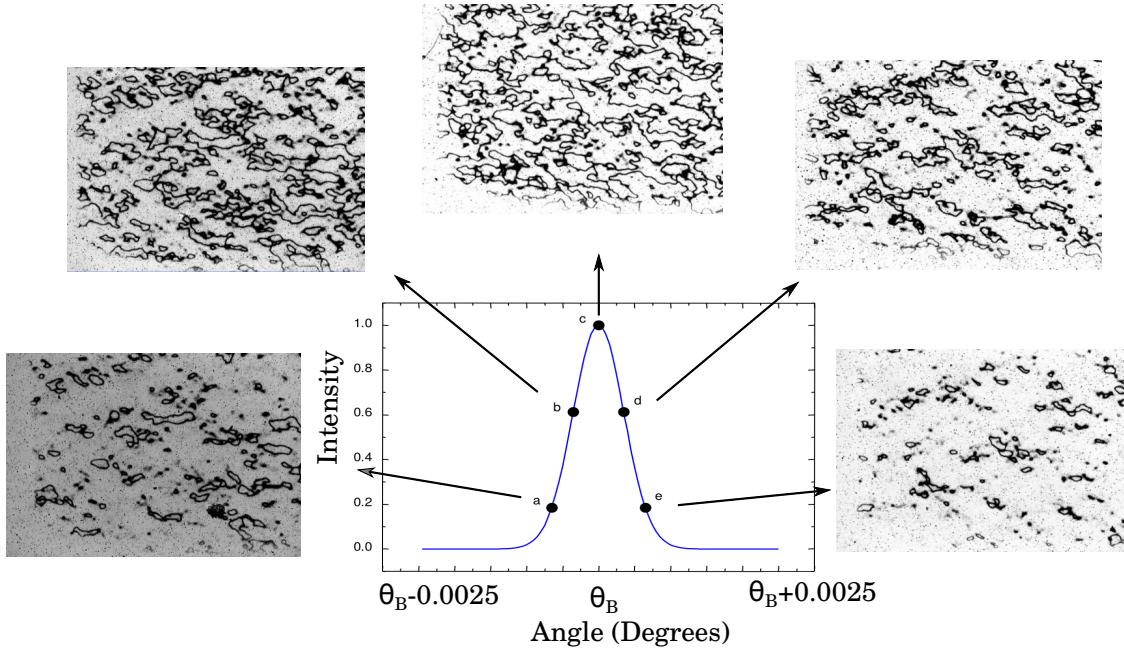
Figure 1.8: Double crystal topographs with the (0, 2, 2) reflection of a Si layer of Si-SiO$_2$ on a Si substrate recorded at different positions of the rocking curve. Most defects emerge in the topographs recorded at the positions *b* and *d*. From Ref. [50].

the whole range of incident angles), considering Bragg's law correction, ω_H, has been discussed by Y. Shvyd'ko [56]. The Bragg equation under dynamical conditions can be written as:

$$2dsin\theta_\pm = \lambda(1 + \omega_H \pm \frac{\epsilon_H}{2}), \tag{1.2.3}$$

$$\omega_H = -\chi_0 \frac{d^2}{\lambda^2} \frac{b-1}{b}, \tag{1.2.4}$$

$$\epsilon_H = \frac{|C\chi_H|}{sin^2\theta \sqrt{|b|}}, \theta \neq 0. \tag{1.2.5}$$

where ϵ_H is the relative spectral width for a given Bragg reflection, b is the asymmetry factor, C is the polarization factor, χ_0 and χ_H are the Fourier components of the electric susceptibility of crystal. The $\pm$ sign is related to the range of $\theta_- - \theta_+$ which, gives the width of reflectivity curve under dynamical conditions. The asymmetry factor is defined by Eq.1.2.6, the parameters are shown in Fig. 1.9 [13].

$$b \equiv \frac{sin\theta_i}{sin\theta_e} = \frac{sin(\theta_B + \alpha)}{sin\theta_B - \alpha)}, \tag{1.2.6}$$

where the diffracting lattice planes form an angle (α) with the crystal surface. The incident and exit angles are θ_i and θ_e, respectively. The widths of the incident and exit beams are directly related

to each other by the asymmetry factor through equation: $H_i = b \cdot H_e$. The Darwin width of the incident beam ($\delta\theta_i$) is given by: $\delta\theta_i = (1/\sqrt{b})(\omega_D tan\theta)$, and conversely the angular spread of the exit beam is increased to $\delta\theta_e = (\sqrt{b})(\omega_D tan\theta)$.
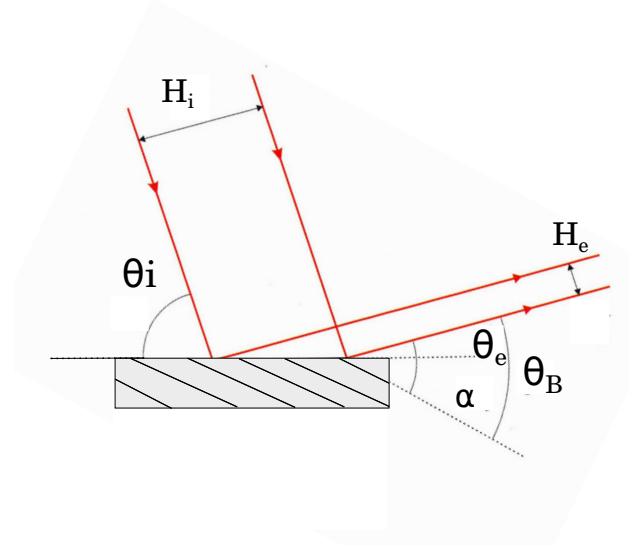
Figure 1.9: Parameters for an asymmetric reflection with Bragg angle θ_B. α is the angle between the scattering crystal planes and the surface, θ_i and θ_e are the angle between crystal surface and the incoming and exit beam, repsectively (Figure is reproduced from Ref. [13]).

The great advantage of using backscattering geometry is illustrated in visual representation of Bragg's law in Fig. 1.10. Bragg's law under kinematical and dynamical conditions in the symmetric Bragg scattering case are plotted in dashed and solid lines, respectively. When the glancing angle to the reflecting atomic planes (θ) is very close to $\pi/2$ a broad angular range with a narrow spectral width can be obtained [17]. Also, the graph indicates that in this geometry, since λ vs. θ is almost flat, the energy variation depends only on the changes of lattice plane distance, d-spacing. However, far from $\pi/2$ where the slope of the curve is higher, the energy variation depends on both the angle and interplanar distance. Therefore, in order to determine only the lattice parameter variation in Eq.1.1.2, reflections with a Bragg angle very close to $\pi/2$ must be chosen.

This technique has been used in the quality assessment of quartz [57], diamond [58], and sapphire [20]. Fig. 1.11 shows the intensity mapping of back-reflected x-rays from reflection $(0, 1, \bar{1}, 50)$ of sapphire together with the rocking curves for selected regions with good and poor quality [20].

1.2.3 Mössbauer Spectroscopy

A free nucleus can be excited from the ground state to the excited state by a γ-ray with energy of $E_0 + E_R$. E_0 is the energy difference between the excited and the lower states and E_R is the recoil energy. These are linked to each other according to:

$$E_R \approx \frac{E_0^2}{2Mc^2},$$

(1.2.7)
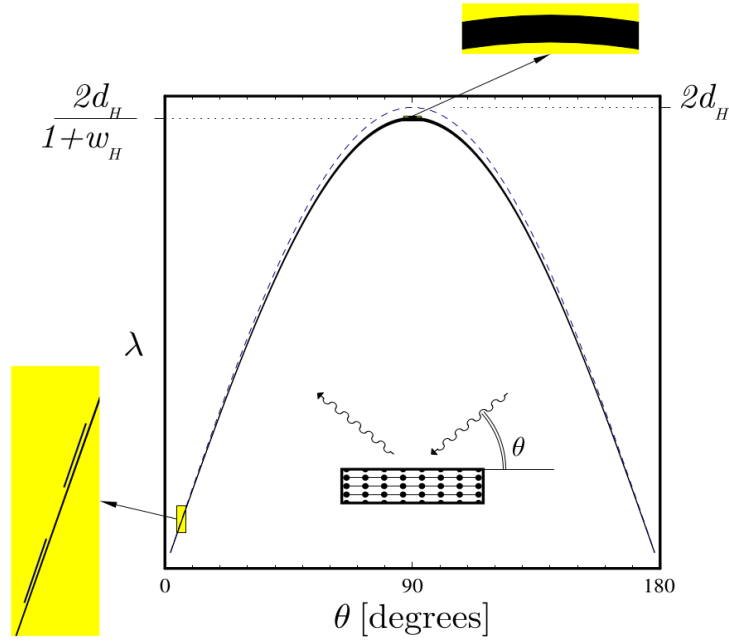
Figure 1.10: Graphical representation of Bragg's equation assuming diffraction from a perfect crystal with planes parallel to the surface, *i.e.* assuming asymmetric reflection. The dashed and solid lines show Bragg's law under the kinematical and dynamical conditions. Figure reproduced from Ref. [17].

where M is the mass of nucleus, and c is the speed of light. A nucleus emitting a photon undergoes recoil with energy of E_R that assures conservation of momentum and energy. In a classical approximation, if the nucleus is bound in a solid, there is finite probability that the recoil energy is taken up by the entire solid. In this case, the recoil is negligible. Therefore, the required energy for excitation of nuclei bound in a solid becomes E_0. A γ-ray with the energy of E_0 emitted from a nuclei bound in solid (*i.e.* from a radioactive source) can excite another nucleus with transition energy E_0 bound in another solid (*i.e.* in an absorber). This elastic process of emission and absorption of γ-ray by nuclei without recoil was discovered in 1958 [59] and is called Mössbauer effect. The probability of the Mössbauer effect is given by the Lamb-Mössbauer factor, f_{LM}. The solid absorbs the energy and excite phonons through an inelastic process with probability of $1 - f_{LM}$. f_{LM} is linked to the atomic mean square displacement parameters, $\langle u^2 \rangle$, by:

$$f_{LM} = exp(-k_\gamma^2 \langle u^2 \rangle), \tag{1.2.8}$$

where k_γ is the γ-ray wave vector. Using the Debye model which assumes a parabolic DPS up to a cut-off energy, f_{LM} can be written as:

$$f_{LM} = exp\Big(- \frac{6E_R}{k_B \Theta_D} \big(\frac{1}{4} + \big(\frac{T}{\Theta_D} \big)^2 \int_0^{\frac{\Theta_D}{T}} \frac{x}{e^x - 1} dx \big) \Big), \tag{1.2.9}$$

where k_B is the Boltzmann's constant, T is the temperature and Θ_D is the Debye temperature, quantifying the cut-off energy, $E_D = k_B \Theta_D$. Eq.1.2.9 expresses that the the higher temperature, the
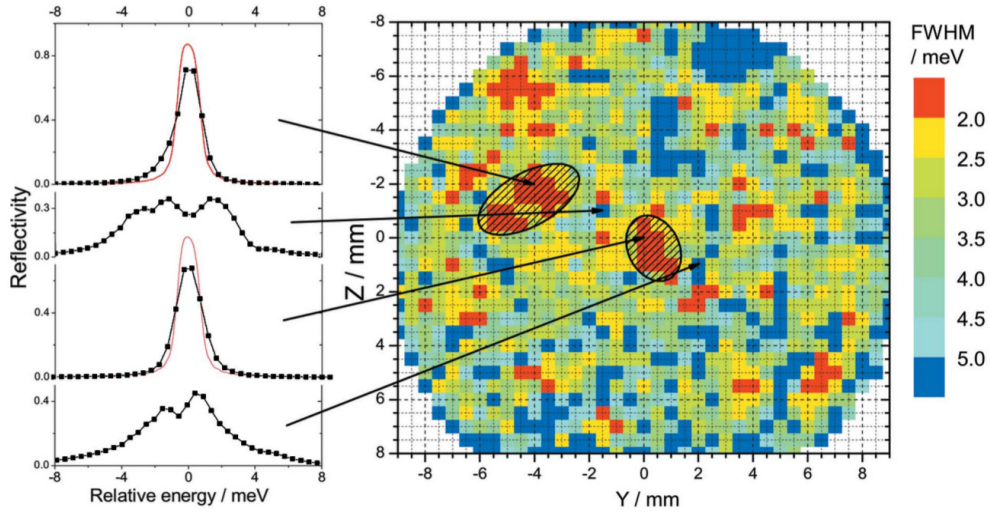
Figure 1.11: A rocking curve FWHM map of 1 mm thick sapphire single crystal. Reflectivity is recorded by a silicon avalanche photo-diode, APD. The x-ray beam was tuned around 23.88 keV using [119]Sn high resolution monochromator. The dashed ellipses area indicates the high quality region of crystal which resulted in narrow reflectivity curves, shown in the left side of the map. The rocking curves selected from outside of this region are broad, from Ref. [20].

lower is f_{LM}. At temperatures much lower than the Debye temperature, Eq. 1.2.9 can be written as:

$$f_{LM} \cong exp\{-\frac{E_R}{k_B\Theta_D}(\frac{3}{2} + (\frac{\pi T}{\Theta_D})^2)\}, \tag{1.2.10}$$

and at higher temperature, *i.e.* at $T \geq \frac{\Theta_D}{2}$ Eq. 1.2.9 is simplified to:

$$f_{LM} \cong exp\{-\frac{6E_R T}{k_B\Theta_D^2}\}. \tag{1.2.11}$$

Equations 1.2.8 and 1.2.10 demonstrate that even at $T = 0$, f_{LM} does not reach unity. To put it in another way, the atomic displacement parameter does not reach zero at absolute zero temperature. In order to observe the nuclear resonance absorption and measure the complete Mössbauer spectrum, in an experimental setup, the source or the absorber are moving towards or away from each other to change the relative energy of the γ-ray emitted from the source by the Doppler effect. Often, the absorber is fixed and the source vibrates with a velocity in range of a few ten mm/sec. The Mössbauer spectrum yields the hyperfine interactions in the absorber, that is the interaction of the nucleus with its electronic environment that determines the surrounding electric or magnetic fields.

A Mössbauer spectrum shows the intensity of transmitted γ-rays as a function of velocity and is characterized mainly by three parameters: the isomer shift (δ), which is induced by a difference in electron density between the source and the absorber, the quadrupole splitting (ΔE_Q) which is due

to interaction between and the nuclei and electric field gradient (EFG), and the magnetic hyperfine splitting which arises due to interaction between the nucleus and surrounding magnetic fields.

Basically, the Hamiltonian (H) used for nuclear hyperfine interaction, H can an be expressed as:

$$H = H_e + H_m = (H_I + H_Q) + H_m, \tag{1.2.12}$$

where H_e represents the electrostatic interaction, caused by the nearby electrons and H_m is the magnetic interaction due to the magnetic moment. In Eq.1.2.12, I and Q denote the isomer shift and quadrupole, respectively. In the following, only H_e which includes the isomer shift and quadrupole splitting will be briefly introduced since the materials used in this study are not magnetic.

Isomer shift   The isomer shift is a result of electrostatic monopole Coulomb interaction between mainly s-orbital electrons and the nuclear charge distribution. The transition energy in the source is different from the transition energy in the absorber because of different electronic and crystallographic environments, see Fig. 1.12a. This difference can be measured in a Mössbauer spectrum as the distance between the minimum of the absorption line and the zero point in the velocity axis, see Fig. 1.12b, calibrated to a reference sample. The isomer shift is a useful quantity for determining the bonding properties and the oxidation states of the specific atoms. The isomer shift is a relative value, it is described in velocity units and it is given most often relative to a standard absorber.

The Hamiltonian for the isomer shift, H_I is related to the electrostatic term of the hyperfine interaction, H_e, and is expressed as [60]:

$$H_I = \frac{1}{6} \sum_{ij} V_{ij} \int r^2 \rho(\mathbf{r}) d^3\mathbf{r}, \tag{1.2.13}$$

where V_{ij} is the Cartesian components of electric potential energy and $\rho(\mathbf{r})$ is the charge density at the point $\mathbf{r} = (x_i, x_j, x_k)$, where x_i, x_j, x_k denote the Cartesian coordinates. Under an assumption of spherical shape of charge distribution, this interaction can be written as:

$$H_I = \frac{2\pi}{3} e^2 Z |\psi(0)|^2 < R^2 > . \tag{1.2.14}$$

Here Z is the charge number of the nucleus, R is the nuclear radius and $|\psi(0)|^2$ is the density of probability of presence of s-electrons in the nucleus at $\mathbf{r} = 0$. Finally, the isomer shift can be obtained as:

$$\delta = \frac{2}{5} Z e^2 (R_e^2 - R_g^2)\{|\psi(0)|_a^2 - |\psi(0)|_s^2\}, \tag{1.2.15}$$

where R_e and R_g are the nuclear radius in the excited and ground states, respectively.

Electric Quadrupole Splitting   A non-spherical nucleus has a spin quantum number, I, greater than $1/2$ and it is characterized by a nonzero nuclear quadrupole moment, Q. The interaction of the nuclear quadrupole moment and the inhomogeneous EFG leads to quadrupole splittings. This interaction splits the nuclear state with $I > 1/2$ into sub-states, see last part of the diagram in
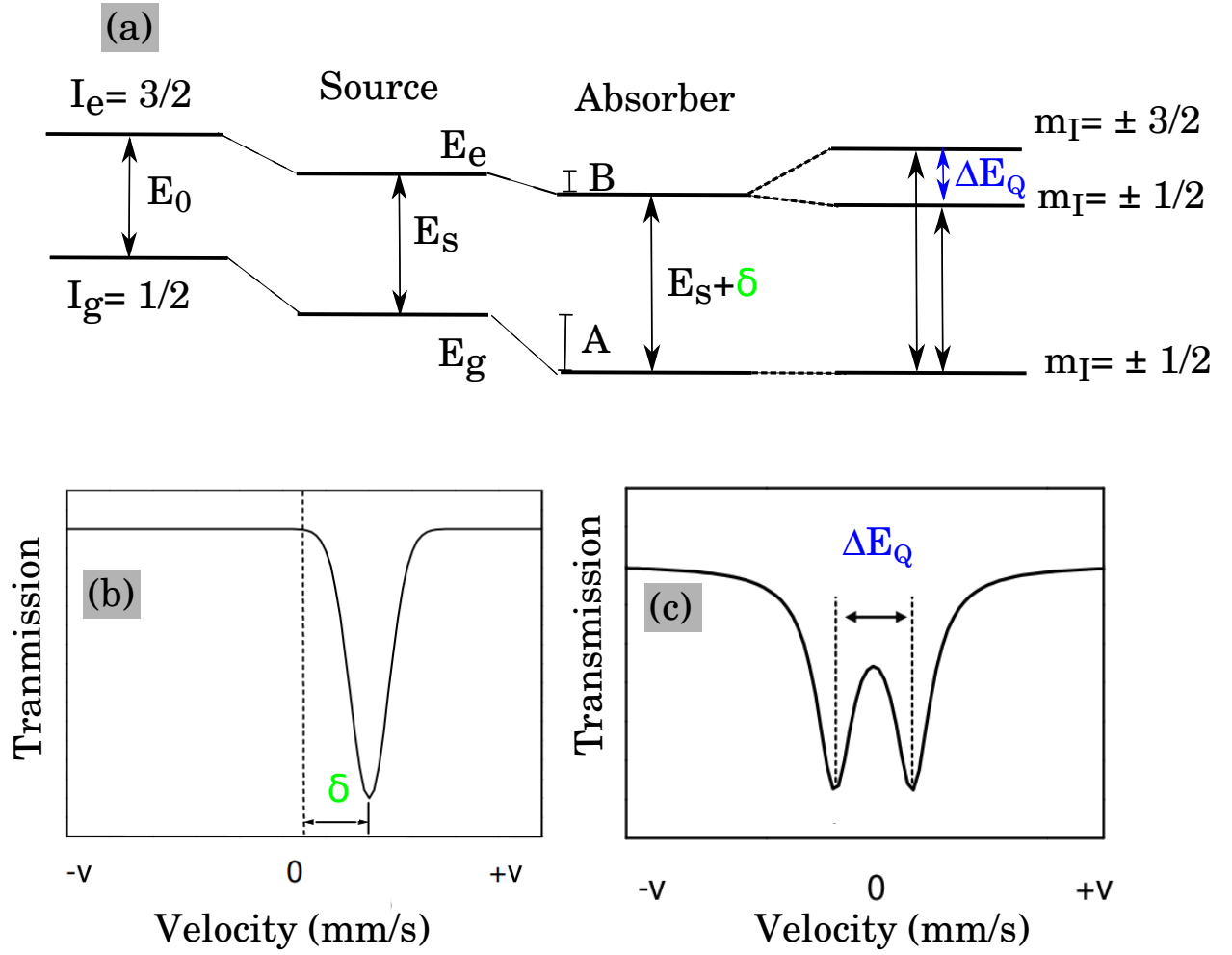
Figure 1.12: (a) A schematic representation of the nuclear energy levels of the source and the absorber for ^{57}Fe. E_0 is the transition energy of a bare nucleus between its ground state (with spin of $I_g=1/2$) and excited state (with spin of $I_e=3/2$). The transition energies in the source (E_s) and absorber $E_s+(A-B) = E_s+\delta$ are different by the amount given by the isomer shift, δ. In presence of an EFG, the nuclear level with $I_e=3/2$ splits into 2 sub-states with magnetic quantum numbers of $m_I= \pm 1/2$ and $m_I= \pm 3/2$. (b) The isomer shift can be measured from a shift of the minimum in a Mössbauer spectrum relative to the zero velocity or a reference sample. (c) The non-spherical charge distributions and gradient of the electric field results in a quadrupole doublet, the distance between the two minima gives the magnitude of the quadrupole splitting, ΔE_Q,

Fig.1.12a. The energy difference between these sub-states indicates the quadrupole splitting, ΔE_Q. This appears as doublet or multiplets in a Mössbauer spectrum, Fig. 1.12a. Note that the sub-states with the same absolute value of $|m_I|$ remains degenerate at the same energy level.

The term H_Q in Eq.1.2.12 is the electrostatic interaction energy which depends on the shape of the

nucleus and is expressed as:

$$H_Q = \frac{1}{6} \sum_{ij} V_{ij} \int (3x_i x_j - \delta_{ij} r^2) \rho(\mathbf{r}) d^3 \mathbf{r} = \frac{1}{6} (\nabla \mathbf{E}) e \mathbf{Q}, \tag{1.2.16}$$

where V_{ij} are the elements of the electric field gradient tensor. The quadrupole interaction energy is governed by:

$$E_Q(I, m) = \frac{e^2 Q V_{zz}}{4I(2I-1)} \left(3m_I^2 - I(I+1)\right) \sqrt{1 + \frac{\eta^2}{3}}, \tag{1.2.17}$$

where η is the asymmetry parameter. In the EFG tensor ($\nabla \mathbf{E}$), usually the off diagonal elements are chosen to be zero by choosing of the coordinate system. Thus, the electric field has three components, V_{xx}, V_{yy}, and V_{zz} with the convetion: $| V_{zz} | \geq | V_{yy} | \geq | V_{xx} |$. These elements are related to each other by η, defined as following:

$$\eta = \frac{V_{xx} - V_{yy}}{V_{zz}}. \tag{1.2.18}$$

If the site symmetry of the nucleus has a threefold or higher symmetry axis then the EFG is symmetric around this axis and $\eta = 0$ [61]. The quadrupole splitting is then given by $\Delta E_Q = eQV_{zz}/2$. The schematic of quadrupole interaction in a simple case of a nucleus with ground state with spin $I = 1/2$ and excited state with spin $I = 3/2$, *e.g.* ^{57}Fe is presented in Fig. 1.12c. However, in the case of ^{121}Sb ($I_g = 5/2, I_e = 7/2$) with rather large natural linewidth (Γ_0), the Mössbauer spectrum is significantly more complicated. ^{121}Sb Mössbauer results will be discussed in chapter 4 and 5.

1.2.4 Nuclear Inelastic Scattering

Nuclear inelastic scattering (NIS) is one of the NRS techniques which gives access to density of phonon states (DPS) and further enables investigations of lattice dynamics of materials containing at least one Mössbauer active isotope. The DPS is required for evaluating lattice dynamics. The phonon is the quantum of vibrational energy. It has energy $\hbar\omega$ and wave vector $\mathbf{q}$. The frequency dependence $\omega(q)$ is known as the phonon dispersion relation. From an integral of phonons over $\mathbf{q}$, DPS can be obtained. A peak in a DPS spectrum represents one or more vibrational modes, and often the peaks have a width in the range of meV. In a NIS experiment, a monochromator with resolution better than meV is desirable in order to resolve the vibrational modes in a DPS spectrum. Thus, in order to obtain NIS data of high quality, one needs to use high resolution monochromator with a good energy resolution.

Incoming photons with energy in the vicinity of the Mössbauer transition excite the nucleus. Subsequently, the nucleus de-excitation occurs either by emitting γ-ray fluorescence (also known as nuclear fluorescence) in a process of either radiative nuclear decay or by ejection of an electron from the *s*-orbitals through internal conversion followed by x-ray fluorescence. The x-ray fluorescence and γ-ray fluorescence occur with the lifetime of the nuclear resonance, *e.g.* 4.99 ns for ^{121}Sb. In a NIS experiment, the intensity of x-ray fluorescence and γ-ray fluorescence are recorded as a function of the energy of incoming photons, tuned in a range of a few ten meV around the Mössbauer transition energy. These delayed photons are distinguishable from the prompt photons fluorescence (non-resonant photons) by using the timing method. The synchrotron radiation has a

time structure imposed by the bunches of electrons in the storage rings. In the timing method, the electronics are allowed to acquire signals only in between the times corresponding to synchrotron radiation pulses, thereby segregating signal and noise. When the energy of the incident photons match the Mössbauer transition energy exactly, a sharp peak of elastic nuclear absorption occurs. When the energy of the incident beam is higher or lower than the Mössbauer transition energy, phonons are created or annihilated and compensate the difference in the photon and nuclear transition energies. If one assumes that the area of an energy spectrum of resonant inelastic absorption of γ-ray by nuclei is equal to unity, then the partial area of elastic and inelastic transitions are given by $\sim f_{LM}$ and $1 - f_{LM}$, respectively. The phonons involved in this transition correspond to inelastic side-bands to the elastic line in the energy spectrum [63]. The normalized probability for nuclear inelastic absorption, W(E), is given by:

$$W(E) = f_{LM}\left[\delta(E) + \sum_{n=1}^{\infty} S_n(E)\right], \tag{1.2.19}$$

where the Dirac function $\delta(E)$ describes the elastic absorption, with zero-phonon process, and $S_n(E)$ describe the inelastic absorption accompanied by creation or annihilation of n phonons. The single phonon term $S_1(E)$ can be calculated from:

$$S_1(E) = \frac{E_R g(|E|)}{E(1 - e^{-\beta E})} , \tag{1.2.20}$$

where $g(E)$ is the density of phonon states, $\beta = (k_B T)^{-1}$, and T is sample temperature. The multiphonon contribution S_n, assuming a harmonic approximation, is given by:

$$S_n(E) = \frac{1}{n} \int_{-\infty}^{\infty} S_1(E') S_{n-1}(E - E') dE'. \tag{1.2.21}$$

The function $g(E)$ can be calculated by the following expression:

$$g(E) = V_0 \frac{1}{(2\pi)^3} \sum_j \int \delta[E - \hbar\omega_j(\mathbf{q})] d\mathbf{q}, \tag{1.2.22}$$

where V_0 is the volume of the unit cell, the index j gives the branches of the dispersion relation $\hbar\omega_j(\mathbf{q})$, $\mathbf{q}$ is the phonon momentum and the integral is taken over the first Brillouin zone. Further information about the inelastic nuclear absorption is provided in [64]. The probabilities of creation and annihilation of phonons are related to each other by the following expression: $S(E) = exp(E/k_B T)S(-E)$, where $S(E)$ and $S(-E)$ are the probabilities of creation and annihilation of phonons, respectively.

The scheme of a typical NIS setup is shown in Fig. 1.13a. The undulators produce x-ray radiation, the heat load from the undulators is handled by HHLM which consists of two independent silicon (1, 1, 1) crystals. The beam is premonochromatzied to a few eV by the HHLM. Then, the beam is further monochromatized by a high resolution monochromator (in our case it is the backscattering monochromator, BSM) to meV range and the reflected beam impinges on the sample. Scattered radiation is counted by two APD detectors, the NIS spectrum (*i.e.* the intensity of incoherent nuclear scattering) and the NFS time spectrum obtained from the detector placed very close to the
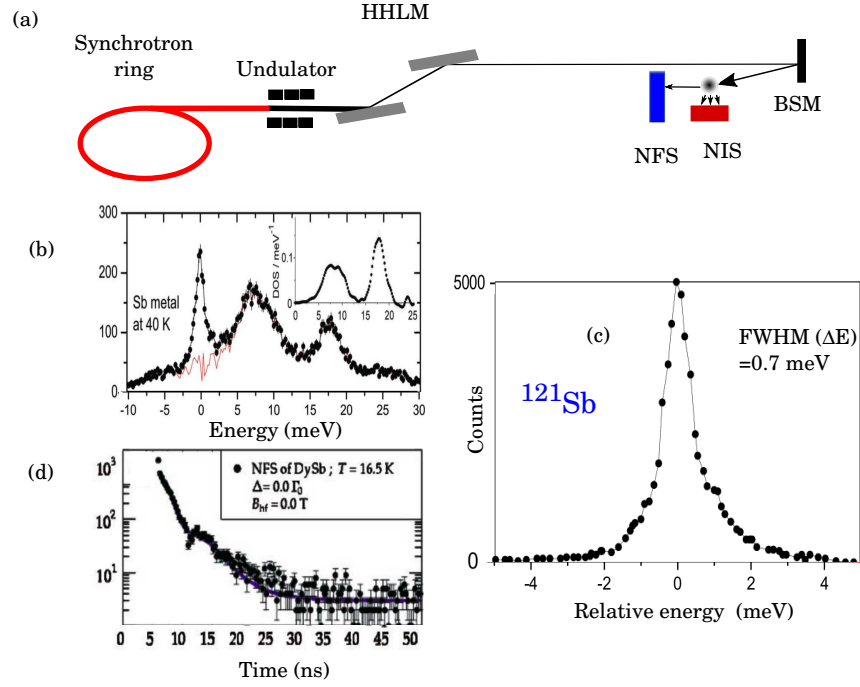
Figure 1.13: (a) Schematic experimental setup for NIS and NFS measurements. The electron beam emits a high brilliance x-ray beam when passing the undulator. The x-ray beam in the ring from the undulators, *i.e.* arrays of magnets, is premonochromatized to a few eV by the High Heat Load Monochromator, HHLM, and then reflected by the Backscattering Monochromator (BSM) and reaches (sub-)meV resolution. We obtain different energies by choosing different reflections of the sapphire [20]. The back-reflected beam impinges on the sample, incoherent scattering of radiation is monitored by the NIS detector, located close to the sample to cover a large solid angle. The coherent photons scattered elastically in forward direction are counted by the NFS detector, located far away from the sample. The dependence of inelastic absorption on the energy of the incident radiation is recorded by tuning the energy of the incident beam, here by changing the temperature of the sapphire crystal. The elastic line of a NIS spectrum is the scaled instrumental function of the monochromator that can be measured by the NFS detector. (b) An example of NIS spectrum measured for ^{121}Sb. The inelastic spectrum with subtracted elastic lines is shown by red solid line, the extracted density of phonon states is presented in inset, from Ref. [20]. (c) Instrumental function of the BSM for Sb measured with forward scattering of synchrotron radiation in September 2014 at ID18, ESRF. The FWHM (energy resolution) shows a width of 0.7 meV. (d) An example of a NFS spectrum measured for ^{121}Sb in DySb, figure from Ref. [62].

sample and rather far from the sample in forward direction, respectively [65]. The instrumental function of the spectrometer is monitored with the forward scattering detector during the experiment. In order to extract the DPS, the scaled elastic line must be subtracted from the absorption spectrum. An example of NIS spectra of ^{121}Sb before and after subtraction of the elastic line is shown in Fig.1.13b, the inset shows the extracted DPS, result is published in 2011 [20]. It is worth pointing out the instrumental function with a FWHM resolution of 0.7 meV for ^{121}Sb has been recently developed at ID18, ESRF, see inset c in Fig.1.13. The main advantage of NIS over other similar techniques dealing with phonons, like Raman scattering, infrared absorption, and INS, is the isotope selectivity. In other words, NIS probes vibration of a particular nuclear isotope without sensitivity to vibrations of the other atoms in the material. The performance of an NIS experiment is determined by the optical monochromator because the monochromator defines the energy resolution of the measured spectrum. As it was mentioned in section 1.1 of this chapter, an extremely high energy resolution monochromator (in range of sub-meV) is a great help in resolving different groups of phonons in a DPS.

1.2.5 Nuclear Forward Scattering

Another NRS technique is Nuclear Forward Scattering (NFS), an important method for hyperfine spectroscopy. It is a complementary technique to the classical Mössbauer spectroscopy. NFS allows for studying the electronic and magnetic properties of Mössbauer isotopes related to the hyperfine interaction. Therefore, it provides information about the environment of the Mössbauer nuclei [1–3].

The meV energy bandwidth of the incident beam determined by the monochromator used for NFS is several orders of magnitude larger than the bandwidth of photons emitted from a radioactive source used in Mössbauer spectroscopy, which is in the range of nano-eV. As a result, the synchrotron radiation excites *all* the possible transitions between the sub-levels of the ground and excited states. During the decay process, a photon can be emitted in any of the hyperfine transitions with a certain probability. As a result, the partial waves travel with different frequencies and phases. The NFS time spectrum shows the intensity resulting from the interference of the partial waves in forward direction as a function of the delay time.

In an experimental setup presented in Fig. 1.13a, the detector in forward direction measures the time structure of the prompt and delayed photons. The NFS technique is a very useful method to study hyperfine interactions for samples, especially when there is no available Mössbauer source [66]. An example of NFS spectrum recorded for ^{121}Sb is presented in Fig. 1.13d, taken from Ref. [62].

For a nucleus with a linewidth of $\Gamma = \hbar/\tau$ and $|\Delta E_Q| = \hbar\Delta\omega$, under the condition that $|\Delta E_Q|$ is greater than $t_{eff}\Gamma$, the intensity of NFS can be approximated by [61]:

$$I_{fwd}(t) \sim \Gamma_0 \frac{t_{eff}}{t/\tau_0} exp(-t/\tau_0 - \sigma_{el} \cdot n \cdot d) J_1^2(\sqrt{0.5 t_{eff} t/\tau_0})$$
$$cos^2(0.5\Delta\omega t + \frac{t_{eff}\Gamma_0}{8\hbar\Delta\omega}), \quad\quad (1.2.23)$$

where n is the number of nuclei per unit volume, σ_{el} is the electronic absorption cross section, J_1 is the Bessel function of first order and t_{eff} is the effective thickness of the sample. The effective

thickness; more precisely the effective absorber thickness and f_{LM} are related by [61]:

$$t_{eff} = d \cdot n \cdot f_{LM} \cdot \sigma_0 \cdot \zeta \qquad (1.2.24)$$

where d is the geometrical absorber thickness, ζ is the natural isotopic abundance, and σ_0 is Mössbauer resonance cross section. In the simplest case, the time behaviour for a sample without splitting of the ground and excited states is a simple exponential decay as shown schematically in Fig. 1.14a. The re-emitted photon is delayed relative to the incident photons because of the life time of the nuclear excited states. Due to the sample thickness, coherent multiple scattering from many nuclei show a characteristic time modulation, so called dynamical beats, see Fig. 1.14b. Dynamical beats are described by the square of a Bessel function in Eq.1.2.23.

In the case of hyperfine splitting, the interference of two partial waves, *e.g.* from two hyperfine transitions in case of quadrupole splitting, result in quantum beats in the time spectrum which are described by the cosine term in Eq.1.2.23. These beats appear as an envelope of the exponential decay as shown in Fig. 1.14c. Usually, quantum beats are superimposed over the dynamical beat, see Fig. 1.14d.

The transition of ^{121}Sb with spin ground state, $I_g = 5/2$, to excited state with $I_e = 7/2$, has an energy of 37.13 keV. In the case of an electric quadrupole interaction the ground and excited states split to 3 and 5 sub-levels, respectively. Corresponding to $|m_I| = 5/2, 3/2, 1/2$ and $|m_e| = 7/2, 5/2, 3/2, 1/2$ and according to the selection rule of $\Delta m_I = 0, \pm 1$, there are eight possible hyperfine transitions. In this work, all NFS results have been recorded for the ^{121}Sb transition and the CONUSS software package [67] has been used for fitting the data. An overview of NFS can be found in Ref. [3] and information focused on theoretical aspects are given in Refs. [68–71]. More information about this technique are provided for iron in Refs. [68, 72], and for non-iron isotopes in Refs. [73–75].

Hyperfine Interaction in Antimony and Tellurium bearing compounds

There is a particular interest in materials with $A_n X_m$ system; where A is a p block metal cation such as Te^{+4}, or Sb^{+3} and X is a non-metal anion such as O. Cations or anions with the ns^2np^x structure are called lone pair cations/anions. The nonbonding electrons in the outermost shell are called lone pair electrons. The lone pairs push the bonding electrons together by applying more repulsion than bonding orbitals. Therefore, materials with stereochemically active lone pairs often have a non-symmetrical structure. Antimony oxide Sb_2O_3 and tellurium oxides TeO_2 are two examples of interesting materials comprising lone pair electrons. The chemical environment of Sb and Te atoms can be understood by Mössbauer spectroscopy and NFS. Klobes *et al.* [77] have been reported that stereochemically active lone pairs in Te^{+4} give rise to pronounced quadrupole splitting energies in TeO_2 using NFS.

Antimony oxides can be used as simple metal oxides either in bulk [78] or nano structure [79] and also can be used in non-centrosymmetric or low-dimensional complexes such as $CoSb_4O_6F_6$ [80] and $FeTe_3O_7Cl$ [81]. Although the environment of Sb in some of antimony oxides, *e.g.* Sb(V) in Sb_6O_{13}, is asymmetric, it was found to be not a strong enough effect to be visible in experimental results obtained by Mössbauer spectroscopy [82] or NFS, see Fig.1.15. As it was mentioned earlier in this chapter, if Γ_0 is large, small quadrupole splittings result in a broadening of abosrption line in

(a)

(b)

(c)

(d)
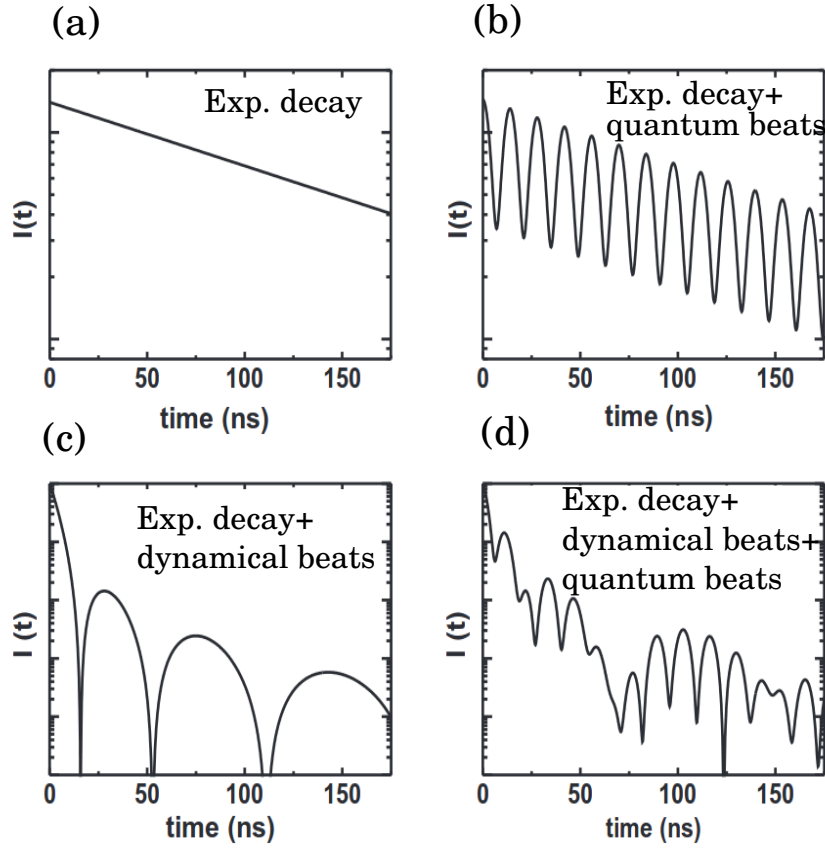
Figure 1.14: (a) Schematic illustration of a single transition without consideration of dynamical beats. (b) The effective thickness shows up as dynamical beats, refers to square of a Bessel function in Eq.1.2.23. (c) Non-zero quadrupole splitting appears as quantum beats, described by the cosine term in Eq.1.2.23.(d) The effect of quantum and dynamical beats on NFS time spectra in a real is a superimposition of dynamical and quantum beats. Adopted from Ref. [76].

a Mössbauer spectrum and not a clear splitting. The Mössbauer spectrum of Sb_2O_5 did not reveal any splitting and its fit showed a small value of $\sim \Delta E_Q = -2$ (mm/s) [83, 84]. We recorded NFS spectra of Sb_2O_5 and $HSbO_3$, the results did no reveal any clear quantum beats and the fits have been done considering $\Delta E_Q = 0$, these fits are shown in solid line in the same figure. In contrast, the EFG around Sb(III) atoms in two stable phases $\alpha-$ and $\beta-Sb_2O_3$ oxides cause a pronounced quadrupole splitting according to several Mössbauer spectroscopy results [84, 85]. We will show the NFS results of α- and β-Sb_2O_3 and their comparison with Mössbauer spectroscopy results will be discussed in chapter 5.
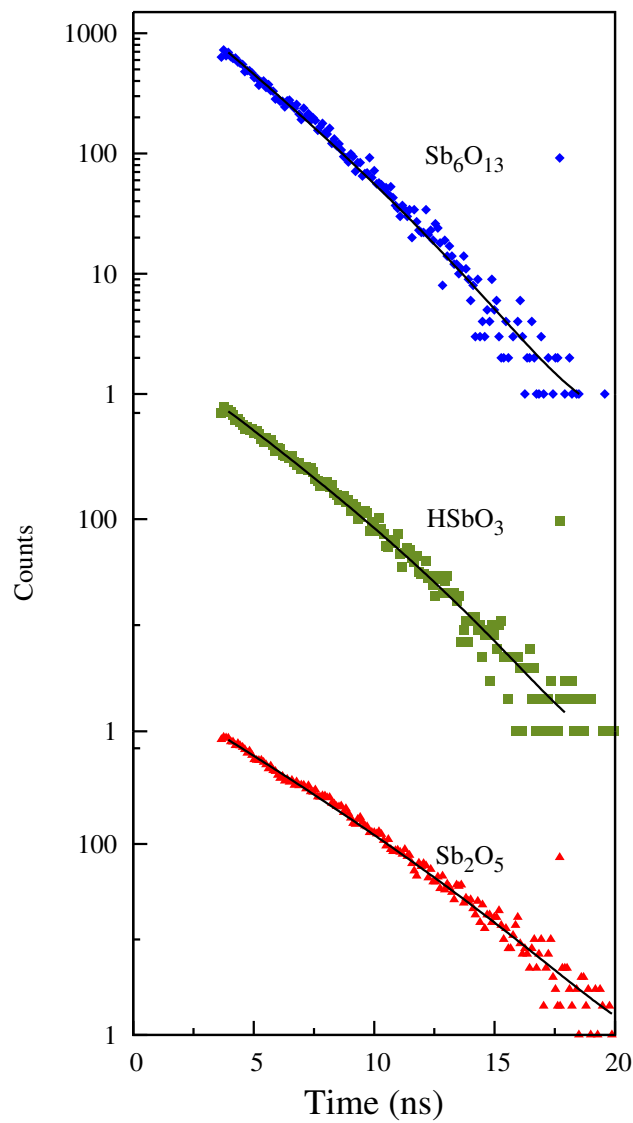
Figure 1.15: NFS spectra of Sb_6O_{13}, Sb_2O_5, and $HSbO_3$ measured at room temperature at the beamline P01, PETRA-III at Deutsches Elektronen-Synchrotron (DESY). Solid lines are fits to the spectra. Samples provided by C. Petrovic, Brookhaven National Laboratory.

Chapter 2

2

White Beam Topography

2.1 Introduction

White sapphire is part of the corundum crystals family, known as aluminium oxide mineral (α-Al_2O_3). The term "sapphire" hereinafter refers to white sapphire as it is commonly used in the optics community. Single crystalline sapphire has rhombohedral arrangement of the atoms with $R\bar{3}C$ symmetry group, often the pseudo hexagonal setting is used for Bragg peak intensity. Its excellent optical properties, chemical resistance, hardness and thermal properties make sapphire a preferred material for various optical application such as semiconductor substrate, Light-Emitting Diodes (LEDs), optics devices, and optical windows for aerospace, [86]. The great demand for high quality devices is linked to the sapphire crystal perfection [87]. In semiconductor technology, the influence of substrate on the perfection of semiconductors is well known [88]. The carrier mobility in silicon-on-sapphire (SOS) transistors is controlled by the high crystallographic perfection in the silicon film adjacent the silicon/sapphire interface [89]. Growing high quality GaN film on a sapphire substrate is still a challenge because of the diffusion of oxygens from the substrate to GaN via defects and lattice mismatch between the substrate and sapphire [90]. Any kind of defects or cracks cause stress in sapphire crystal, stress that results in yield reduction of LED and performance [91]. Hence high quality crystals in terms of crystallographic orientation and purity are required. Crystal imperfections directly impact the quality of x-ray optics. Sapphire has been used as an analyzer in a Resonant Inelastic X-ray Scattering (RIXS) [19, 92, 93] and a monochromator in Nuclear Inelastic Scattering (NIS) [20, 56, 94] experimental setups.

The properties of synthetic sapphire depend on the details of the manufacturing processes. Synthetic sapphire has been made using different growth techniques for several decades. Because of the difficulty of producing high quality sapphire in large volume crystal growth and of the enormous demand for large perfect sapphire crystals, quality evaluation of sapphire has been studied extensively in theory and experiments [31, 34, 91, 95, 96]. The Verneuil method was the first method and has been used in numerous experiments over a century [97]. In this technique, a powder of the starting matreial is continuously released on top of the rotating rod through very hot flame. As more materials fed, the support rod is translating out of the flame and solidifcation occurs. Although, this method has the advantage of fast growth and simplicity but it does not produce high quality crystal as the growth rate in the Verneuil technique is usually much higher than other developed techniques. Therefore, other techniques such as Czochralski, Kyropoulos, Bridgman, Horizontally- directed solidification have been also widely studied. A comprehensive review of these technique is reported in several review papers and books [29, 30, 91, 97]. Despite all the efforts to improve the quality of sapphire crystal no perfect crystal was produced.

The characterization of a crystal yields knowledge of the nature and source of defects. This information can be used to refine the crystal growth process. X-ray topography is a well-known nondestructive imaging technique based on x-ray diffraction. Using this technique enables us to examine the crystal quality and monitor the lattice strains owing to defects. Using synchrotron radiation with well collimated and high flux beam enables large area transmission topography with high spatial resolution, which is not possible with most of laboratory x-ray generators [44]. In addition, a topograph obtained by using synchrotron radiation scan be recorded during an extremely short exposure time in few seconds or less. The basis for x-ray topography is the variations in intensity in individual diffracted spots due to structural nonuniformity in the lattice planes surrounding defects [98]. In the present study, we used crystals grown by several techniques and we used the synchrotron x-ray white beam transmission topography method to characterize strain and extended defects within the crystal volume of single crystals.

2.2 Experimental

In order to understand the reasons that limit the quality of sapphire crystals and select the best wafers a set of 38 crystals grown by different techniques was prepared. The crystals were grown by the Verneuil, Bridgman, Kyropoulos and Horizontally-directed solidification in the Shubnikov Institute of Crystallography, Moscow. Details of a few crystals are given in Table.3.1. The crystals grown by Kyropoulos, Verneuil, and Horizontally- directed solidification had pulling rates of 0.25-1, 10-15, and 6-10 mm/h, respectively and were cut from boules with diameters of around 20, 90 and 300 mm and lengths of 120, 200 and 500 mm, respectively. All the wafers were mechanically and/or chemically polished on both sides.

White beam topography was performed using a beam size of about 6×6 mm^2 at the TOPO-TOMO beam line at the ANKA synchrotron radiation source, Karlsruhe, Germany (transmission topography configuration, Fig. 2.1a [99]). For some of the crystals we further characterized the same crystal with a wider beam, the size of the crystal diameter, at BM05, ESRF. Fig. 2.1b shows the schematic white beam transmission topography setup. Synchrotron radiation at energies of 6-60 keV impinges upon the sapphire crystal and produces Laue spots on the film. Fig. 2.1c shows a sapphire after exposure. The black part can be easily removed from the surface of crystal. A lead beam stop has been used to absorb the direct beam. Since the spatial resolution decreases with the sample-film distance, this distance is usually small, in our case it is 8.7 cm. The topographs were detected on Slavich VRP-M film with grain size of 0.5 μm. In general, CCD detectors can also be used to record the topographs but have a lower resolution, more than 10 μm. Sets of planes which fulfil the Bragg condition produce one diffraction spot on the Laue pattern recorded on the film. In order to find the corresponding reflection we used a software package called LauePt [100]. An example of comparison of simulation and experimentally obtained reflections on a film is presented in Fig. 2.1d. Note that the simulation shows reflections in rhombohedral indices. Since it is common to use four indices for sapphire crystals, they are converted into pseudo-hexagonal notation in this report.

(a)

(b)

(c)

(d)
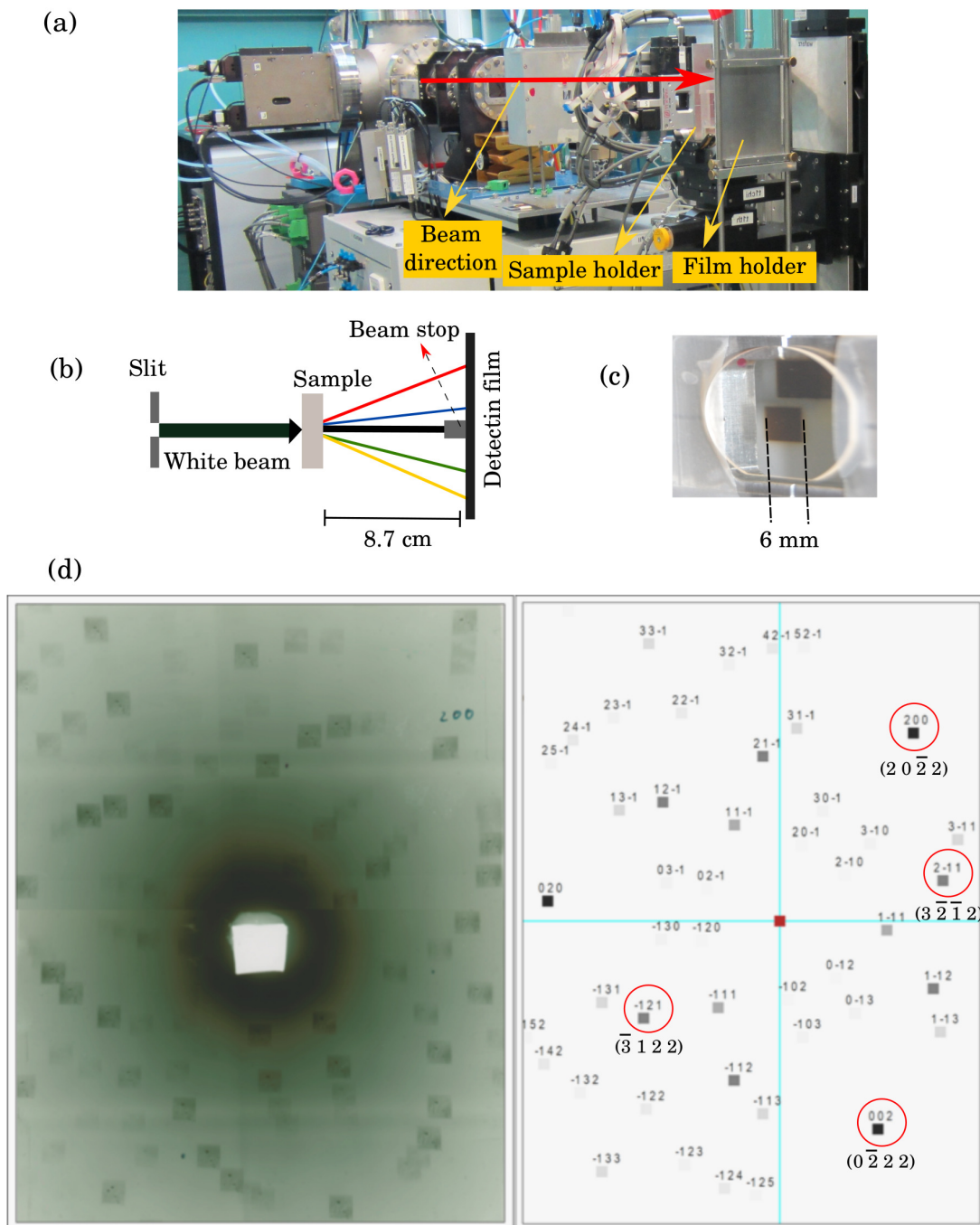
Figure 2.1: (a) TOPO-TOMO setup at the ANKA synchrotron source, Karlsruhe, Germany. (b) Schematic experimental setup for white beam topography in transmission geometry. (c) White beam profile (6×6 mm^2) on sapphire single crystal. (d) (Left) experimental and (right) simulated Laue patterns for wafer #1. Reflections are indexed in the rhombohedral setting. The equivalent hexagonal notation of a few of strong reflection are given in right side of the simulated Laue pattern.

Table 2.1: List of the sapphire crystals and their specifications. The Monocrystal (#11) was grown by Stavropol Inc.

# -No.,Name	Growth technique	Orientation	Dia^a(mm)/THK^b(mm)	Pulling rate (mm/h)	Post treatment
1-SK1C	Kyropoulos	(0001)	22/1	0.25-1	mechanical and chemical polishing
2-DP17	Kyropoulos	(01$\bar{1}$2)	40/1.1	0.25-1	mechanical and chemical polishing
3-SK2C	Kyropoulos	(0001)	30/1	0.25-1	mechanical and chemical polishing
4-SK24R	Kyropoulos	(10$\bar{1}$2)	35/3	0.25-1	chemical polishing
5-SHB12C	Bridgman	(0001)	27/2.5	-	mechanical polishing
6-SHB32C	Bridgman	(0001)	27/2.5	-	mechanical and chemical polishing
7-SK3R	Kyropoulos	(10$\bar{1}$2)	45/1	0.25-1	mechanical and chemical polishing
8-SHDC15-1	Horizontal directed solidification	(11$\bar{2}$0)	20/2	0.25-1	chemical polishing
9-SVA-1	Verneuil	(11$\bar{2}$0)	20/2	10-15	mechanical and chemical polishing
10-SVC-1	Verneuil	(0001)	20/2	10-15	mechanical polishing
11-Mono crys.	Modified Kyropoulos	(0001)	24/1	-	-

^{a}Diameter
^{b}Thickness

2.3 Results and Discussion

A. Overview

The crystalline quality of each sapphire single crystal was characterized by white beam topography. As some of the crystals showed very similar features, we show the topographs obtained from only a selection. Imperfection density or dislocation density for each of them has been estimated from the topographs. Practically, dislocation densities up to $\sim 10^4$ cm^{-2} can be measured. It is difficult to resolve dislocations when the density is between 10^5 and 10^6 cm^{-2} and when this value exceeds $\sim 10^6$ cm^{-2} the topograph becomes featureless and appears uniformly black.

Fig. 2.2 shows the white beam transmission topography results of crystals #1 to #5. The left side images reveal the overall quality across each crystal. The shape of defects in each of the crystals can be seen from the right hand insets.

Crystal #1 has a homogeneous distribution of curved shape defects, the surface orientation of this crystal is (0001), also called C plane, and it has been grown by the Kyropoulos method. The formation of curved dislocations is usually attributed to a too fast growth rate [101]. Curved dislocations are intermediate between the edge and screw dislocations. Edge and screw dislocations are two extreme forms of dislocations and can be visualized as extra planes inserted in the lattice where their slipping direction are perpendicular and parallel to the line of imperfection, respectively. The vector that defines the direction and magnitude of the slip is called Burgers vector (**b**). The edge dislocation lines are able to move along the direction of the Burgers vector under applied force by the resolved shear stress; *i.e.* the shear stress resolved along the slip direction on the slip plane, and form curved dislocations with screw and edge components. Note that the Burgers vector remains constant along the curved dislocation line and only the type of dislocation changes.

We estimated a dislocation density of 2-4 $\times 10^2$ cm^{-2}, which is a very small value for sapphire. Defects in crystalline solid are of several types: zero-dimension point defects, linear dislocation, planar grain boundaries, and three-dimension bulk defects. Dislocation is the major type of defects in our sapphire crystals. They are often much longer than the thickness of crystal hence they are mostly parallel to the C plane. Later, in this chapter we will discuss the shape and type of defects in this crystal.

Crystal #2 with surface orientation of (0 1 $\bar{1}$ 2), also grown by the Kyropoulos method, reveals an inhomogeneous distribution of dislocations which varies from $\sim 4\times 10^3$ cm^{-2} to $\sim 3\times 10^2$ cm^{-2} in left side of the topograph. From the small area topograph shown in inset, we can see the straight line and curved dislocations. Dislocations in sapphire are often seen with a curved shape while parallel straight dislocations have been observed only in a few cases. Qiang *et. al.* reported the observation of parallel groups of straight dislocations in a C-plane crystal grown by the temperature gradient technique [102]. The length of the dislocations is ≤ 1 mm and they are located in a plane inclined relative to the (0 1 $\bar{1}$ 2) the surface plane.

Crystal #3 with similar specification as the first crystal consists of uniformly distributed dislocations with a density in the order of 10^3 cm^{-2}. The formation of dense clusters of dislocations is related to high thermal fluctuation of the crystal during the crystallization process. The high thermal fluctuations results in non-directional stress, consequently, dislocations with different Burgers
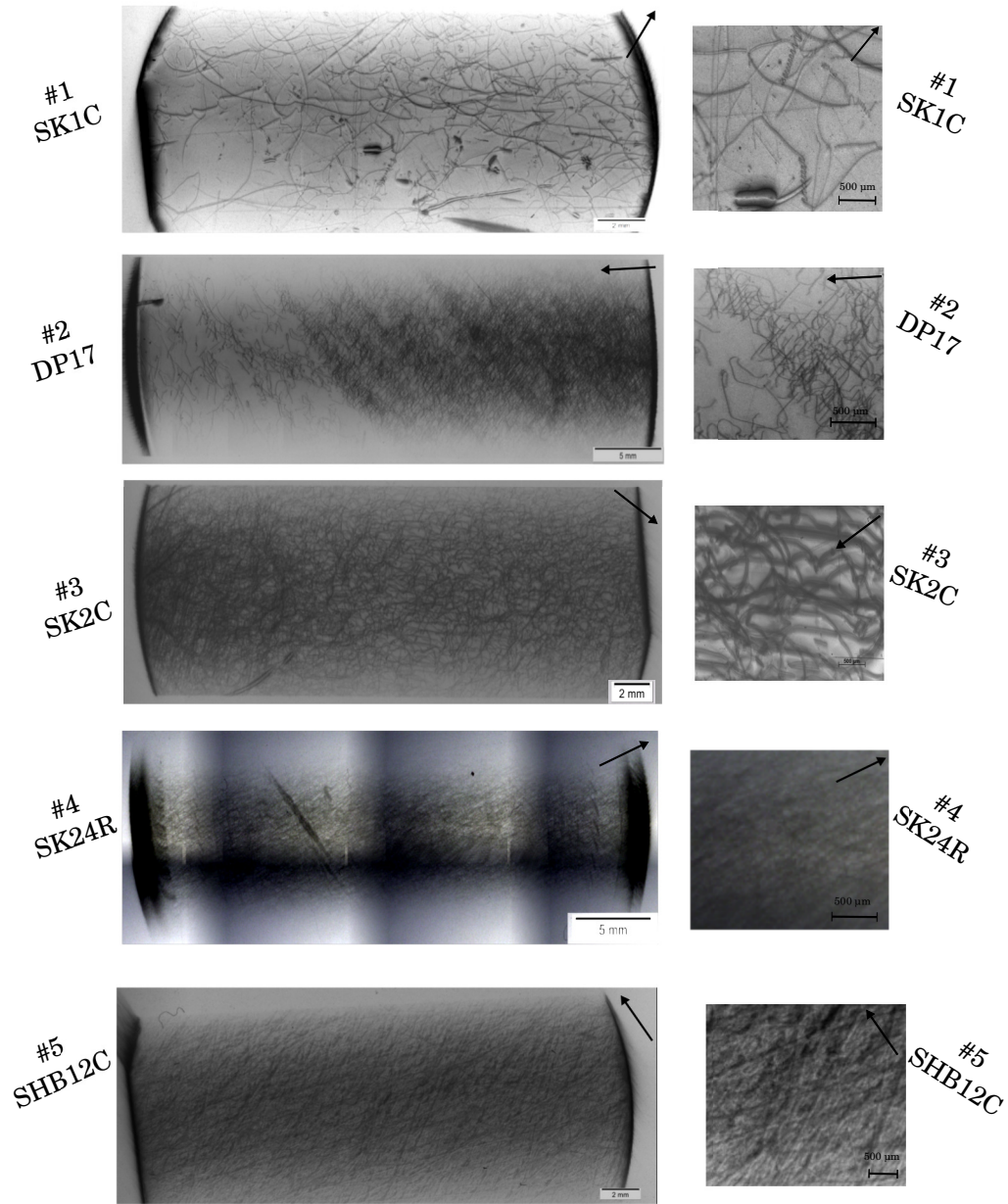
Figure 2.2: (a) White beam transmission topographs of crystals #1−#5.
(Left) Topographs have been recorded with a large beam at BM05,
ESRF. (Right) Topographs recorded with small beam at ANKA, KIT.
The black arrows on top right of each image shows the diffraction
vector, **g**.

vectors are formed in tangles [103]. We see similar features in the topograph of crystal #4. This
3 mm thick crystal has $(1\,0\,\bar{1}\,2)$ surface orientation and has been grown by the same technique as
the #1-3. The clusters are highly dense with a dislocation density $> 10^3$ cm^{-2}. This crystal has not
been mechanically polished which could be a reason for its poor quality.

The next two crystals with thickness of 2.5 mm are chosen from a batch of *C*-plane crystals grown

by the Bridgman method. Crystal #5 without chemical polishing looks very defective while crystal #6 which was treated chemically and mechanically revealed a better quality, see Fig. 2.3. The dislocation density of the latter is of the order of 10^3 cm^{-2}. The topographs of crystals #6-11 are shown in Fig. 2.3. Crystal #7 is an example of a Kyropoulos grown crystal which was treated chemically and mechanically but does not show good quality. Its poor quality most probably reflects the region of boule from which it was cut. A topograph of the crystal #8, grown by HDSM with growth direction of $(1\ 1\ \bar{2}\ 0)$ revealed a homogeneous distribution of dislocations with an estimated density of more than 10^5 -10^6 cm^{-2}. The lowest quality crystals have been obtained by the Verneuil method, crystals #9 and #10. Investigation of several reflections confirmed the presence of small angle grain boundaries in these crystals, which were not found in other crystals. The dislocation density is so high ($> 10^6$ cm^{-2}) that no single dislocation can be resolved. Very strong stress is evidenced by the deformation of the shape of topographs, see crystal #10 in Fig. 2.3. Diffraction by a crystal with grain boundaries forms a splitted topograph, *e.g.* reflection from the crystal #10 in the same Figure. A topograph recorded from one of the best commercially available crystal, crystal #11, presents a high dislocation density, more than 10^5-10^6 cm^{-2}, in contrast to estimated dislocation densities from Monocrystal, Stavropol, of better than 10^3 cm^{-2}. This large difference demonstrates how much more stringent the constraints are for x-ray rather than visible light optics applications. There is a homogeneous distribution of straight and curved dislocations across this wafer. In small regions the dislocation tangles become less dense.
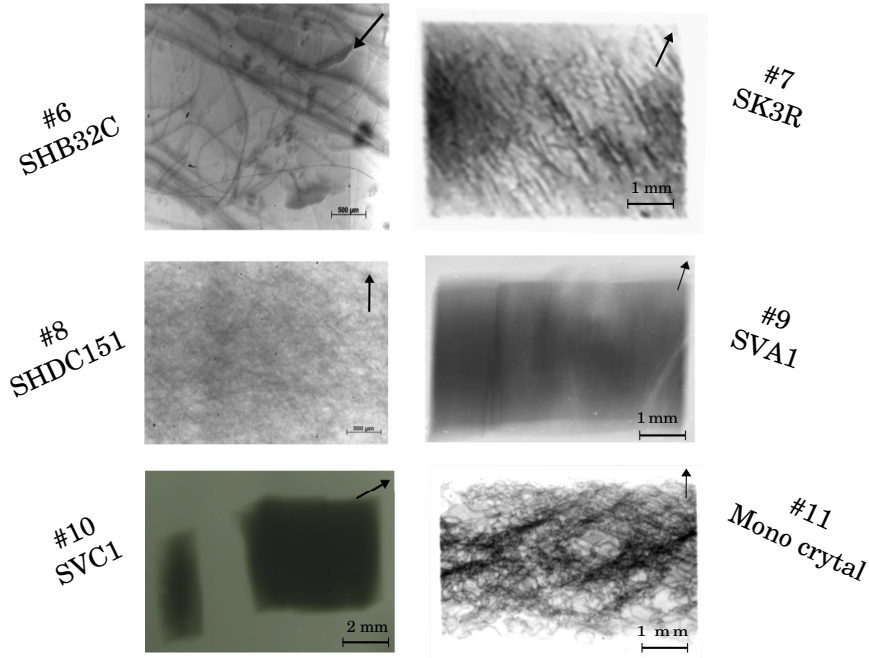

Figure 2.3: (a) White beam topographs #6-11 measured with small beam at ANKA, KIT. Crystal #11 is one of the claimed best commercial crystals.

We employed the method of white beam topography for quality assessment of all crystals and observed that crystals #1 has the highest quality. Also half of the crystal #2 has a very good quality.

B. Detailed inspection of the best crystas

White beam topography has been carried out in more detail for the whole area of the best two crystals. Fig. 2.4a presents the image of crystal #1, from the same side as it was shown in Fig. 2.2, which we call front side. There are three dislocation-free regions which are shown with colored ellipses. These regions are also seen from the back side of the crystal, see topograph shown in Fig. 2.4b. After looking at different reflections of these dislocation-free regions, we confirm that the number of dislocations is very low in these three regions and crystallites are perfect or nearly perfect. This crystal has been cut from the centre part of the boule, where the thermal gradient is minimum [104] (far from the seed). In the other areas of crystal #1, the agglomeration of defects (mainly dislocations) is uniform except the long black feature in the bottom right of the front side, which exhibits contrast from inclusions and can be seen from the back side too.

In contrast to the crystal #1, the distribution of dislocations changes dramatically from one side to other side in crystal #2, Fig. 2.5. Two region are selected and the topographs are magnified for a better visibility of dislocations. The dislocation density are estimated from summing the length of visible dislocations, marked with yellow lines. The obtained values are $\sim 1.5 \times 10^3$ cm^{-2} and $\sim 2.5 \times 10^2$ cm^{-2} for right and left images, respectively. It is known that the thermal gradient in the volume close to the periphery of the boule is higher than in the middle part. This can explains dramatic changes of quality in this crystal with 40 mm diameter, almost half of the size of its boule.

Let us now turn to the analysis of several different types of defects seen in crystal #1. In Fig. 2.6a we see several intense dark black contrasts with various size. These could be either contrast from inclusions, *i.e.* cluster of point defects, or large precipitate particles. In x-ray topographs they appear as two separated half-circles in black in a direct image [96]. As it was mentioned, the big black shape at the left bottom of Fig. 2.4a belongs to this type of the defects. Inclusions are among the most undesirable defects, since they deform dramatically the structure of the surrounding crystallites.

Dislocations are the main type of defect in the crystal #1 and often appear as curved lines. Fig. 2.6b shows a dislocation with a length of more than 2 mm and curved at its top part. We can see it as two parallel dislocations, joined at their ends. These two lines can be a dislocation dipole, *i.e.* an arrangement of two dislocations with opposite signs (net Burgers vector=zero) gliding on parallel planes at a very close distance. The elastic interaction between these two edge dislocations enhances the shear stress required to let them pass each other and if the subjected stress is not sufficient to trigger motion then the dislocations are trapped and form a dipole in a process called edge-trapping [105, 106]. The elastic energy of dipole dislocation is smaller than for single dislocations and its stress field decreases (with increasing distance) faster than that of straight individual dislocations. Dipoles are more energetically favoured than individual dislocations and when they break-up in a loop shape they can exit from the surface by annealing. Dipoles have been observed in sapphire [106] and magnesium oxide crystals [107]. Under special condition, their ends can make a curved dislocations and transfer its edge component to a screw component.

Lagerlöf *et al.* explained the formation of dipoles by a climbing dissociation process [106], the schematic diagram is shown in Fig. 2.7, taken from Ref. [106]. In Fig. 2.7a we see a dipole consisting of two parallel edge dislocations (hashed filled rectangles) in two planes. When the two ends of a dipole are pinched off by a climb, they form a U shape and are called a perfect dipole or a perfect loop, similar to an upside-down U shape in inset (b). Also, a faulted dipole or loop can
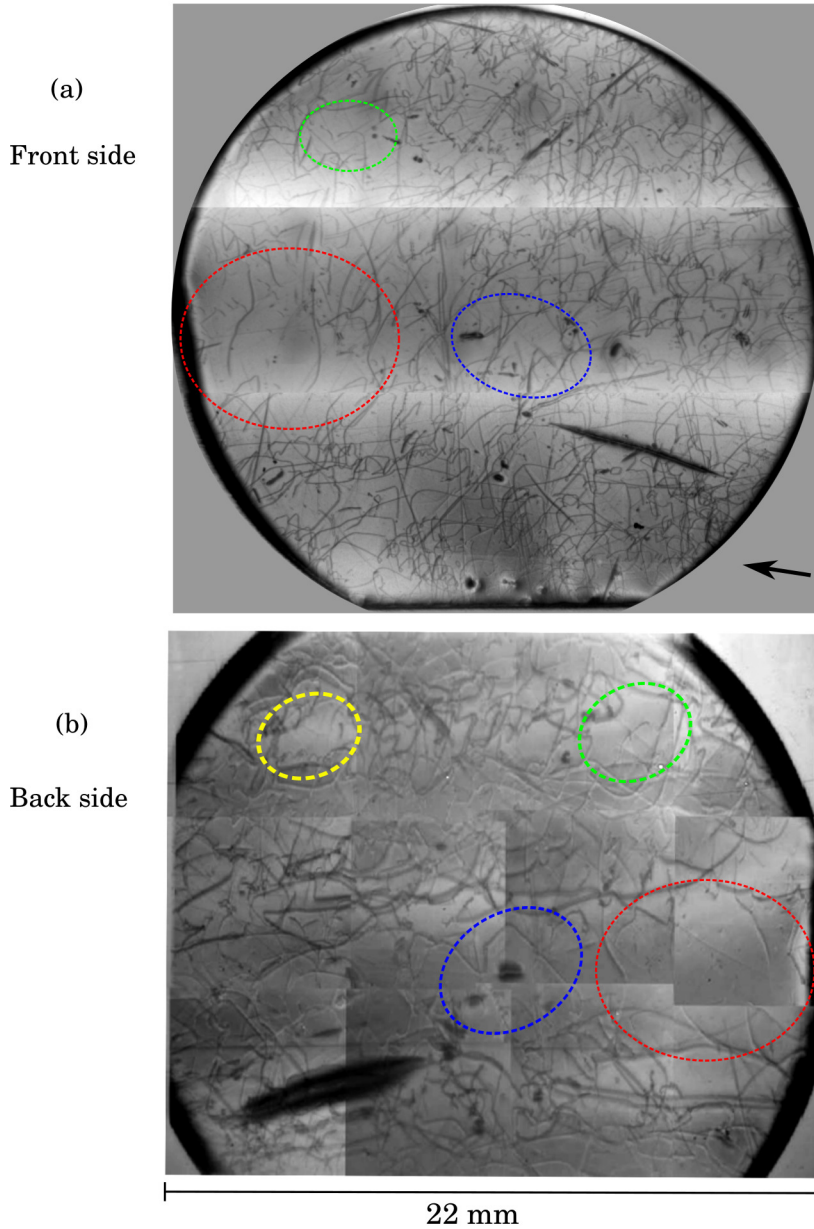
Figure 2.4: White beam topograoh of (a) front side and (b) back side of crystal #1 at different reflections. The colored ellipses indicate dislocation free regions seen from both side of the crystal.

form if the inner parts of the dislocation move towards each other, in both climb and glide moves, the dipole ends intersect and annihilate, see Fig.2.7c. A region marked with an arrow in Fig. 2.6c shows dislocations undergoing faulting process. The annihilation of dipoles may be related to the mobility of point defects at the highly curved area of the dipole. If the mobility is large enough to move away the point defects form perfect dipoles and if the mobility is low they may condense into faulted dipoles [108]. Dislocation dipoles in sapphire have been studied intensively in Refs. [106, 108, 109].
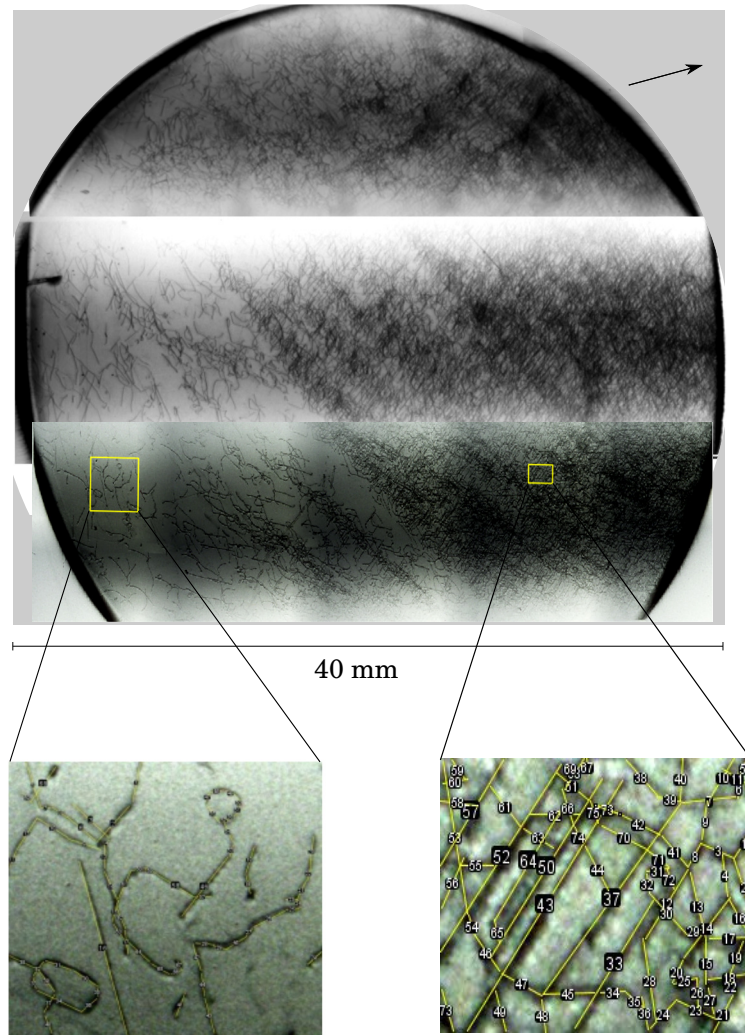
Figure 2.5: White beam topographs of crystal #2 at different reflections. Two regions of the topograph are enlarged in the bottom of the image. The yellow lines shows the dislocations, the dislocation density can be approximated by summing the length of these lines. Dislocation densities of $\sim 10^2$ and $\sim 10^3$ cm^{-2} have been estimated from the left and right images, respectively.

Dipoles can be a source of trails of loops, the formation of loops from dipoles is illustrated in a schematic diagram in Fig.2.7d taken from Ref.[110]. Fig. 2.6d shows an example of series of loops in crystal #1, that can be formed by a dipole break-up. The pinching off of dipoles by a cross slip mechanism may results in a row of loops which can be either vacancy or interstitial loops [111]. These loops are usually prismatic loops where the Burgers vector is not in the loop plane, and can be shrinked and annihilated by lattice diffusion via annealing [112]. It is energetically favourable for a dislocation dipole to break-up into a row of dislocation [113]. Such a loop can also originat from helical dislocations. Helices can be a transformed to loops under special circumstances like thermal stress. In this case we should expect very few loops, maximum three [114]. However, in

(a)   (b)

(c)   (d)
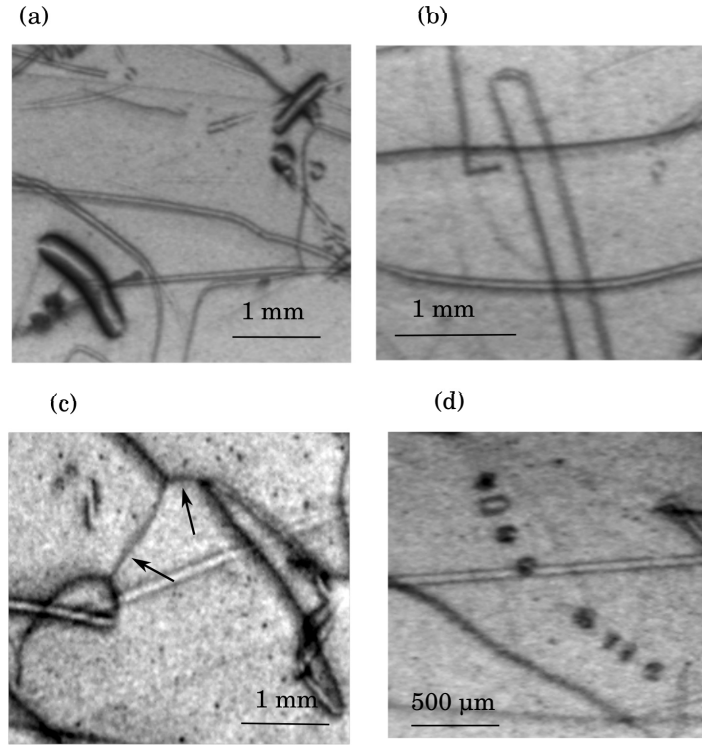
Figure 2.6: Dislocations in crystal #1.(a) Defects as broken ellipses or circles with intense dark black contrasts. (b) An example of two parallel dislocation, could be a dipole. (c) Dislocations joint at their ends, shown by arrows. (d) A row of closed loops.

our case we observe a row of loops which perhaps resulted from interaction of two parallel helices with opposite twist. The interactions between two opposite rotation can yield closed loops [114]. In the next paragraph, more details about the helical dislocation will be given.

Fig. 2.8a-d present helically shaped dislocations in crystal #1 with different shapes and number of turns. These helices are another type of dislocation in sapphire which were first observed in 1971 [115]; they only appear in very high quality crystals [114]. We observed them when the dislocation density is less than 10^3 cm^{-2}. When a screw dislocation is subjected to absorption or emission of vacancies or dopant inhomogeneity [116] they have the possibility to climb along their Burgers vectors. If both ends of the dislocation are pinned in two planes (similar to dipoles) and be subjected to large chemical stress a straight dislocation line can be turned to a helix. Screw dislocations are more mobile than edge dislocations, thus it is easier for them to move and make turns of helices [114, 116]. Fig. 2.8a-c show three helical dislocations at different level of formation. In inset (a), we see a helix with only two turns that seems to be at the starting point of its formation, whereas that in inset (b) exhibits more turns. Helices can also unwind towards lines. In that case, we expect to see changes of curved lines to straight lines, supposedly due to relaxation, but as we do not observe many straight dislocations, the former idea of dislocations evolving from linear to helical has more merit. A helix with many compact turns can be formed as for example shown in Fig. 2.8c. This could be the result of a variation in different parts of the crystal subjected to large thermal stress. A simulation of thermal stress for the Kyropoulos grown crystals showed that near
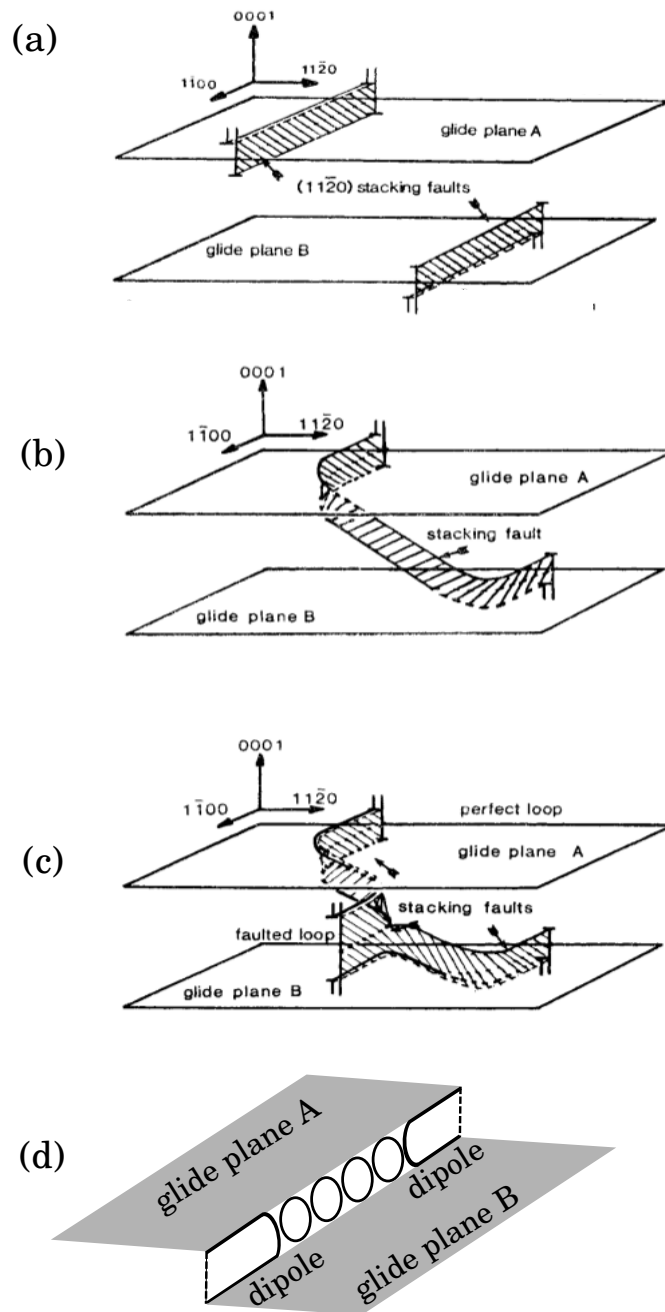
Figure 2.7: (a) Schematic representation of a dipole edge-trapped between glide planes A and B. Diagrams of formation of (b) a perfect loop and (c) faulted loop at the end of a dipole, pictures are taken from Ref. [106]. (d) Simple representation of the transformation of dipoles into a trail of loops [110].

the crystallization interface, at the shouldering location, the tailing location of a boule experiences high thermal stresses [117]. It is also possible to observe a helical dislocation with an invisible helix axis, the line along the direction of a helix, an example shown in Fig. 2.8d. In this particular

case, the axis is not detected either due to the diffrcation conditions or the axis is an annihilated part of dislocation after interacting with another helix with an opposite twist [114].
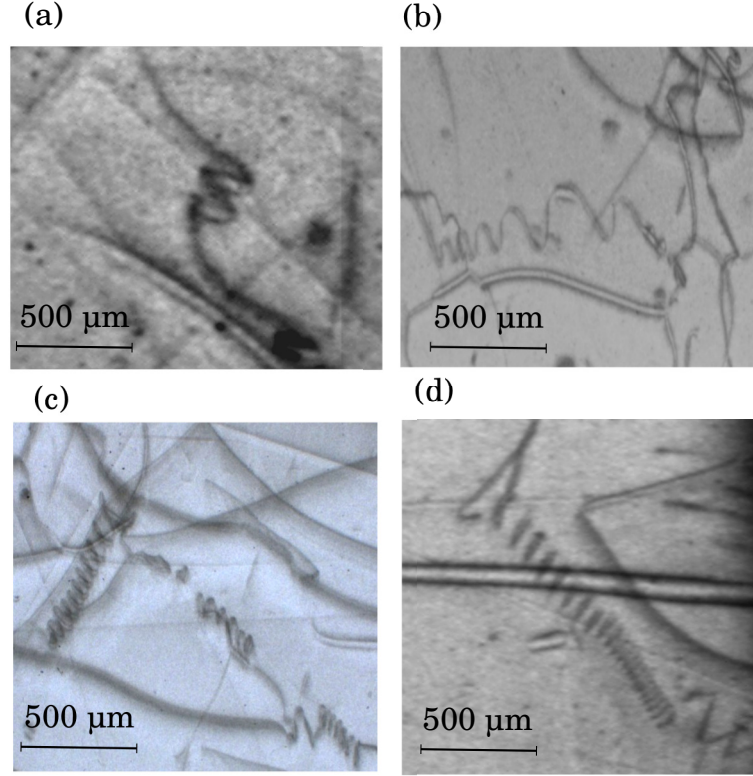
Figure 2.8: Helical dislocations in crystal #1. (a) A twisted dislocation which forms two loops of a helical dislocation. (b) An example of helical dislocation with open loops with different diameter. (c) A helix with greater number of turns. (d) An example of helical dislocation with invisible axis.

From several topography images one can determine the Burgers vector $\mathbf{b}$, the essential parameter of a dislocation. The determination of a Burgers vector can be obtained by applying the condition $\mathbf{g} \cdot \mathbf{b} = 0$, where $\mathbf{g}$ is the diffraction vector. In screw type dislocations $\mathbf{b}$ is parallel to the dislocation line vector, $\mathbf{u}$, and they are invisible when $\mathbf{b}$ is perpendicuar to $\mathbf{g}$. In edge type dislocations $\mathbf{b}$ is perpendicular to $\mathbf{u}$ and dislocations show no contrast when the condition $\mathbf{g} \cdot \mathbf{b} \times \mathbf{u} = 0$ is fulfilled.

We show some selected topographs of the same region of sample #1 which has the best quality among the studied crystals, in Fig. 2.9a. For a better distinguishability, blue lines are drawn next to the studied dislocations. Dislocations indicated as a and b exhibit no contrast in the reflection $(0\ \bar{2}\ 2\ 2)$ and show contrast in the other reflections. In addition, we know the possible directions of dislocations and Burger vectors of dislocations in sapphire single crystals from an earlier study [102, 118]. So the Burgers vector of a and b are parallel to $[2\ \bar{1}\ \bar{1}\ 0]$. Dislocations labelled c and d shows strong contrast in reflections $(0\ \bar{2}\ 2\ 2)$, $(\bar{1}\ 4\ \bar{3}\ 4)$, and $(\bar{2}\ 4\ \bar{2}\ 3)$ but are invisible in $(2\ 0\ \bar{2}\ 2)$, thus the Burgers vectors $[\bar{1}\ 2\ \bar{1}\ 0]$ is justified. In the same manner, the helical dislocation e is invisible in $(\bar{2}\ 2\ 0\ 2)$ so its Burgers vector is parallel to $[1\ 1\ \bar{2}\ 0]$.
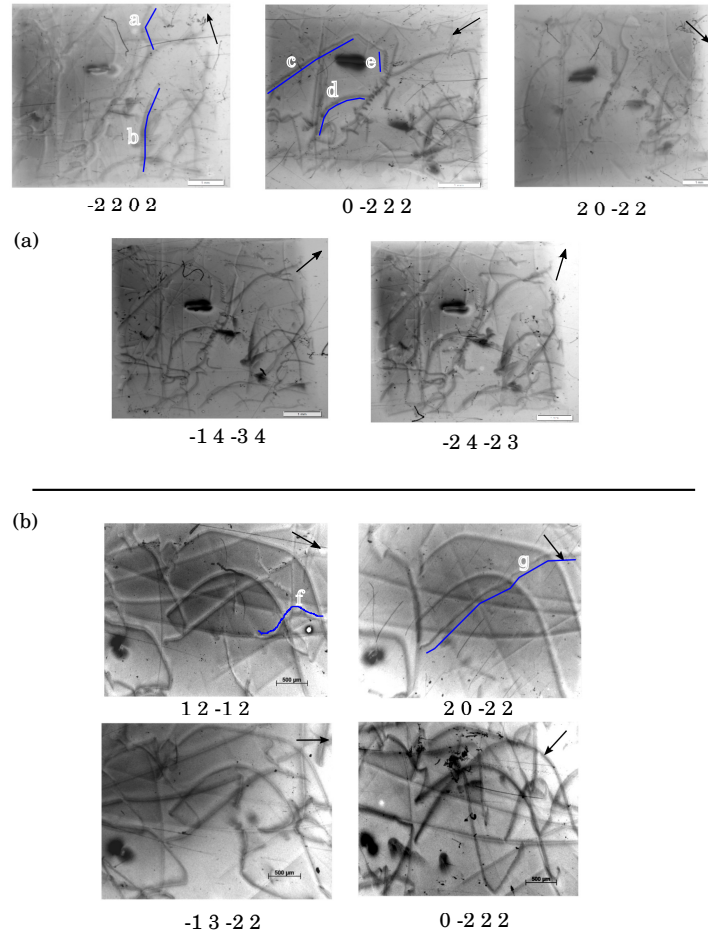
Figure 2.9: (a) Different reflections recorded form one part of the crystal #1. (b) Four reflections selected from different region of the same crystal. The Burgers vectors of dislocations *a-g* belong to the $< 2\bar{1}\,\bar{1}0 >$ class. Most of the detected dislocations have both edge and screws components; these are mixed dislocations.

Four reflections obtained in another region of same crystal are shown in Fig. 2.9b. Dislocation *f* and beveled dislocation *g* are invisible in $(2\,0\,\bar{2}\,2)$ and $(0\,\bar{2}\,2\,2)$, respectively. One can say that the Burgers vector of dislocations *a-g* belong to the $< 2\,\bar{1}\,\bar{1}\,0 >$ class, one of two reported Burgers vectors in this sapphire crystals [102, 118]. The second Burgers vector of dislocations in sapphire is $< 1\,0\,\bar{1}\,0 >$. After finding the Burgers vector, we can determine the characteristics of some of dislocations. The Burgers vector of dislocation *c* has 30° angle with dislocation line and it becomes invisible when **g** vector is perpendicular to the Burgers vector in reflection $(2\,0\,\bar{2}\,2)$. Thus, dislocation *c* is a 30° screw dislocation. The dislocation line of *e* is parallel to $[\bar{2}\,2\,0\,2]$ and perpendicular to its Burgers vector. As dislocation *e* disappears in reflection $(\bar{2}\,2\,0\,2)$ it is a pure edge dislocation. Helical dislocations in sapphire are mainly of edge character [115]. Dislocation *g* with the dislocation line nearly parallel to $[0\,\bar{2}\,2\,2]$ and Burgers vector parallel to $[2\,\bar{1}\,\bar{1}\,0]$ is an edge dislocation. The curved shape dislocation often are mixed dislocation of edge and screw types. Summing up the results, it can be concluded that crystals consist of similar dislocations to

the high quality sapphire crystals in earlier studies. The dislocation density for some of our crystals indicates their superior quality.

2.4 Conclusion

X-ray investigations of the real structure in sapphire have been performed for a batch of crystals synthesized by almost all known growth techniques. White beam topography of several crystals showed that the main defect type is dislocations, which appear as straight lines, curves, and helical shapes. We could identify a Burgers vector of $< 2\,\bar{1}\,\bar{1}\,0 >$ using the dislocation contrast criteria for some of the dislocations. The average dislocation densities are linked to the growth techniques and pulling rates. Studies on several wafers grown by same technique showed similar features and dislocation densities. The best crystal has been grown by the Kyropoulos technique. Crystal #1 with (0 0 0 1) surface plane with average dislocation density of a few 10×10^2 cm^{-2} consists of several dislocation free regions. Nearly perfect area of this size were not found in other crystals, but a dislocation density in order of 1.5×10^2 cm^{-2} has been observed in crystal #2, too. The findings suggest that (nearly) perfect crystals in large volume can be obtained using the Kyropoulos technique. It is desirable to cut the sapphire parallel to its (0 0 0 1) plane to minimize the effect of dislocations on the d-spacing variations.

Chapter 3

Backscattering Rocking Curve Imaging
of High Quality Sapphire Single Crystals

abstract

We report on the characterization of high quality sapphire single crystals suitable for high-resolution x-ray optics at high energy. Investigation using rocking curve imaging reveals good quality of the crystals with sensitivity to the lattice spacing parameter variation of $\delta d/d \sim 10^{-4}$. The investigation using backscattering rocking curve imaging with lattice spacing resolution of $\delta d/d \sim 5 \times 10^{-8}$ shows very diverse quality maps for all crystals. Our results highlight nearly ideal areas with an edge length of 0.2-0.5 mm in most crystals. Comparison of the back reflection peak positions shows that even neighboring ideal areas exhibit a relative difference in the lattice parameters of the order of $\delta d/d = $10-20 $\times 10^{-8}$, which is several times larger than the rocking curve width. Stress-strain analysis suggests that an extremely stringent limit on the strain at a level of ~ 100 kPa in the growth process is required in order to produce crystals with large areas of the quality required for x-ray optics at high energy

A Jafari[1,2,3], I. Sergueev[4], D. Bessas [3], B. Klobes [1], P. Alexeev [1,4], B. S. Roschin [5], V. E. Asadchikov [5,6], J. Härtwig [3], H-C. Wille[4], A. Chumakov [3], and R. P. Hermann[2,7]

[1]*Jülich Centre for Neutron Science JCNS and Peter Grünberg Institut PGI, JARA-FIT, Forschungszentrum Jülich GmbH, 52425 Jülich, Germany*

[2] *Faculté des Sciences, Université de Liège - 4000 Liège, Belgium*

[3]*ESRF- The European Synchrotron, 38043 Grenoble Cedex 9, France*

[4]*Deutsches Elektronen-Synchrotron, 22607 Hamburg, Germany*

[5]*Shubnikov Institute of Crystallography RAS, 119333 Leninskii pr-t 59, Moscow, Russia*

[6]*Lomonosov Moscow State University, Faculty of Physics, 119991, GSP-1, 1-2 Leninskiye Gory, Moscow, Russia*

[7]*Materials Science and Technology Division, Oak Ridge National Laboratory, Oak Ridge, Tennessee 37831, USA*

3.1 Introduction

White sapphire, *i.e.* α-Al$_2$O$_3$ corundum, single crystals have excellent pressure and temperature stability, extreme hardness, high transparency and high dielectric constant. As such they are suitable for many advanced optical applications like medical lenses [119], LEDs [91], electronic substrates [120, 121], and focusing devices [122, 123]. Sapphire is a promising candidate for hard x-ray optical applications [124], high pressure cells for neutron scattering experiments [125, 126] and optical windows in corrosive atmospheres [127, 128]. Sapphire single crystals with low- to medium- optical quality can satisfy many demands whereas production in the highest quality is still an unreached milestone. An emerging application of sapphire is relevant to x-ray monochromatization. Currently, common x-ray monochromators based on silicon and germanium have significant limitations for application in x-ray inelastic scattering due to their high crystal symmetry. For Resonant Inelastic X-ray Scattering (RIXS) and Nuclear Resonant Scattering (NRS) the relevant probe beam energies are defines by the elemental absorption edge and by specific nuclear resonance energies, respectively. Unfortunately in most cases, the probe beam energy can not be chosen to match energies favorable for Si-based optics. Both the RIXS and NIS methods require x-ray optics as analyzers [19] or monochromators [17] based on low symmetry crystals such as α-quartz or sapphire, crystals which enable a quasi-continuous choice of high resolution x-ray beams. For NIS, sapphire is currently the only explored high-efficiency choice for energies above 30 keV because of the high Debye-Waller factor that ensures high reflectivity. Note that multiple-crystal Si monochromators often used at 10-25 keV are possible for few particular energies above 30 keV [129], however, with comparatively very limited spectral reflectivity.

Several nuclear transitions with energies above 30 keV can be investigated by NIS, in particular, the transitions of ^{125}Te at the energy of 35.49 keV [20, 130], of ^{121}Sb at 37.13 keV [20, 131] and of ^{129}Xe [132] at 39.6 keV. Theoretical calculations [17] predicts for the sapphire backscattering monochromator an energy bandwidth of 0.3-0.7 meV, *i.e.* $\delta E/E$ =1-2 $\times 10^{-8}$ for these energies. In 2005, the first Nuclear Forward Scattering (NFS) signal at 37.13 keV (^{121}Sb nuclear transition) using a sapphire backscattering monochromator has been recorded at the nuclear resonance scattering beamline, ID18 at the ESRF [21], with a 7 meV bandwidth [62]. In 2007, NIS at the same energy with an improved resolution of 4.5 meV was reported [131]. NIS experiments at 35.49 keV (^{125}Te nuclear transition) have been carried out with 7.5 and 6.6 meV energy resolution at BL09XU at SPring-8 [94] and at at the nuclear resonance scattering station ID22N, ESRF [130], respectively. Thus, attempts to use sapphire as a high resolution monochromator for NIS show that the main limiting factor is the quality of available crystals, which is ten times worse than the theoretical expectation. It was shown that it is possible to achieve $\delta E/E \sim 2 \times 10^{-8}$ using particular small volumes in the best crystal [20], at the cost of additional focusing optics. Energy bandwidths of 1.2, 1.1, and 0.95 meV were obtained at 37.13 [20], 35.49 [20], and 39.6 keV [20] (^{121}Sb, ^{125}Te, and ^{129}Xe nuclear transitions), respectively. However, the possibility to reproduce the same resolution with other sapphire crystals and achieving the theoretical energy resolution, which is factor 2 better than in the last studies, are questionable.

The difficulty in growing sapphire crystals could be related to a binary composition requiring two elements, Al and O, as compared to the crystals like silicon required only one element. Also, the high viscosity of molten sapphire[133] (1.8×10^{-5} m^{2}s^{-1}) may emerge lattice defects easier than low viscosity materials *e.g.* silicon[134] with 3×10^{-7} m^{2}s^{-1}. Furthermore, the relatively high melt-

ing temperature of 2303 K certainly makes the control of thermal gradients more challenging. The quality of the sapphire crystals clearly depends on the production method. A wide range of growth techniques have been refined, such as Czochralski, Kyropoulos, and heat exchanger methods, in order to overcome the crystal quality related to growth issues [30, 34, 91]. The crucible and insulation material, the purity of the raw material, the growth rate and temperature gradients control are the main parameters for the growth of high quality crystals. Several numerical analysis studies of the Kyropoulos technique estimating the temperature gradient, the temperature of the reactor [34] and the thermal stress distribution [117], have aimed at defining how to produce improved sapphire crystals. These studies reveal high thermal stresses at the interface of the seed and crystal as well as at the shoulder and at the bottom part of the boule. Limited improvements have been achieved and extensive reviews on sapphire growth and applications are documented [97, 135].

Quantifying and understanding imperfections in single crystals calls for advanced characterization methods. Their non-destructive nature makes several x-ray based techniques well suited. x-ray diffraction topography using either a polychromatic (white radiation) or a monochromatic beam, is an imaging technique based on Bragg diffraction.

The rocking curve evaluation with a monochromatic beam is one of the most used technique for quantitative measurement of crystalline perfection, with one of the first study of rocking curves measurement of a ruby crystal (Al_2O_3) documented in 1965 [136]. P.M. Adams *et al.* reported the effects of dislocations, residual grinding, polishing, mosaic structure and twinning on the crystal quality[137]. Quality assessment of several sapphire substrates revealed a full width at half maximum (FWHM) of the rocking curves in the range of a few ten arc-sec to arc-min [137]. Further on, all angular and energy widths quoted as FWHM. A combination of x-ray diffraction rocking curves and atomic force microscopy (AFM) showed that sapphire wafers treated with chemo-mechanical polishing with subsequent chemical etching have better surface smoothness compared to those treated only by mechanical polishing or by chemo-mechanical polishing [138]. Nowadays, a large number of topographs can be recorded by a CCD camera in a Rocking Curve Imaging (RCI) setup at synchrotron radiation facilities [51]. These topographs can be analyzed with PC-based softwares to rapidly reveal a wealth of information.

Sapphires suitable as a high resolution monochromator require quantitative RCI with resolution of $\delta d/d \sim 10^{-7}$-10^{-8} which corresponds to the theoretically expected $\delta E/E$. Such high sensitivity requires Bragg reflections with small width of 0.02-0.2 arcsec [139]. These measurements are challenging even with synchrotron radiation sources. One way to achieve the required sensitivity is to use backscattering RCI, where the investigated crystal is installed in backscattering diffraction geometry and the rocking curve measurements are performed by variation of the incoming x-ray energy using multiple-crystal Si high-resolution monochromators (HRM) with $\delta E/E \sim$ 3-6 $\times10^{-8}$. In backscattering geometry, reflections with Bragg angle very close to 90° are used. The advantage of backscattering RCI is that due to the large angular acceptance of the back reflections, the reflectivity becomes insensitive to the lattice inclination and depends only on the lattice variation $\delta d/d$.

By taking advantage of the features of the RCI and the backscattering geometry, the intrinsic energy widths of the reflectivity curves have been evaluated with a resolution of $\delta E/E \sim 10^{-7}$-10^{-8} in quartz [57], diamond [58] and sapphire [20]. The last study has evaluated imperfections in *C*-plane sapphire crystal, *i.e.* with [0 0 0 1] direction as surface normal, with a small beam of

Table 3.1: Characteristics of the investigated sapphire crystals, and the Bragg reflection used. δE is the intrinsic theoretical bandwidth.

Crystal #	Growth technique	Surface plane	Diameter/ Thickness(mm)	Reflection	Extinction length(μm)	δE (meV)
1	Kyropoulos	(0001)	22/1	0 1 $\bar{1}$ 50	145	1.57
2	Kyropoulos	(01$\bar{1}$2)	40/1.1	7 10 $\bar{17}$ 18	130	1.71
3	Bridgman	(0001)	27/2.5	0 1 $\bar{1}$ 50	145	1.57
4	Kyropoulos	(0001)	30/1	0 1 $\bar{1}$ 50	145	1.57
5	Kyropoulos	(10$\bar{1}$2)	30/3	7 10 $\bar{17}$ 18	130	1.71

0.1×0.2 mm^2 and spatial resolution of 0.4 mm using slits after a high resolution monochromator operating at 23.9 keV [20]. The sapphire crystal studied therein has a few high quality spots which makes it suitable as backscattering monochromator at the beamline ID18, ESRF.

In this study, we report on the quality assessment of sapphire crystals with the purpose of monochromatization of a synchrotron x-ray beam at high energies. We show a quantitative analysis of the crystalline quality using different topography techniques and in particular demonstrate the use of high-throughput backscattering RCI over large areas with spatial resolution of 0.055 mm. We found small areas with almost perfect crystallites in several crystals. A relative stress in the order of 40(5) kPa is determined, stress which causes displacements in d-spacing even in these nearly ideal crystallites.

3.2 Experimental

We investigated the quality of five sapphire single crystals grown by the Kyropoulos and Bridgman techniques, see crystal details in Table 3.1. These crystals were grown in the Shubnikov Institute of Crystallography in Moscow and selected from a batch studied by white beam topography (WBT), reported in [140].

First, the crystal #1 was characterized by the RCI at the beamline BM05, ESRF. The schematic setup for this experiment is shown in Fig. 3.1a. In the RCI setup the 20 keV beam coming from the silicon high heat load monochromator (HHLM), with chosen Si(1 1 1) reflections is diffracted by the sapphire when it fulfils the Bragg condition of the reflection (0 0 0 6) with Bragg angle 8.2°, (*hkil*) indices are given for the sapphire reflections, where $i = -(h + k)$. The intrinsic angular width of this reflection is 0.3 arcsec. However, due to the energy bandwidth of the upstream monochromator of $\sim$ 2.8 eV, the rocking curve width for the ideal crystal is expected to be 4 arcsec. Thus, the sensitivity of the method to the lattice spacing can be obtained [139] as $\delta d/d = (\Gamma)/\tan\theta_B \sim 10^{-4}$, where Γ is the rocking curve width.

An image is recorded in the CCD detector for each angular step of $\sim$ 0.9 arcsec. By rocking the sapphire crystal, sequences of topographs were recorded and then assembled to yield a topograph of the entire crystal. We used the Visrock program for numerical analysis of sequences of digital x-ray images [53].

The same crystal was studied using white beam topography in transmission geometry using a large beam size in order to assess the overall quality across the crystals. This study was performed at BM05, ESRF.

The schematic backscattering RCI setup designed at the beamline ID18, ESRF is depicted in Fig. 3.1b. The beam after the HHLM was further monochromatized by a multiple-crystal channel-cut Si HRM [141]. The energy of the HRM was chosen between 23.840 and 23.905 keV in order to match the sapphire backscattering reflections listed in Table 1. The theoretical energy bandwidth of the HRM is 0.7 meV. Experimentally, bandwidth of 0.9 meV has been measured using nuclear resonance scattering on ^{119}Sn at 23.88 keV. The deviation from the theoretical value is due to the imperfections of the Si crystals across the beam spot and an energy bandwidth of 0.7 meV is expected for small parts of the beam. The sharp energy bandwidth of the HRM provides high lattice spacing resolution of $|\delta d/d| = |\delta E/E| = 3 \times 10^{-8}$.
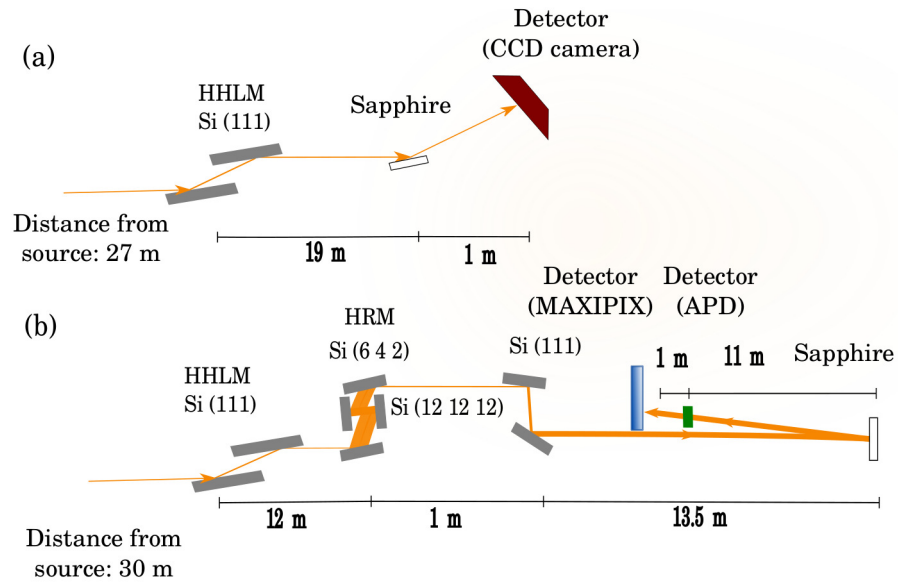
Figure 3.1: A schematic representation of the setup of the rocking curve imaging at BM05, ESRF. A silicon high heat load monochromator (HHLM) of two Si(111) reflections was used to adjust the synchrotron radiation to an energy of 20 keV. The sapphire was located close to the CCD detector. (b) Schematic view of the backscattering RCI experimental setup at ID18, ESRF. Starting left and following the beam (yellow): high heat load monochromator, high-resolution monochromator (HRM), asymmetrically cut Si(111) crystals with b_{total}=10, the sapphire crystal under study, avalanche photodiode (APD) detector, and MaxiPix detector. The diffracted intensity from back reflections of sapphire have been recorded by MaxiPix detector after moving the APD detector out of the beam.

In order to cover a large area on the investigated crystals, the beam downstream of the HRM has been enlarged in the vertical direction by using two asymmetric Si (111) reflections with combined asymmetry parameter, b_{total} =10. The beam at the studied crystals had a width size of $\sim 1.9 \times 2.5$ mm^2 (H×V). The beam back-reflected by the sapphire was collected by a 2-dimensional MaxiPix detector, with 55×55 μm^2 pixel size, installed in near backscattering geometry with a Bragg angle θ_B of 89.90°. The intensity in each pixel was measured as a function of incoming energy tuned by the HRM with an energy step of 0.5 meV while the sapphire crystal stayed at rest and constant temperature. Thus, a set of rocking curves for 4×3.5 mm ^{2} (H×V) spots on the sapphire crystal was obtained with a spatial resolution of 55 μm. The data sets were analyzed and maps of the rocking curve width and of the maximum position were recorded. In order to characterize the entire surface, the crystal was moved in the transverse directions relative to the beam and the same measurements were repeated.

3.3 Results

The map of the rocking curve widths measured by RCI for crystal #1 is shown in Fig. 3.2a. The straight line (pointed by a black filled arrow) and the yellow area below it are artifacts caused by diffraction from the sample holder. The map shows that the width in most of the crystal varies between 3.3 and 4.3 arcsec (blue and red colors) which is comparable or better than the theoretically expected value of 4 arcsec. This result is, probably, due to the smaller energy bandwidth of the beam after HHLM. Thus, for most of the crystal, the broadening of the reflection is not more than 30 % of the ideal width. The reasonable quality with a precision of $\delta d/d = 10^{-4}$ is also confirmed by the rocking curves shown in Fig. 3.2b. These rocking curves were acquired at four individual spots, 1-4 in Fig 3.2a and normalized to the maximum intensity. The rocking curves at spots 1 and 2 have a symmetric ideal shapes with widths of$\sim$ 3.6 arcsec. Almost the same width is observed for the spot 3. Only the rocking curve at spot 4 shows broadening mainly due to the presence of two peaks corresponding to areas with different lattice spacing or with misorienation of the lattice planes. If this effect would corresponds to the variation of the lattice spacing, the difference of the lattice spacing can be estimated as $\delta d/d \sim 1.6 \times 10^{-4}$.
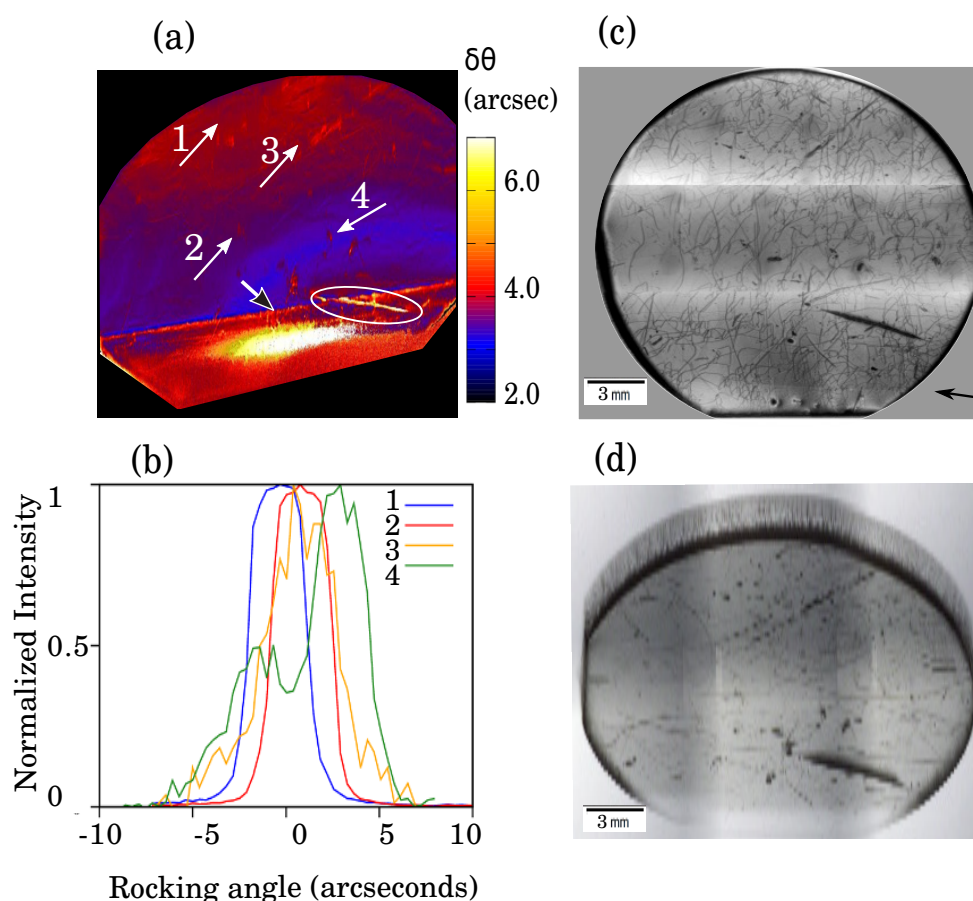
Figure 3.2: (a) The map of the rocking curve widths obtained from crystal #1 using rocking curve imaging, (b) rocking curves taken at spots labeled in (a), (c) white beam topograph in transmission, Laue, geometry; (d) monochromatic beam topograph recorded at the slope of the rocking curve with rocking curve imaging setup in reflection, Bragg, geometry.

Higher sensitivity to defects can be obtained by an investigation of the topograph performed at the slope of the rocking curve [142]. The topograph of crystal #1 taken in reflection, Bragg, geometry is shown in Fig. 3.2d together with the white beam topograph shown in Fig. 3.2c. Both topographs show significant amounts of defects not visible in the map of rocking curve widths. The defects do not always correlate in both topographs. This has several reasons. One is related to the fact that white beam topograph was done in reflection geometry and the other in transmission geometry. A second reason is the fact that there are extinction rules. A defect is only visible if it deforms the diffracting lattice planes (hkl). If the hkl indices are different then one is sensitive (or insensitive) to different components of the strain-field of the given defect. So it is a direct consequence that the visible or invisible details of a defect image must not be the same in two images taken with a different diffraction (diffraction vector, normal to the diffraction plane). Deep-level defects are only visible in Laue white beam topographs and those that can be seen in monochromatic beam topographs are shallow-level defects. Dislocations are the main type of defects in this crystal [140].

In order to test the feasibility of the method, the backscattering topography was first applied to a Ge crystal which has almost ideal quality. Here, the Ge(5 15 15) reflection was used at the energy of 23.880 keV with an intrinsic width of 2.85 meV ($\delta E/E = 12 \times 10^{-8}$). For each pixel the widths of the rocking curve and positions of the maximum of the curves were determined and the corresponding maps are displayed in Fig. 3.3a, b in units of relative lattice parameter variation, $\delta d/d$ which is equivalent to $\delta E/E$. In addition, examples of rocking curves obtained at a few labeled pixels are shown in Fig. 3.3c. The width of the reflection is very uniform across the area with the exception of the lines (yellow color) where a larger width is observed. These lines are due to the scratches on the surfaces visible by eye. The average value of the widths through good areas is 3.2 meV which is close to the theoretical value of 2.85 meV. The position of the reflection maximum is also the same across the good areas of the crystal and shifted by up to 2 meV at the scratches. The shift is due to the decrease of the lattice constant at the scratches on the order of $\delta d/d \sim 5 \times 10^{-8}$. This study shows that, indeed, this imaging backscattering topography setup can provide reliable information about crystal quality with a relative precision of 10^{-7}-10^{-8}.
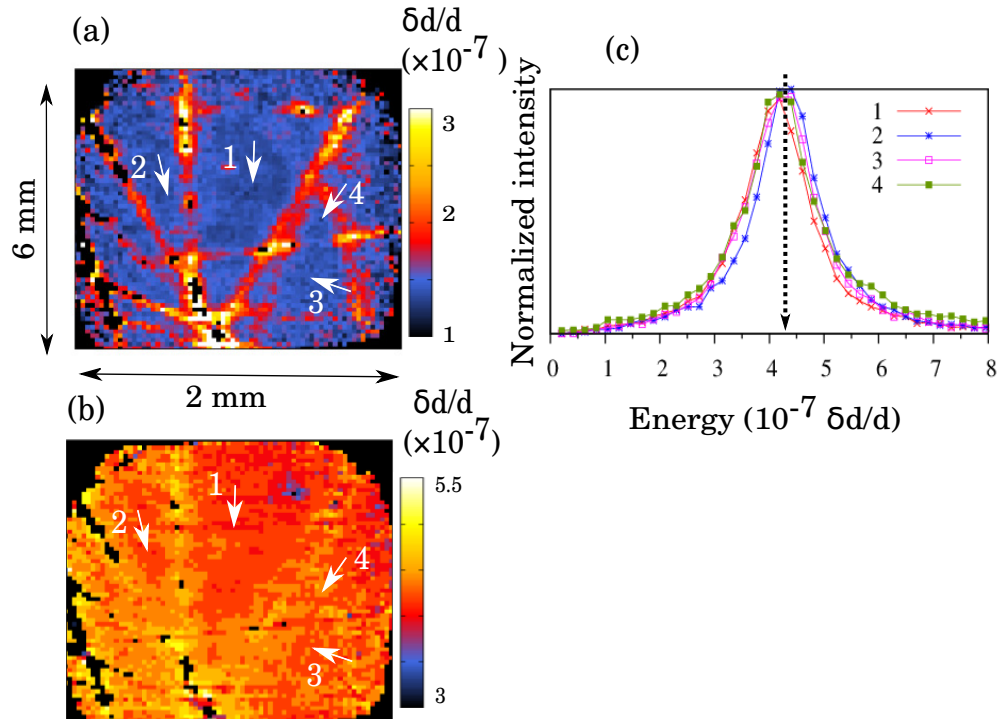
Figure 3.3: : Backscattering rocking curve imaging maps of a Ge crystal. (a) The map of the rocking curve widths in units of $|\delta d/d|=|\delta E/dE|$. (b) The map of the rocking curve centers in units of $\delta d/d$. (c) Rocking curves measured at the pixels labeled in (a) and (b).

Backscattering RCI was applied to characterize sapphire crystals using the reflections (0 1 $\bar{1}$ 50) and (7 10 $\bar{17}$ 18) with intrinsic widths of 1.5, 1.7 meV, and similar extinction lengths, see Table 3.1. Taking into account the 0.7 meV HRM bandwidth, one expects 1.65 meV and 1.83 meV energy width for the reflectivity curves of the ideal crystals. Due to the rather large step of 0.5 meV in the scans of the rocking curves, the precision of the parameters estimation is about 0.2 meV.
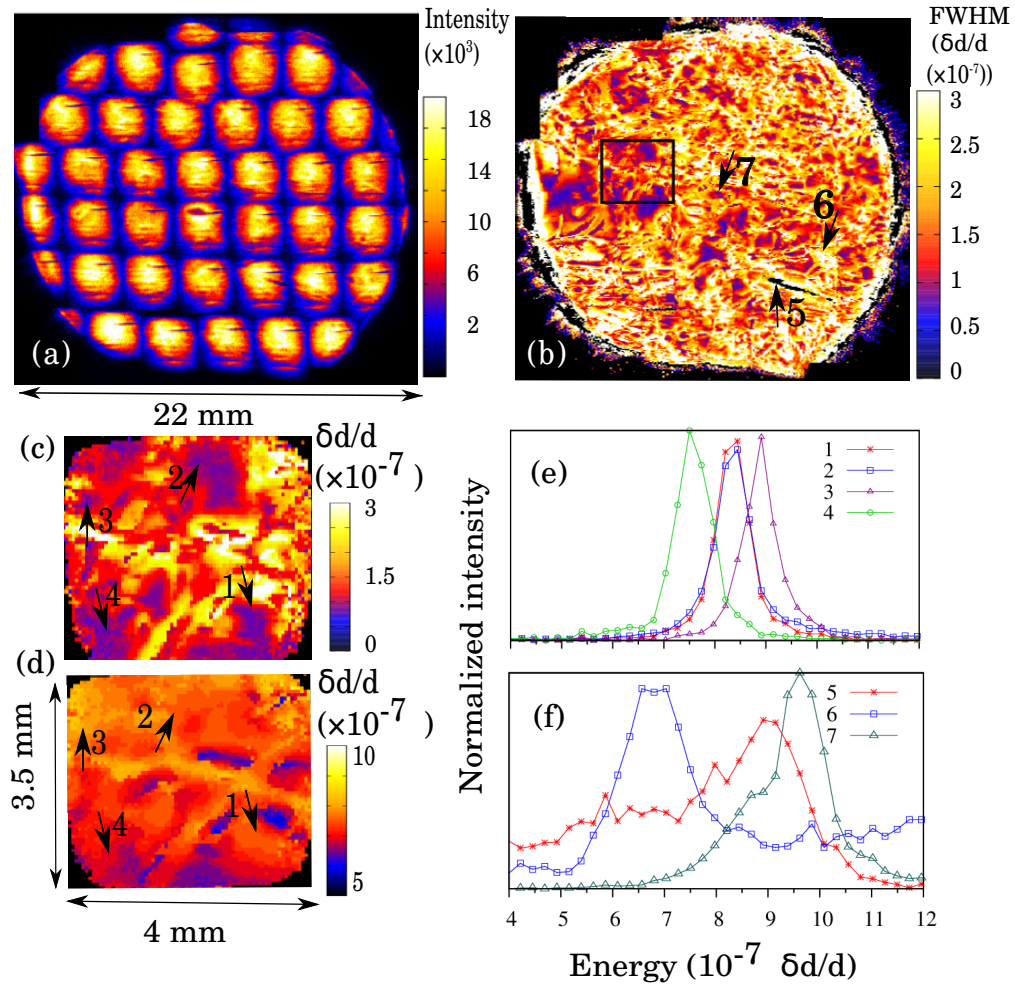
Figure 3.4: The maps of backscattering rocking curve imaging of crystal #1. (a) Total intensity map obtained by integration of the flux over rocking curve. This map represents the beam profile. Different spots correspond to the different positions of the crystal. (b) The map of the rocking curve widths in units of $|\delta d/d|=|\delta E/E|$. (c) A part of this width map in (b) at one crystal position, marked by the black square in (b). (d) The map of the rocking curve centers in units of $\delta d/d$ for the same area as in (c). (e-f) Rocking curves measured at the pixels labeled by numbers in (b) and (c).

The backscattering topography maps of crystal #1 measured with reflection (0 1 $\bar{1}$ 50) at the energy of 23.906 keV are shown in Fig. 3.4. The integrated intensity distribution on the detector is shown in Fig. 3.4a where the modulation by the beam intensity profile is visible for the $\sim$ 40 crystal positions. The rocking curve width map of the entire crystal is shown in Fig. 3.4b. For a chosen spot denoted by the square frame in the full map in Fig. 3.4b, a detailed map of the widths and of the energy distributions at the peak positions are shown in Fig.3.4c and 3.4d, respectively. Note that due to uncontrolled small drifts of the absolute energy of the HRM used in the experiment, we can compare position of the maximum reflectivity curves only within one illuminated spot among

the ~ 40 spots used to raster the crystal, where the energy is tuned simultaneously for all pixels in the detector.

The map of rocking curve widths reveals that the crystal quality varies strongly on a pixel by pixel base. Closer inspection reveals features similar to the white beam topography. It is important to note that black denotes zero-intensity for the map of the rocking curve widths. For example, the big defect in the bottom right part of the topograph in Fig. 3.2c,d. and the space around crystal appears in black in the map in Fig. 3.4b. Regions which only exhibits few dislocations in the middle left part have the best resolution and are shown as dark blue. Examples of the rocking curves measured in the best and worst areas are presented in Fig.3.4e and 3.4f.

The detailed maps of Fig.3.4c and 3.4d shows that there are 4 spots of almost ideal quality with characteristic edge length of 0.2-0.5 mm marked by numbers 1-4 in the figure. The quality of these spots is confirmed by the rocking curves taken at the spots and shown in Fig.3.4e. The characteristic width at these spots is $\delta d/d = 6 \times 10^{-8}$ i.e. an energy bandwidth of 1.43 meV. However, the peak position varies from point to point and a spread over $\delta d/d = 12 \times 10^{-8}$ can be seen between curves 3 and 4. Such variation of the lattice constant between almost ideal spots is two times larger than width of the reflection. The bad quality of the reflections on the border between good spots is partly due to the overlap of the areas with different lattice parameters.

Figure 3.5: Backscattering rocking curve imaging maps of crystal #2. (a) The map of the rocking curve widths. (b) The map of the rocking curve widths taken for one crystal position marked by the black square in (a). (c) Rocking curves measured at the pixels labeled by numbers 1,2,3 in (b). (d) The map of back reflection peak positions of the rocking curves taken for one crystal position marked by the black square in (a).
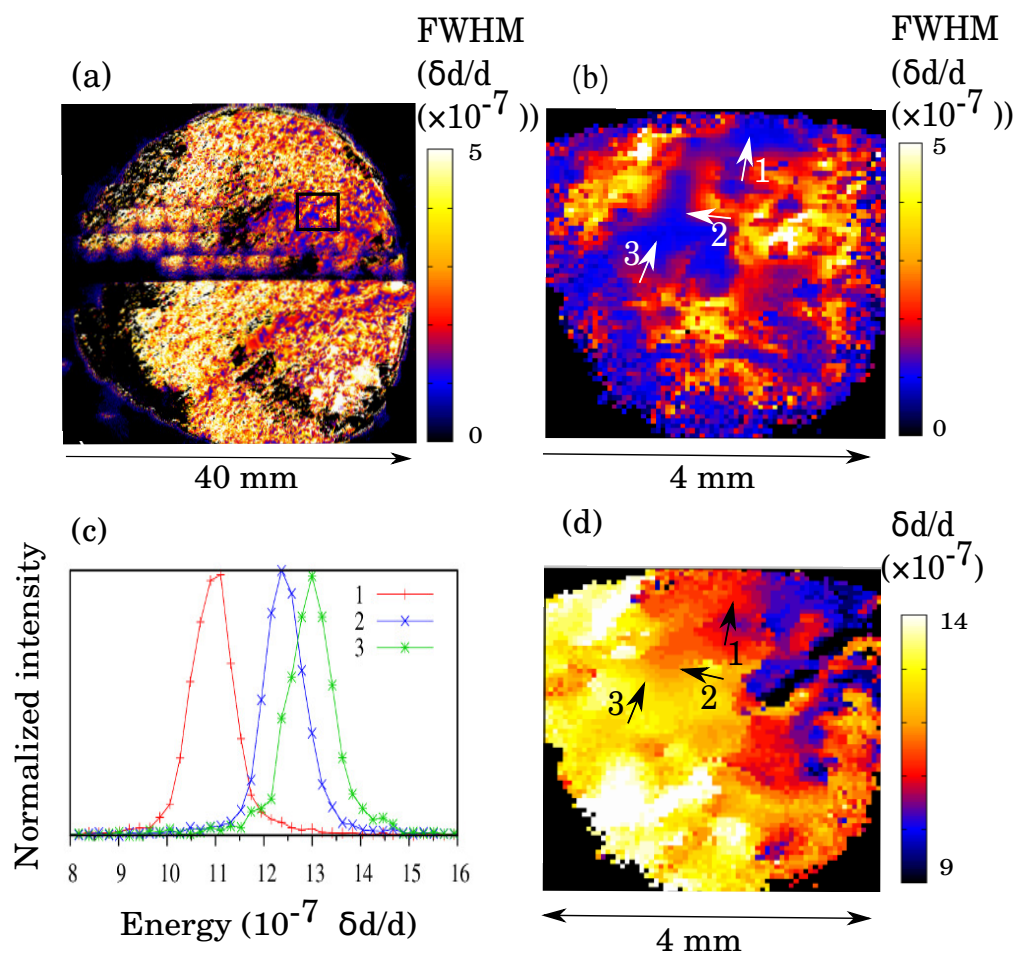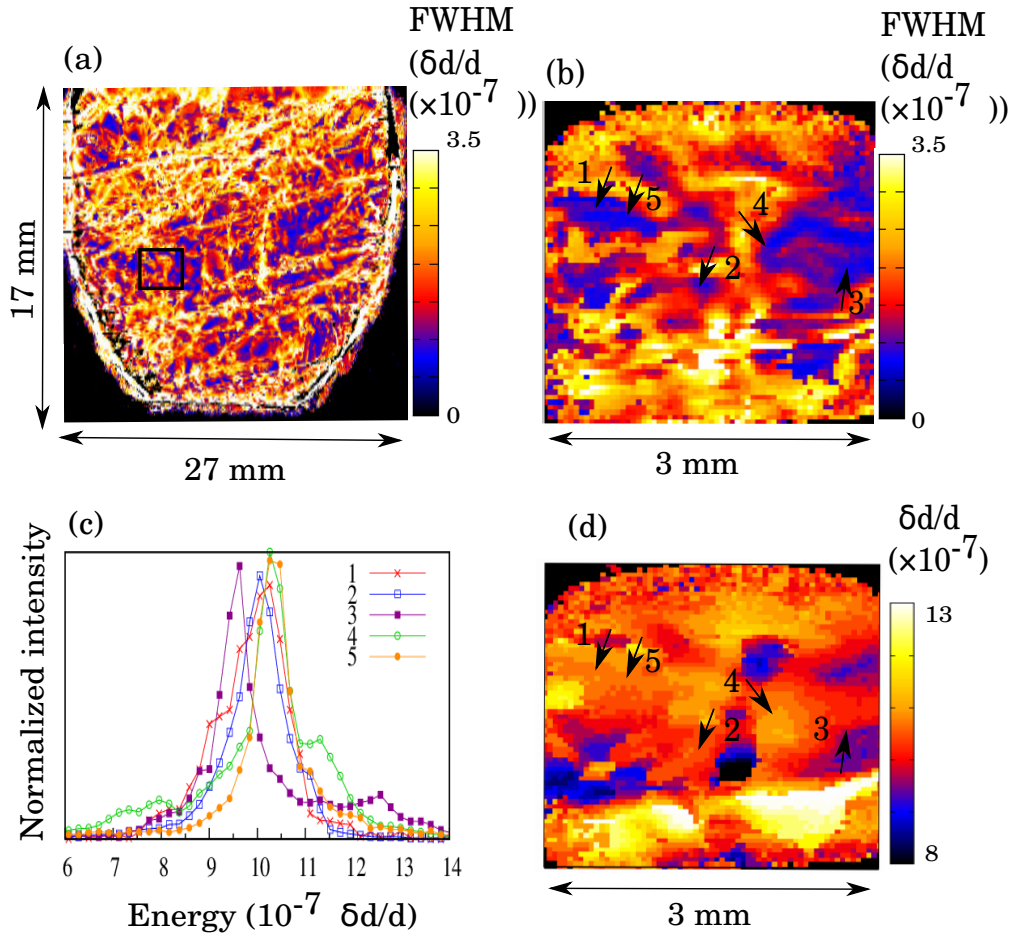
Figure 3.6: Backscattering rocking curve imaging maps of crystal #3. (a) The map of the rocking curve widths. (b) The map of the rocking curve widths in the area marked by the black square in (a). (c) Rocking curves measured at the pixels labeled by numbers 1,2,3,4,5 in (b). (d) The map of back reflection peak positions of the rocking curves taken for the same area as (b).

For crystal #2, the map of rocking curve widths was recorded with the reflection $(7\ 10\ \bar{17}\ 18)$ and is shown in Fig. 3.5a. Only tiny areas exhibit a width $\delta d/d < 10 \times 10^{-8}$. The rest of crystal is highly deformed mainly on the left side. A smaller region denoted by the black rectangle was selected and the corresponding width (Fig. 3.5b) was analyzed. The rocking curves in the center of the good spots are shown in Fig. 3.5c. The good spots have an edge length of 0.3-0.5 mm. These rocking curve are symmetric and without any satellite peaks, similar to the first crystal. An average width of about 8×10^{-8} was obtained, corresponding to 2.0 meV. This value is close to the expected 1.8 meV for an ideal crystal. However, again the peak positions are spread in a range of 50×10^{-8}, 6 times larger than the width of the reflection, see peak position map in Fig.3.5d.

The maps for crystal #3 are shown in Fig.3.6. The reflection $(0\ 1\ \bar{1}\ 50)$, as for crystal #1, was used here. However, this crystal was grown by a different method, see Discussion and Table 3.1. High quality spots with area with an edge length of 0.2-0.5 mm are distributed over almost the entire crystal. They are separated by bad quality interface lines due to the scratches on the surface.

The rocking curves from good areas in one frame are compared in the Fig. 3.6c. Most of these rocking curves have an asymmetric shape with satellite peaks. The average width of these curves is determined to be about $\delta d/d = 9 \times 10^{-8}$ or 2.3 meV which is 50 % larger than theoretically expected for an ideal crystal. A peak position spread is also observed for the selected narrow rocking curves. However, the characteristic spread value $\delta d/d = 3 \times 10^{-8}$ is smaller than in the other crystals of this study. The measurements of crystal #4 and #5 indicate comparatively poor quality of these crystals, see Fig. 3.7.

3.4 Discussion

As seen by RCI in Fig. 3.2, crystal #1 comprises large areas with a rocking curve widths of ≤ 4 arcsec which signifies almost ideal quality with a resolution $\delta d/d \sim 10^{-4}$. Typically, the average widths of the rocking curve of crystals with medium-high quality is a few ten of arcseconds [137, 143]. However with the technology developed in the last decade, width as good as 9.43 arcsec [144] and 8.7 arcsec [145] have been achieved. The last result was achieved with crystals grown by the Rubicon Technology Inc. company, measured with reflection (0 0 0 6) (Bragg angle of 21°) at 8 keV. The latter crystal also shows ideal quality with a resolution $\delta d/d \sim 4 \times 10^{-4}$.

A resolution of $\delta d/d \sim 7 \times 10^{-8}$ is provided by RCI in backscattering geometry where resolution is defined by the width of the rocking curve. In addition, a spatial resolution of 55 μm was obtained over the entire crystal surface. Investigation of the several crystals shows very diverse quality maps in contrast to the quite uniform maps obtained by RCI. Several spots of almost ideal quality and with edge length of 0.2-0.5 mm were found in the maps of all crystals. In principle, such spots can be used for efficient monochromatization of the x-ray beams by using a focused incoming beam. However, most of the crystal areas have worse quality with broadening of the reflectivity curves up to $\delta d/d \sim 3\text{-}5 \times 10^{-7}$. Such quality would lead to an energy bandwidth of the monochromator at 35 keV of about 10-18 meV which is not acceptable for NIS. However, such quality could be reasonable for analyzers used in RIXS, since it would provide an energy bandwidth of 5 meV, for the x-ray energy of 10 keV.

Whereas good spots with symmetric rocking curves exist in all crystals, their quality is slightly different. The highest quality is obtained for the crystals #1 and #2 grown by the Kyropoulos method. The crystal #3 grown by the Bridgman method shows the rocking curve ~ 50 % broader compared to the theoretically expected.

In addition to the width of the rocking curves we also obtained the peak positions over the crystal area. We found that even for good spots the peak positions are different due to variations in the lattice parameters which lead to characteristic variations at $\delta d/d \sim 10\text{-}20 \times 10^{-8}$. In a crystal with dislocations, lattice planes far from the dislocation could be subjected to a homogeneous stress that reduces the d-spacing with respect to a perfect crystal. Conversely, tensile stress would increase the d-spacing. The compressed lattice planes diffract the beam at a lower wavelength or higher energy. We can estimate the relative stress between the dislocation-free regions in crystal #1 along the beam direction, i.e. normal to C plane, because the chosen (0 1 $\bar{1}$ 50) reflection is nearly perpendicular to the surface. The internal stress (σ) in the crystal can be derived from the lattice strain ($\delta d/d$) and elastic tensor c according to $\sigma = c \cdot \delta d/d$. A relative stress of 40(5) kPa is obtained from the

relative shift in the position of peaks 3 and 4 in Fig. 3.4e considering the c_{33} elastic constant from Refs. [146, 147]. According to numerical simulations, due to thermoelastic stress during growth the best part of a Kyropoulos grown boule exhibits absolute value stress similar to 600 kPa [104]. However, most parts of the crystal exhibit values in the range of MPa to GPa [104, 117, 148]. A numerical study on thermoelastic stress distribution for silicon grown by similar technique, the Czochralski method calculates the stress values between a few MPa and 40 MPa [149], much smaller than typical in sapphire. So, not only the average stress in the crystal must be lowered but also their relative change throughout the crystal must be reduceded before sapphire crystal, that can be considered as perfect for x-ray optics can be grown.

The data gathered in this study also suggests that crystals with surface oriented perpendicular to [0 0 0 1] have less x-ray visible lattice defects than those cut perpendicular to [0 1 $\bar{1}$ 2] and [1 0 $\bar{1}$ 2] directions. The Kyropoulos technique is known as an effective method to grow sapphire crystals with high quality, especially in large diameters [91]. Nevertheless, a comparison of crystal #1 and #4 shows that the quality of crystals grown by the same conditions changes dramatically. This is likely due to the inability to control all the known parameters such as the growth rate and temperature gradient or other unidentified parameters.

The impact of discrete dislocations on the lattice parameter variations was investigated by comparison of the white beam topographs and the map of width in crystal #1 as shown in Fig. 3.8. Here blue, red and black contours shows regions with widths of 2, 4, and 6 meV in map of the rocking curve widths plotted on top of the white beam topograph. In general, the higher density of the defects visible in topograph leads to the worse quality of the reflection. At the same time, the best resolutions in the rocking curve widths map not necessarily signigy the absence of defects. The reason for this disagreement is the limited depths of the backscattering reflection. The extinction length of (0 1 $\bar{1}$ 50) reflection is 145 μm at 23.9 keV, which is smaller than 1 mm thickness of the crystal. Thus, defects inside the crystal can not detected by backscattering topography, but are visible in the white beam transmission topograph. In order to check the distribution of defects through the depth of the crystal, backscattering topography on the crystal #1 has been performed from both sides. It was found that the maps the rocking curve widths of the both sides, are in general, similar, so that the density of the defects is uniform through the crystal. However, these results do not exclude the presence of deeper defects in the bulk of crystal to which backscattering topography is not sensitive. These defects would be visible with backscattering topography at higher energy.
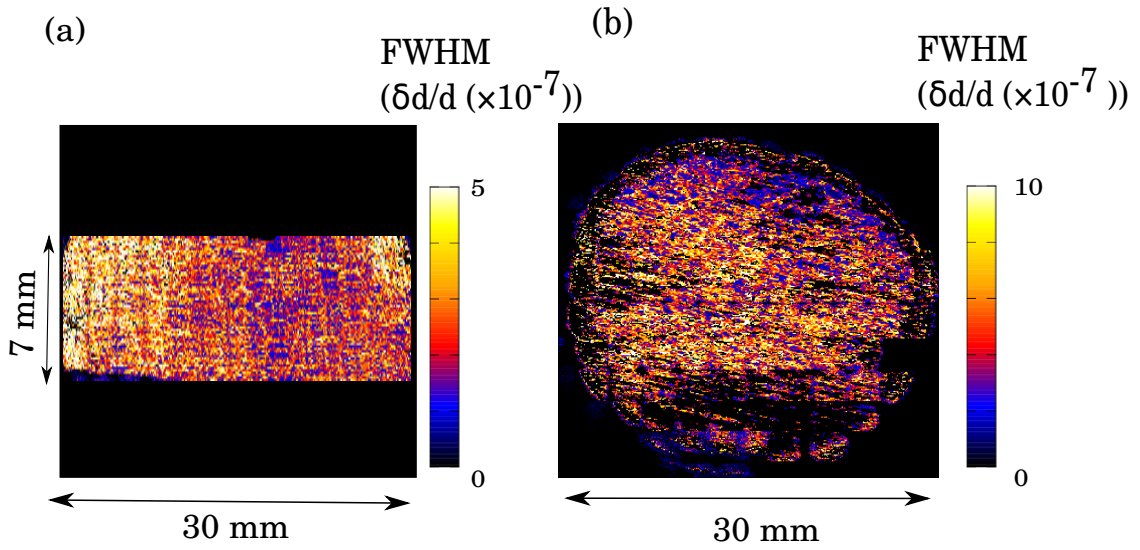
Figure 3.7: The maps of rocking curve widths of (a) part of crystal #4 recorded at reflection (0 1 $\bar{1}$ 50) and (b) crystal #5 recorded at reflection (7 10 $\bar{17}$ 18) using backscattering rocking curve imaging setup.
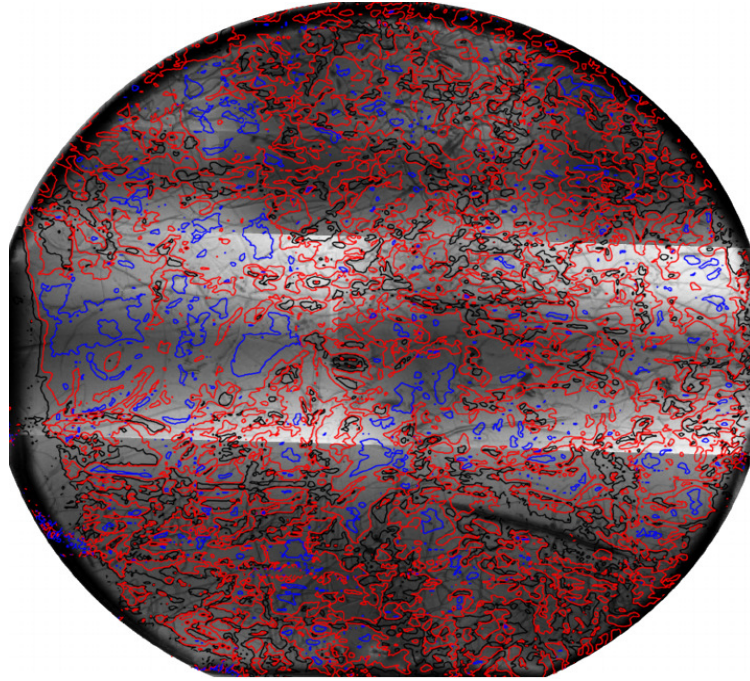
Figure 3.8: Overlay map of the white beam topograph and the map of rocking curve widths for crystal #1 obtained from white beam transmission topography and backscattering rocking curve imaging, respectively. The blue, red, black contours are drawn for widths of 2, 4, and 6 meV in the map of rocking curve widths, respectively.

Next to the material specific insights that we obtained on sapphire crystals, another result is the demonstration of high throughput of rocking curve imaging in backscattering geometry. The measurement duration is short, *e.g.* scanning a 20 mm diameter crystal takes about an hour. This is the technique of choice for determining lattice parameter variations with a high sensitivity of $\delta d/d \approx 10^{-8}$ in nearly perfect single crystals. Note that the sensitivity could be improved by the choice of a narrower bandwidth monochromator, such as discussed in Ref. [150]. The resolution can be further improved using differential intensity measurements at the slope of the rocking curve often used for the topography [139, 151]. Assuming the best relative intensity change of $\delta I/I \sim 0.05$, we estimate that the backscattering topography method with the HRM used herein can provide a $\delta d/d$ resolution down to 10^{-10}.

In this modified topography-like setup, tuning the energy of the incident beam instead of rocking through the Bragg angle of the crystal provides direct access to lattice parameter variation and reveals changes in the peak position of rocking curves with high precision. Another advantage of the used setup is the relatively large beam size obtained by combining a magnifying arrangement of asymmetrically cut crystals together with a large area pixel detector, a combination which provides a solution for utilizing backscattering geometry RCI imaging map in large areas in a reasonable time at a synchrotron radiation facility.

3.5 Conclusion

In this study x-ray characterization of several high quality sapphire single crystals has been performed using three methods: white beam topography, RCI, and backscattering RCI. The RCI results with lattice parameter resolution of $\delta d/d \sim 10^{-4}$ show almost uniform and rather good quality of the crystals, typically sufficient for visible light applications. At the same time, backscattering RCI with resolution $\delta d/d \sim 5 \times 10^{-8}$ reveals mixed quality through all crystals. Almost for crystals nearly ideal regions with edge length of 0.2-0.5 mm were found. However, the lattice parameter even for the ideal spots vary in the range of $\delta d/d = 10$-50×10^{-8} which is few times larger than the width of the reflection. We attribute this variation of the lattice parameters to a relative stress of $\sim$ 40 kPa occurring during crystal growth. Such stress can easily be expected in the current procedure of the sapphire growth. Thus, in order to obtain sapphire crystals of sufficient quality for x-ray high resolution monochromators or analyzers, the procedure of the crystal growth has to be updated in order to decrease the relative thermoelastic stress.

Chapter 4

Lattice Dynamics in AgPb$_m$SbTe$_{2+m}$ (m=0-∞) Thermoelectric Materials

Abstract

The lattice dynamics in Ag$_{0.8}$Sb$_{1.2}$Te$_{2.2}$ and AgPb$_m$SbTe$_{2+m}$ (LAST-*m*) alloys were determined using the element specific Nuclear Inelastic Scattering technique, NIS. LAST-*m* alloys with their high thermoelectric figure of merit (*ZT*) have emerged as promising materials for high-performance thermoelectric power generation in the mid to high temperatures, 500 K and above. The high ZT values for LAST-*m* materials is attributed to the presence of nanoscale precipitation of secondary phases within the matrix, which results in significant reduction of the thermal conductivity. Our study of hyperfine structure of the precipitate revealed local structural distortion of Sb nanostructures in LAST-*m* alloys. We report on the experimental observation of a pronounced group velocity mismatch between the nano inclusion embedded in the matrix when *m* = 18. In earlier work, Barabash *et al*. have suggested this mismatch as origin of the low thermal conductivity in LAST-*m* alloys [38]. There is however an equal excess of low energy phonon modes in the inclusions upon nanostructuration when the *m* value is small, *m* =3, or large, *m* =18.

A Jafari[1,2,3]**, P. Fichtl** [1]**, B. Klobes** [1]**, I. Sergueev**[4]**, and R. P. Hermann**[2,5]

[1]*Jülich Centre for Neutron Science JCNS and Peter Grünberg Institut PGI, JARA-FIT, Forschungszentrum Jülich GmbH, D-52425 Jülich, Germany*

[2] *Faculté des Sciences, Université de Liège - B-4000 Liège, Belgium*

[3]*ESRF- The European Synchrotron, CS40220, 38043 Grenoble Cedex 9, France*

[4] *Deutsches Elektronen-Synchrotron - D-22607 Hamburg, Germany*

[5]*Materials Science and Technology Division, Oak Ridge National Laboratory, Oak Ridge, Tennessee 37831, USA*

Chapter 5

Lattice Dynamics Study of Antimony and Tellurium Oxides

Abstract

We present a study of the structure and lattice dynamics of α-Sb$_2$O$_3$ (senarmontite), β-Sb$_2$O$_3$, and α-TeO$_2$ (paratellurite), compounds with pronounced stereochemically active Sb and Te lone pairs. Mössbauer spectroscopy is used to study the structure of Sb in α-Sb$_2$O$_3$ and β-Sb$_2$O$_3$. Vibrational spectroscopy of Sb and Te for each oxide are investigated using Nuclear Inelastic Scattering, NIS. In order to further obtain information on O vibrational modes, inelastic neutron scattering was utilized. Furthermore, the vibrational frequencies obtained by density functional theory (DFT) to make a comparison with the experimental results and to assess the validity of the utilized functional. Good agreement was found between density functional theory calculated and experimental density of phonon states. The Sb-O-Sb wagging mode of α-Sb$_2$O$_3$ is experimentally observed at $\sim$ 336 cm^{-1} for the first time, its frequency was not clear in most of previous studies. A softer lattice vibrational modes occur in orthohombic β-Sb$_2$O$_3$ as compared to cubic α-Sb$_2$O$_3$, indicating that the antimony bonds are weakened upon transforming from molecular α-Sb$_2$O$_3$ to layer chained structure β-Sb$_2$O$_3$. The comparison of experimental and theoretical approach provides a detailed picture of the lattice dynamics in these oxides.

A Jafari[1,2,3]**, B. Klobes** [1]**, V. L. Deringer** [4]**, R. P. Stoffel**[4]**, R. Dronskowski** [4]**, I. Sergueev**[5]**, and R. P. Hermann**[2,6]

[1]*Jülich Centre for Neutron Science JCNS and Peter Grünberg Institut PGI, JARA-FIT, Forschungszentrum Jülich GmbH, 52425 Jülich, Germany*

[2] *Faculté des Sciences, Université de Liège 4000 Liège, Belgium*

[3]*ESRF- The European Synchrotron, 38043 Grenoble Cedex 9, France*

[4]*Institute of Inorganic Chemistry, RWTH Aachen University Landoltweg 1, Aachen, 52074, Germany*

[5]*Materials Science and Technology Division, Oak Ridge National Laboratory, Oak Ridge, Tennessee 37831, USA*

Chapter 6

6

Summary and outlook

In this study, we examined the crystal quality of sapphire by using various synchrotron based techniques. We discussed the different types of observed lattice defects, their distribution, and Burgers vector in several crystals using white beam topography at the TOPO-TOMO beamline in ANKA, KIT, and BM05 at ESRF. Our findings demonstrate that the quality of sapphire depends crucially on its growth technique, its post treatments and the cutting direction. The Kyropoulos technique is the most promising technique to produce high quality sapphire in large volume. The Bridgman, horizontal directional solidification, and Verneuil methods give in average lower quality, sequentially. The *C*-plane Kyropoulos grown crystals revealed the best quality, even better than the highest commercially available quality.

Up to now no large volume perfect sapphire single crystal were fabricated. In this work, a particular attention is paid to the characterization to make the available crystals applicable for the x-ray techniques *e.g.* NRS and RIXS.

The study on the broadening of rocking curves using a monochromatic beam provided quantitative information about the impact of lattice defects on disruptions in the parallelism of atomic planes and lattice parameter variations. The widths of rocking curves from a nearly perfect region in some crystals showed a very close value to an intrinsic width for that reflection. The least lattice parameter variability was observed in defect free areas of crystal #1. Detail comparison of the white beam topograph and maps of rocking curve width for this crystal showed the presence of dislocations which have less impact on lattice parameter changes or energy resolution in backscattering reflections. We noticed that defect-free areas do not necessarily give the best energy resolution.

Currently, one of the best sapphires is used as monochromator in the nuclear resonance station, ID18, ESRF. Using the NIS setup enabled us to observe lattice dynamics of solids composed of Sb and/or Te Mössbauer isotopes, with small x-ray bandwidth. We were interested in investigating the lattice related properties of a very promising thermoelectric material, $(PbTe)_m AgSbTe_2$, called LAST-*m* alloy. Its high figure of merit is partly due to the low thermal conductivity, attributed to the precipitation of (Ag, Sb) nanostructures within the PbTe matrix. Phonon scattering processes occur at the boundary of the matrix (the main phase) and nanoprecipitates (the secondary phases). We obtained the ^{125}Te and ^{121}Sb partial phonon density of states of LAST-*m* alloys, using NIS experiments at the nuclear transition energies of ^{121}Sb (37.129 keV) and ^{125}Te (35.409 keV) with energy resolution of 0.7 meV corresponding to both energies. These results are helpful to explore the vibrational properties and lattice dynamics of the main and secondary phases, individually. In-depth knowledge was gained by comparing the phonon density of states of LAST-*m* to PbTe and $Ag_{0.8}Sb_{1.2}Te_2$.

The important result is that we observed a phonon group velocity mismatch between the matrix and the nanoprecipitates. This mismatch is most pronounced in LAST-18. It has been suggested that phonons created or annihilated at the boundary travels in nanoprecipitates with frequencies different than those in the matrix, and as a result the transmission of heat carrying phonons, mainly acoustic phonons, is reduced and thereby the lattice thermal conductivity is minimized.

Furthermore, we investigated the vibrational properties and lattice dynamics of phase pure α-Sb_2O_3, β-Sb_2O_3, and α-TeO_2 containing Sb(III) and Te(IV) lone pair elements. The presence of the stereochemical active lone pair electrons in these oxides is responsible for the formation of highly distorted structures. α-Sb_2O_3 has extensive industrial application and is used as a catalyst and as a flame retardant in textiles and other materials. Glasses based on β-Sb_2O_3 and α-TeO_2, are of great interest due to their non-centrosymmetric crystal structures. Understanding their lattice vibrations and corresponding properties is a step for further application and improved functionality.

The measured partial DPS in these oxides was found comparable to calculated partial DPS for each oxide and the band frequencies were in good agreement with the earlier studies. The results are important for benchmarking DFT lattice dynamics calculation involving lone pair electrons. The total DPS obtained by inelastic neutron scattering measurement and the vibrational frequencies are consistent with DFT calculated total DPS. The DPS revealed most of the Raman and IR active and inactive modes. As Raman and IR spectroscopy data are incomplete, our results are useful to assign the modes with so far unclear assignments and frequencies.

In β-Sb_2O_3, the vibrational modes are located mainly in the low energy range indicating a smaller force constant as compared to α-Sb_2O_3. Comparison of Sb-O bond strength between the two common phases of Sb_2O_3 showed a higher mean force constant in α-Sb_2O_3, with molecular structure. Te-O bonds in the quasi molecular structure α-TeO_2 are also robust.

NFS and conventional ^{121}Sb Mössbauer spectroscopy revealed a pronounced quadrupole splitting for both α-Sb_2O_3 and β-Sb_2O_3 associated with the presence of the lone pair electrons. The nuclear quadrupole interaction in β-Sb_2O_3 has a large asymmetry parameter. The determination of the quadrupole splitting was improved using time domain NFS spectra.

Clearly, further research will be needed to improve the sapphire quality. Future work will involve growing more C-plane sapphire single crystals using Kyropoulos technique with a reduced growth (pulling) rate of $<< 0.5$ mm/h. In addition, very careful control of any other growth parameters, special care to the purity of the feed material, and very clean high vacuum are required. Also, it is worth trying other promising growth techniques such as Chemical Vapor Deposition (CVD). Investigation on any other non-cubic single crystal with high atomic number, high Debye temperature, and Debye-Waller factor and reaching an ideal crystal quality is of great interest for x-ray optics.

Further study on vibrational properties and lattice dynamics on several $Ag_{1-x}Pb_{18}Sb_{1+x}Te_{20}$, *i.e.* alloys with close stoichiometry close to LAST-18, with the reported information on microstructural and thermoelectrical properties of these alloys will give insight into the formation of the matrix with similar feature to PbTe and to help to find the exact stoichiometry which gives the best thermoelectric properties. The correlation between the size of nanostructured precipitates, could be varied by annealing, and their acoustic phonon behavior, and finally their thermoelectric performance improved. The process of nanostructuration of Sb in a Te rich sample in any LAST-m alloy can be investigated by in situ x-ray diffraction and any change of their hyperfine interactions can

be monitored in nuclear forward scattering of synchrotron radiation which would yield in-depth knowledge.

Chapter 7

Curriculum Vitae

Atefeh Jafari was born on September 18, 1986 in Tehran, Iran. She received her bachelor's degree in Physics-Solid states from Tarbiat Moallem University of Tehran (Kharazmi) in June 2009. She then moved to the Kuala Lumpur, Malaysia to attend graduate school at the University Putra Malaysia (UPM) where she earned Master degree on Nanomaterial and Nanotechnology on September 2012 for her thesis entitled "Synthesis and characterization of chemical deposited nanostructured Cadmium Sulphide thin film for solar cell applications". She worked as research assistant in the department of Physics, faculty of science at UPM from April 2011 to July 2012. She continued her doctoral research at the Forschungszentrum Jülich and the University of Liège under the supervision of Prof. Dr. Raphaël Hermann. She was a long-term visitor thesis student at the group of "Matters at extremes" at the European Synchrotron Radiation Facility (ESRF) under supervision of Dr. Alexandr Chumakov.

List of Publications

Jafari, A., Rizwan Z., Ghazali M.,Din F., Zakaria A. (2010). Optical and structural characterization of air-annealed CdS film prepared by chemical bath deposition (CBD) technique, *Chalcogenide Letters*, 12(7), 641.

Jafari, A., Zakaria A., Rizwan Z., Ghazali M. (2011). Effect of Low Concentration Sn Doping on Optical Properties of CdS Films Grown by CBD Technique, *International Journal of Molecular Sciences*, 12(9), 6320.

Rizwan Z., Zakaria A., Ghazali M., Jafari A., Din F., Zamiri R. (2011). Effect of Annealing Temperature on the Optical Spectra of CdS Thin Films Deposited at Low Solution Concentrations by Chemical Bath Deposition (CBD) Technique, *International Journal of Molecular Sciences*,12(2), 1293.

Daud M.N.M., Zakaria A., Jafari A., Ghazali M., Abdullah W.R.W., Zainal Z.(2012). Characterization of CdTe Films Deposited at Various Bath Temperatures and Concentrations Using Electrophoretic Deposition, *International Journal of Molecular Sciences*, 13, 5706.

Jafari A. and Zakaria A. (2012). Fabrication and modification of chemical deposited nanocrystalline cadmium sulphide thin film in presence of impurity, *AIP Conference Proceedings*, 1482(1), 617.

Bessas D., Sergueev I., Merkel D. G., Chumakov A.I., Rüffer R. , Jafari A. , Kishimoto S., Wolny J.A., Schünemann V., Needham R.J., Sadler P.J., Hermann R.P. (2015). Nuclear resonant scattering of synchrotron radiation by ^{187}Os. *Phys. Rev. B*, 91, 224102.

Alexeev P., Asadchikov V., Bessas D., Butashin A., Deryabin A., Dill F.-U, Ehnes A., Herlitschke M., Hermann R.P., Jafari A., Prokhorov I.A., Roshchin B., Rohlsberger R., Schlage K., Sergueev I., Siemens A., Wille H.-C. (2016). The sapphire backscattering monochromator at the Dynamics beamline P01 of PETRA III, *Hyperfine Interactions*, 237, 59.

Klobes B., Arinicheva Y., Neumeier S., Simon R.E., Jafari A., Bosbach D., Hermann R.P. (2016). Quadrupole splitting and Eu partial lattice dynamics in europium orthophosphate $EuPO_4$. Hyperfine Interactions, 237, 31.

Asadchikov V.E, Butashin A.V., Buzmakov A.V., Deryabin A. N., Kanevsky V.M., Prokhorov I. A., Roshchin B.S., Volkov Y.O., Zolotov D.A., Jafari A., Alexeev P., Cecilia A., Baumbach T., Bessas D., Danilewsky A. N., Sergueev I., Wille H.-C., Hermann R.P. (2016). Single crystal sapphire microstructure for high resolution synchrotron X-ray monochromators, *Crystal Research and Technology*, 51(4), 290.

Jafari A., Sergueev I., Bessas B., Klobes B., Roschin B., Asadchikov V., Alexeev P., Härtwig J., Chumakov A. I., Wille H.-C., and Hermann R.P., "Rocking Curve Imaging of High Quality Sapphire Crystals in Backscattering Geometry", Submitted to Journal of Applied Physics.

Contributed Presentation in Conferences and Seminars

University Malaysia Terengganu 10th International Annual Symposium (UMTAS), Oral presentation, 11-13 July 2011, Terengganu, Malaysia.

DPG (German Physical Society) conference, Oral presentation, 30 March-4 April 2014, Dresden, Germany.

Meeting of contact group for synchrotron radiation, Oral presentation, 8-9 Dec 2014, Namur, Belgium.

DPG conference, Oral presentation, 15-20 March 2015, Berlin, Germany.

Congress of the Francophone group Mössbauer spectrometry (GFSM), Poster presentation, 21-22 May 2015, Jülich, Germany.

International Conference on Thermoelectrics and European Conference on Thermoelectrics ICT and ECT 2015, Oral presentation, 28 June-2 July, Dresden, Germany.

International Conference on the Applications of the Mössbauer Effect (ICAME), Oral and Poster presentations. 13th to 18th September 2015, Hamburg, Germany.

Awards

Gold Medal in "Invention, Research, and Innovation Exhibition", in "Applied Research", in cluster of "Science, Technology, and Engineering", University Putra Malaysia, Malaysia, 18-21 July, 2011.

Silver Medal in "Invention, Research, and Innovation Exhibition", in "Applied Research", in cluster of "Science, Technology, and Engineering", University Putra Malaysia, Malaysia, July 2012.

Bibliography

[1] E. Gerdau and H. de Waard, *Nuclear Resonant Scattering of Synchrotron Radiation(Part A)*, Hyperfine Interactions, 1999, vol. 123-124.

[2] E. Gerdau and H. de Waard, *Nuclear Resonant Scattering of Synchrotron Radiation(Part B)*, Hyperfine Interactions, 2000, vol. 125.

[3] R. Röhlsberger, *Nuclear Condensed Matter Physics with Synchrotron Radiation: Basic Principles, Methodology and Applications*, Springer Berlin Heidelberg, 2010, vol. 208.

[4] E. Gerdau, R. Rüffer, H. Winkler, W. Tolksdorf, C. P. Klages and J. P. Hannon, *Phys. Rev. Lett.*, 1985, **54**, 835–838.

[5] P. Elleaume, *Nuclear Instruments and Methods in Physics Research Section A: Accelerators, Spectrometers, Detectors and Associated Equipment*, 1989, **282**, 477 – 480.

[6] C.-I. Brändén, *Structure*, 1994, **2**, 5–6.

[7] A. K. Freund, *Proc. SPIE*, 1995, **2515**, 445–457.

[8] M. Seto, Y. Yoda, S. Kikuta, X. W. Zhang and M. Ando, *Phys. Rev. Lett.*, 1995, **74**, 3828–3831.

[9] W. Sturhahn, T. S. Toellner, E. E. Alp, X. Zhang, M. Ando, Y. Yoda, S. Kikuta, M. Seto, C. W. Kimball and B. Dabrowski, *Phys. Rev. Lett.*, 1995, **74**, 3832–3835.

[10] T. Toellner, *Hyperfine Interactions*, 2000, **125**, 3–28.

[11] A. Authier, S. Lagomarsino and B. K. Tanner, *X-Ray and Neutron Dynamical Diffraction: Theory and Applications*, Springer US, Boston, MA, 1996.

[12] F. Masiello, G. Cembali, A. I. Chumakov, S. H. Connell, C. Ferrero, J. Härtwig, I. Sergeev and P. Van Vaerenbergh, *Journal of Applied Crystallography*, 2014, **47**, 1304–1314.

[13] J. Als-Nielsen and D. McMorrow, *Diffraction by perfect crystals*, John Wiley and Sons, Inc., 2011.

[14] E. Gerdau, *Hyperfine Interactions*, 1994, **90**, 301–312.

[15] E. Burkel, *Reports on Progress in Physics*, 2000, **63**, 171.

[16] B. Dorner, E. Burkel and J. Peisl, *Nuclear Instruments and Methods in Physics Research Section A: Accelerators, Spectrometers, Detectors and Associated Equipment*, 1986, **246**, 450–451.

[17] Y. Shvyd'ko, *X-Ray Optics-High-Energy-Resolution Applications*, Springer, Berlin, 2009, vol. 98.

[18] A. Q. R. Baron, S. Kishimoto, J. Morse and J.-M. Rigal, *Journal of Synchrotron Radiation*, 2006, **13**, 131–142.

[19] T. Gog, D. M. Casa, A. H. Said, M. H. Upton, J. Kim, I. Kuzmenko, X. Huang and R. Khachatryan, *Journal of Synchrotron Radiation*, 2013, **20**, 74–79.

[20] I. Sergueev, H.-C. Wille, R. P. Hermann, D. Bessas, Y. V. Shvyd'ko, M. Zajac and R. Rüffer, *Journal of Synchrotron Radiation*, 2011, **18**, 802–810.

[21] R. Rüffer and A. I. Chumakov, *Hyperfine Interactions*, 1996, **97**, 589–604.

[22] E. Fremy, *Synthese Du Rubis*, Hachette Livre - Bnf, 2015.

[23] D. C. Harris, *Proceedings of the American Academy of Arts and Sciences*, 1925, **60**, 305–383.

[24] D. C. Stockbarger, *Review of Scientific Instruments*, 1936, **7**, 133–136.

[25] B. Chalmers, *Canadian Journal of Physics*, 1953, **31**, 132–146.

[26] A. Chernov, E. Givargizov, K. Bagdasarov, V. Kuznetsov, L. Demianets and A. Lobachev, *Modern Crystallography III: Crystal Growth*, Springer Berlin Heidelberg, 1984.

[27] C. S. Bagdasarov, *Sovremennaja kristallografija*, 1980, **3**, 350.

[28] S. Kyropoulos, *Zeitschrift für anorganische und allgemeine Chemie*, 1926, **154**, 308–313.

[29] D. C. Harris, *Proc. SPIE*, 2003, **5078**, 1–11.

[30] D. C. Harris, *Proc. SPIE*, 2009, **7425**, 74250P–74250P–12.

[31] F. Barvinschi, J.-L. Santailler, T. Duffar and H. L. Gal, *Journal of Crystal Growth*, 1999, **198-199, Part 1**, 239–245.

[32] C. Miyagawa, T. Kobayashi, T. Taishi and K. Hoshikawa, *Journal of Crystal Growth*, 2014, **402**, 83–89.

[33] G. A. Lebedev, S. P. Malyukov, V. A. Stefanovich and D. I. Cherednichenko, *Crystallography Reports*, 2008, **53**, 331–335.

[34] S. Demina, E. Bystrova, M. Lukanina, V. Mamedov, V. Yuferev, E. Eskov, M. Nikolenko, V. Postolov and V. Kalaev, *Optical Materials*, 2007, **30**, 62 – 65.

[35] V. A. Tatartchenko, *Sapphire Crystal Growth and Applications*, John Wiley and Sons, Ltd, 2010.

[36] M. S. Akselrod and F. J. Bruni, *Journal of Crystal Growth*, 2012, **360**, 134 – 145.

[37] H. S. Dow, M. W. Oh, S. D. Park, B. S. Kim, B. K. Min, H. W. Lee and D. M. Wee, *Journal of Applied Physics*, 2009, **105**,.

[38] S. V. Barabash, V. Ozolins and C. Wolverton, *Phys. Rev. Lett.*, 2008, **101**, 155704.

[39] M. E. Manley, S. Shapiro, Q. Li, A. Llobet and M. E. Hagen, *Journal of Applied Physics*, 2011, **109**, 083722–1 – 4.

[40] P. Bauer Pereira, *PhD thesis*, Université de Liège, Faculté des Sciences, Liège,Belgium, 2011.

[41] W. Berg, *Naturewissenschaften*, 1931, **19**, 391–396.

[42] C. Barrett, *Trans. IMD-AIME*, 1945, **161**, 15–64.

[43] M. Hart, *Journal of Applied Crystallography*, 1975, **8**, 436–444.

[44] B. Tanner, *Progress in Crystal Growth and Characterization*, 1977, **1**, 23 – 56.

[45] W. Zachariasen, *Theory of X-ray diffraction in crystals*, J. Wiley & Sons, inc., 1945.

[46] A. Authier, *physica status solidi (b)*, 1968, **27**, 77–93.

[47] D. Bowen and B. Tanner, *High Resolution X-Ray Diffractometry And Topography*, CRC Press, 2005.

[48] U. Bonse, *Zeitschrift für Physik*, 1958, **153**, 278–296.

[49] F. Masiello, *PhD thesis*, Université de Grenoble, Grenoble, France, 2011.

[50] J. Härtwig, S. Köhler, W. Ludwig, H. Moriceau, M. Ohler and E. Prieur, *Crystal Research and Technology*, 2002, **37**, 705–715.

[51] D. Lübbert, T. Baumbach, J. Härtwig, E. Boller and E. Pernot, *Nuclear Instruments and Methods in Physics Research Section B: Beam Interactions with Materials and Atoms*, 2000, **160**, 521–527.

[52] N. Chrysanthakopoulos, M. Calamiotou, F. Lorut and J. Baruchel, *Journal of Physics D: Applied Physics*, 2001, **34**, A163.

[53] D. Lübbert and T. Baumbach, *Journal of Applied Crystallography*, 2007, **40**, 595–597.

[54] T. A. Lafford, J. Villanova, N. Plassat, S. Dubois and D. Camel, *Journal of Physics: Conference Series*, 2013, **425**, 192019.

[55] Wierzbicka, D. A., J.Z., Zytkiewicz and L. Z.R., *Synchrotron Radiation in Natural Science*, 2009, **8**, 26–27.

[56] Y. V. Shvyd'ko, E. Gerdau, J. Jäschke, O. Leupold, M. Lucht and H. D. Rüter, *Phys. Rev. B*, 1998, **57**, 4968–4971.

[57] J. P. Sutter, A. Q. R. Baron, D. Miwa, Y. Nishino, K. Tamasaku and T. Ishikawa, *Journal of Synchrotron Radiation*, 2006, **13**, 278–280.

[58] Y. Shvyd'ko, *Nature Physics*, 2010, **6**, 196–199.

[59] R. L. Mössbauer, *Zeitschrift für Physik*, 1958, **151**, 124–143.

[60] K. Koch, K. Koepernik, D. V. Neck, H. Rosner and S. Cottenier, *Phys. Rev. A*, 2010, **81**, 032507.

[61] P. Gütlich, E. Bill and A. Trautwein, *Mössbauer Spectroscopy and Transition Metal Chemistry: Fundamentals and Applications*, Springer Berlin Heidelberg, 2010.

[62] H.-C. Wille, Y. V. Shvyd'ko, E. E. Alp, H. D. Rüter, O. Leupold, I. Sergueev, R. Rüffer, A. Barla and J. P. Sanchez, *EPL (Europhysics Letters)*, 2006, **74**, 170.

[63] A. Chumakov and W. Sturhahn, *Hyperfine Interactions*, 1999, **123**, 781–808.

[64] V. G. Kohn, A. I. Chumakov and R. Rüffer, *Phys. Rev. B*, 1998, **58**, 8437–8444.

[65] A. Rüffer, R.and Chumakov, *Hyperfine Interactions*, 2000, **128**, 255–272.

[66] D. Bessas, I. Sergueev, D. G. Merkel, A. I. Chumakov, R. Rüffer, A. Jafari, S. Kishimoto, J. A. Wolny, V. Schünemann, R. J. Needham, P. J. Sadler and R. P. Hermann, *Phys. Rev. B*, 2015, **91**, 224102.

[67] W. Sturhahn, *Hyperfine Interactions*, 2000, **125**, 149–172.

[68] U. van Bürck, D. P. Siddons, J. B. Hastings, U. Bergmann and R. Hollatz, *Phys. Rev. B*, 1992, **46**, 6207–6211.

[69] V. A. Bordovitsyn and I. Ternov, *Synchrotron Radiation Theory and Its Development: In Memory of I.M. Ternov*, World Scientific, 1999.

[70] L. Zhang, J. Stanek, S. S. Hafner, H. Ahsbahs, H. F. Gruensteudel, J. Metge and R. Rüffer, *American Mineralogist*, 1999, **84**, 447–453.

[71] C. Strohm, P. Van der Linden and R. Rüffer, *Phys. Rev. Lett.*, 2010, **104**, 087601.

[72] J. B. Hastings, D. P. Siddons, U. van Bürck, R. Hollatz and U. Bergmann, *Phys. Rev. Lett.*, 1991, **66**, 770–773.

[73] O. Leupold, A. Chumakov, E. Alp, W. Sturhahn and A. Baron, *Hyperfine Interactions*, 1999, **123**, 611–631.

[74] I. Sergueev, A. I. Chumakov, T. H. D. Beaume-Dang, R. Rüffer, C. Strohm and U. van Bürck, *Phys. Rev. Lett.*, 2007, **99**, 097601.

[75] D. Bessas, D. G. Merkel, A. I. Chumakov, R. Rüffer, R. P. Hermann, I. Sergueev, A. Mahmoud, B. Klobes, M. A. McGuire, M. T. Sougrati and L. Stievano, *Phys. Rev. Lett.*, 2014, **113**, 147601.

[76] T. Lummen, *PhD thesis*, University of Groningen, Groningen, The Netherlands, 2009.

[77] B. Klobes, N. Barrier, B. Vertruyen, C. Martin and R. P. Hermann, *Hyperfine Interactions*, 2014, **226**, 713–719.

[78] C. A. Cody, L. DiCarlo and R. K. Darlington, *Inorganic Chemistry*, 1979, **18**, 1572–1576.

[79] D. Zeng, C. Xie, B. Zhu and W. Song, *Materials Letters*, 2004, **58**, 312–315.

[80] S. Hu, M. Johnsson, P. Lemmens, D. Schmid, D. Menzel, J. Tapp and A. Müller, *Chemistry of Materials*, 2014, **26**, 3631–3636.

[81] D. Zhang, R. K. Kremer, P. Lemmens, K.-Y. Choi, J. Liu, M.-H. Whangbo, H. Berger, Y. Skourski and M. Johnsson, *Inorganic Chemistry*, 2011, **50**, 12877–12885.

[82] D. J. Stewart, O. Knop, C. Ayasse and F. W. D. Woodhams, *Canadian Journal of Chemistry*, 1972, **50**, 690–700.

[83] G. G. Long, J. G. Stevens and L. H. Bowen, *Inorganic and Nuclear Chemistry Letters*, 1969, **5**, 799 – 804.

[84] W. Peng, R. Hannon, H. Lee, A. Genis, V. Melim, C. Kimball, B. Dabrowski and D. Hinks, *Physics Letters A*, 1989, **139**, 91–94.

[85] A. Svane, *Phys. Rev. B*, 2003, **68**, 064422.

[86] K. K. Tedjojuwono, N. Clark and W. M. Humphreys, *Proc. SPIE*, 2013, **8884**, 88841I–88841I–11.

[87] G. Cullen, V. Ban, C. Wang, S. Berkman, J. Blanc, M. Duffy, N. Goldsmith, W. Ham and P. Zanzucchi, *Heteroepitaxial Semiconductors for Electronic Devices*, Springer New York, 2013.

[88] L. Romano, V. Privitera and C. Jagadish, *Defects in Semiconductors*, Elsevier Science, 2015.

[89] M. Abrahams and J. Blanc, *Method of improving silicon crystal perfection in silicon on sapphire devices*, 1981, US Patent 4,279,688.

[90] D. Look, *Physica Status Solidi (b)*, 2001, **228**, 293–302.

[91] H. Tang, H. Li and J. Xu, *Growth and Development of Sapphire Crystal for LED Applications*, INTECH Open Access Publisher, 2013.

[92] H. Yavaş, E. E. Alp, H. Sinn, A. Alatas, A. H. Said, Y. Shvyd'ko, T. Toellner, R. Khachatryan, S. J. Billinge, M. Z. Hasan and W. Sturhahn, *Nuclear Instruments and Methods in Physics Research Section A: Accelerators, Spectrometers, Detectors and Associated Equipment*, 2007, **582**, 149 – 151.

[93] M. G. Hönnicke, X. Huang, C. Cusatis, C. N. Koditwuakku and Y. Q. Cai, *Journal of Applied Crystallography*, 2013, **46**, 939–944.

[94] Y. Imai, Y. Yoda, S. Kitao, R. Masuda, S. Higashitaniguchi, C. Inaba and M. Seto, *Proc. SPIE*, 2007, **6705**, 670512.

[95] K. Hoshikawa, J. Osada, Y. Saitou, E. Ohba, C. Miyagawa, T. Kobayashi, J. Yanagisawa, M. Shinozuka and K. Kanno, *Journal of Crystal Growth*, 2014, **395**, 80 – 89.

[96] B. Raghothamachar, G. Dhanaraj, J. Bai and M. Dudley, *Microscopy Research and Technique*, 2006, **69**, 343–358.

[97] E. R. Dobrovinskaya, L. A. Lytvynov and V. Pishchik, *Sapphire Material, Manufacturing, Applications*, Springer, Berlin, 2009.

[98] B. Tanner, *X-ray Diffraction Topography*, Elsevier Science & Technology, 1976.

[99] A. Rack, T. Weitkamp, S. B. Trabelsi, P. Modregger, A. Cecilia, T. dos Santos Rolo, T. Rack, D. Haas, R. Simon, R. Heldele, M. Schulz, B. Mayzel, A. Danilewsky, T. Waterstradt, W. Diete, H. Riesemeier, B. Müller and T. Baumbach, *Nuclear Instruments and Methods in Physics Research Section B: Beam Interactions with Materials and Atoms*, 2009, **267**, 1978 – 1988.

[100] X. R. Huang, *Journal of Applied Crystallography*, 2010, **43**, 926–928.

[101] M. Tachibana, Q. Tang, N. Ide and K. Kojima, *Japanese Journal of Applied Physics*, 1994, **33**, 1995.

[102] Z. Qiang and D. Peizhen, *Materials Letters*, 1989, **8**, 105–108.

[103] J. L. Caslavsky, C. P. Gazzara and R. M. Middleton, *Philosophical Magazine*, 1972, **25**, 35–44.

[104] S. Demina, E. Bystrova, V. Postolov, E. Eskov, M. Nikolenko, D. Marshanin, V. Yuferev and V. Kalaev, *Journal of Crystal Growth*, 2008, **310**, 1443–1447.

[105] B. J. Pletka, T. E. Mitchell and A. H. Heuer, *Journal of the American Ceramic Society*, 1974, **57**, 388–393.

[106] K. P. D. Lagerlöf, B. Pletka, T. E. Mitchell and A. H. Heuer, *Radiation Effects*, 1983, **74**, 87–107.

[107] G. W. Groves and A. Kelly, *Journal of Applied Physics*, 1962, **33**, 456–460.

[108] K. Lagerlöf, J. Castaing and A. Heuer, *Philosophical Magazine*, 2013, **93**, 152–161.

[109] D. S. Phillips, T. E. Mitchell and A. H. Heuer, *Philosophical Magazine A*, 1982, **45**, 371–385.

[110] W. Cai and W. Nix, *Imperfections in Crystalline Solids*, Cambridge University Press, 2016.

[111] D. Hull and D. Bacon, *Introduction to Dislocations*, Elsevier Science, 2001.

[112] K. P. D. Lagerlöf, T. E. Mitchell and A. H. Heuer, *Journal of the American Ceramic Society*, 1989, **72**, 2159–2171.

[113] K. Lagerlöf, T. Mitchell and A. Heuer, *Acta Metallurgica*, 1989, **37**, 3315 – 3325.

[114] J. L. Caslavsky and C. P. Gazzara, *Philosophical Magazine*, 1972, **26**, 961–975.

[115] J. L. Caslavsky and C. P. Gazzara, *Journal of Materials Science*, 1971, **6**, 1139–1141.

[116] J. Weertman, *Phys. Rev.*, 1957, **107**, 1259–1261.

[117] X. Chenghai, M. Songhe, Z. Mingfu, Z. Hongbo and W. Guigen, *Chinese Journal of Aeronautics*, 2007, **20**, 475 – 480.

[118] W. M. Chen, P. J. McNally, Y. V. Shvyd'ko, T. Tuomi, A. N. Danilewsky and M. Lerche, *Journal of Crystal Growth*, 2003, **252**, 113–119.

[119] M. N. Ediger, R. W. Waynant, N. I. Djeu, Y. Shimoji and R. S. F. Chang, 1989, **4**, AP/1–AP/2.

[120] H. Schumacher, T. J. Gmitter, H. P. LeBlanc, R. Bhat, E. Yablonovitch and M. A. Koza, *Electronics Letters*, 1989, **25**, 1653–1654.

[121] F. J. Bruni, *Crystal Research and Technology*, 2015, **50**, 133–142.

[122] J. Hrdý and O. Pacherová, *Nuclear Instruments and Methods in Physics Research Section A: Accelerators, Spectrometers, Detectors and Associated Equipment*, 1993, **327**, 605 – 611.

[123] C. David, J. Bruder, T. Rohbeck, C. Grünzweig, C. Kottler, A. Diaz, O. Bunk and F. Pfeiffer, *Microelectronic Engineering*, 2007, **84**, 1172 – 1177.

[124] Y. Shvyd'ko and E. Gerdau, *Hyperfine Interactions*, 1999, **123**, 741–776.

[125] A. J. Rondinone, C. Y. Jones, S. L. Marshall, B. C. Chakoumakos, C. J. Rawn and E. Lara-Curzio, *Canadian Journal of Physics*, 2003, **81**, 381–385.

[126] J. Kohlbrecher, A. Bollhalder, R. Vavrin and G. Meier, *Review of Scientific Instruments*, 2007, **78**, 125101.

[127] S. Bayya, G. Villalobos, W. Kim, J. Sanghera, M. Hunt and I. D. Aggarwal, *Proc. SPIE*, 2014, **9202**, 92021D.

[128] J. B. Taylor, R. Boland, E. Gowac, P. Stupik and M. Tricard, *Proc. SPIE*, 2013, **8708**, 870816.

[129] S. Tsutsui, Y. Yoda and H. Kobayashi, *Journal of the Physical Society of Japan*, 2007, **76**, 065003.

[130] H.-C. Wille, R. P. Hermann, I. Sergueev, U. Pelzer, A. Möchel, T. Claudio, J. Perßon, R. Rüffer, A. Said and Y. V. Shvyd'ko, *EPL (Europhysics Letters)*, 2010, **91**, 62001.

[131] H.-C. Wille, R. P. Hermann, I. Sergueev, O. Leupold, P. van der Linden, B. C. Sales, F. Grandjean, G. J. Long, R. Rüffer and Y. V. Shvyd'ko, *Phys. Rev. B*, 2007, **76**, 140301.

[132] B. Klobes, A. Desmedt, I. Sergueev, K. Schmalzl and R. P. Hermann, *EPL (Europhysics Letters)*, 2013, **103**, 36001.

[133] E. Dobrovinskaya, L. Lytvynov and V. Pishchik, *Sapphire: Material, Manufacturing, Applications*, Springer US, 2009.

[134] P. Rudolph, *Handbook of Crystal Growth: Bulk Crystal Growth*, Elsevier Science, 2014.

[135] M. S. Akselrod and F. J. Bruni, *Journal of Crystal Growth*, 2012, **360**, 134 – 145.

[136] L. S. Birks, J. W. Hurley and W. E. Sweeney, *Journal of Applied Physics*, 1965, **36**, 3562–3565.

[137] P. M. Adams, *Evaluation of the Quality of Sapphire Using X-Ray Rocking Curves and Double-Crystal X-Ray Topography*, Defense Technical Information Center, 1994.

[138] Y. Wang, S. Liu, G. Peng, S. Zhou and J. Xu, *Journal of Crystal Growth*, 2005, **274**, 241–245.

[139] M. Hart, *Journal of Crystal Growth*, 1981, **55**, 409 – 427.

[140] V. E. Asadchikov, A. V. Butashin, A. V. Buzmakov, A. N. Deryabin, V. M. Kanevsky, I. A. Prokhorov, B. S. Roshchin, Y. O. Volkov, D. A. Zolotov, A. Jafari, P. Alexeev, A. Cecilia, T. Baumbach, D. Bessas, A. N. Danilewsky, I. Sergueev, H.-C. Wille and R. P. Hermann, *Crystal Research and Technology*, 2016, **51**, 290–298.

[141] A. I. Chumakov, A. Barla, R. Rüffer, J. Metge, H. F. Grünsteudel, H. Grünsteudel, J. Plessel, H. Winkelmann and M. M. Abd-Elmeguid, *Phys. Rev. B*, 1998, **58**, 254–257.

[142] B. Tanner, *X-Ray Diffraction Topography: International Series in the Science of the Solid State*, Elsevier Science, 2013.

[143] P. Capper, *Bulk Crystal Growth of Electronic, Optical and Optoelectronic Materials*, Wiley, 2005.

[144] H. Tang, H. Li and J. Xu, *Growth and Development of Sapphire Crystal for LED Applications*, INTECH Open Access Publisher, 2013.

[145] J. P. Ciraldo, J. Levine and H. Ganegoda, *Proc. SPIE*, 2014, **9100**, 91000Q.

[146] J. B. Watchman, W. E. Teffet, D. G. Lam and R. P. Stinchfield, *Journal of the American Ceramic Society*, 1960, **43**, 334–334.

[147] J. H. Gieske and G. R. Barsch, *physica status solidi (b)*, 1968, **29**, 121–131.

[148] Z. Jin, H. Fang, N. Yang, Z. Zhang, S. Wang and J. Xu, *Journal of Crystal Growth*, 2014, **405**, 52–58.

[149] A. Benmeddour and S. Meziani, *Revue des Energies Renouvelables*, 2009, **12**, 575–584.

[150] T. S. Toellner, J. Collins, K. Goetze, M. Y. Hu, C. Preissner, E. Trakhtenberg and L. Yan, *Journal of Synchrotron Radiation*, 2015, **22**, 1155–1162.

[151] A. Authier, *Dynamical Theory of X-ray Diffraction*, Oxford University Press, 2004.

[152] G. G. Wang, M. F. Zhang, H. B. Zou, C. H. Xu, X. D. He and J. C. Han, *Chinese Journal of Structural Chemistry*, 2007, **26**, 1332–1336.

[153] A. D. LaLonde, Y. Pei, H. Wang and G. J. Snyder, *Materials Today*, 2011, **14**, 526 – 532.

[154] G. J. Snyder, *Nature Nanotechnology*, 2008, **7**, 105–114.

[155] Y. Pei, X. Shi, A. LaLonde, L. Chen and G. J. Snyder, *Nature*, 2011, **473**, 66–69.

[156] S. Lin, W. Li, Z. Chen, J. Shen, B. Ge and Y. Pei, *Nature Communications*, 2011, **7**, 66–69.

[157] H. Wang, A. D. LaLonde, Y. Pei and G. J. Snyder, *Advanced Functional Materials*, 2013, **23**, 1586–1596.

[158] S. N. Girard, J. He, C. Li, S. Moses, G. Wang, C. Uher, V. P. Dravid and M. G. Kanatzidis.

[159] Y. Liu, P. Sahoo, J. P. A. Makongo, X. Zhou, S.-J. Kim, H. Chi, C. Uher, X. Pan, Poudeu and F. P. Pierre, *Journal of the American Chemical Society*, 2013, **135**, 7486–7495.

[160] K. F. Hsu, S. Loo, F. Guo, W. Chen, J. S. Dyck, C. Uher, T. Hogan, E. K. Polychroniadis and M. G. Kanatzidis, *Science*, 2004, **303**, 818–821.

[161] S. Perlt, T. Höche, J. Dadda, E. Müller, P. B. Pereira, R. P. Hermann, M. Sarahan, E. Pippel and R. Brydson, *Journal of Solid State Chemistry*, 2012, **193**, 58–63.

[162] S. Perlt, T. Höche, J. Dadda, E. Müller and B. Rauschenbach, *Journal of Electronic Materials*, 2012, **42**, 1422–1428.

[163] J. Dadda, E. Müller, S. Perlt, T. Höche, P. Bauer Pereira and R. P. Hermann, *Journal of Materials Research*, 2011, **26**, 1800–1812.

[164] J. He, J. R. Sootsman, S. N. Girard, J.-C. Zheng, J. Wen, Y. Zhu, M. G. Kanatzidis and V. P. Dravid, *Journal of the American Chemical Society*, 2010, **132**, 8669–8675.

[165] E. Quarez, K.-F. Hsu, R. Pcionek, N. Frangis, E. K. Polychroniadis, and M. G. Kanatzidis, *Journal of the American Chemical Society*, 2005, **127**, 9177–9190.

[166] B. A. Cook, M. J. Kramer, J. L. Harringa, M.-K. Han, D.-Y. Chung and M. G. Kanatzidis, *Advanced Functional Materials*, 2009, **19**, 1254–1259.

[167] C. W. Li, J. Ma, H. B. Cao, A. F. May, D. L. Abernathy, G. Ehlers, C. Hoffmann, X. Wang, T. Hong, A. Huq, O. Gourdon and O. Delaire, *Phys. Rev. B*, 2014, **90**, 214303.

[168] J. Ma, O. Delaire, A. F. May, C. E. Carlton, M. A. McGuire, L. H. VanBebber, D. L. Abernathy, G. Ehlers, T. Hong, A. Huq, W. Tian, V. M. Keppens, Y. Shao-Horn and B. C. Sales, *Nature Nanotechnology*, 2013, **8**, 445–451.

[169] J. Sootsman, R. Pcionek, H. Kong, C. Uher and M. G. Kanatzidis, 2005, **886**, 0886–F08–05.

[170] P. Gütlich, *Mössbauer Spectroscopy and Transition Metal Chemistry*, Springer Berlin Heidelberg, New York, 2011.

[171] P. Bauer Pereira, I. Sergueev, S. Gorsse, J. Dadda, E. Müller and R. P. Hermann, *physica status solidi (b)*, 2013, **250**, 1300–1307.

[172] H. Lin, E. S. Božin, S. J. L. Billinge, E. Quarez and M. G. Kanatzidis, *Phys. Rev. B*, 2005, **72**, 174113.

[173] T. Claudio, D. Bessas, C. S. Birkel, G. Kieslich, M. Panthöfer, I. Sergueev, W. Tremel and R. P. Hermann, *physica status solidi (b)*, 2014, **251**, 919–923.

[174] T. Matsunaga, N. Yamada, R. Kojima, S. Shamoto, M. Sato, H. Tanida, T. Uruga, S. Kohara, M. Takata, P. Zalden, G. Bruns, I. Sergueev, H.-C. Wille, R. P. Hermann and M. Wuttig, *Advanced Functional Materials*, 2011, **21**, 2232–2239.

[175] S. Lee, K. Esfarjani, T. Luo, J. Zhou, Z. Tian and G. Chen, *Nat. Commun.*, 2014, **5**, 3525.

[176] A. Möchel, I. Sergueev, N. Nguyen, G. J. Long, F. Grandjean, D. C. Johnson and R. P. Hermann, *Phys. Rev. B*, 2011, **84**, 064302.

[177] W. Kim and A. Majumdar, *Journal of Applied Physics*, 2006, **99**, 084306.

[178] R. M. Bozorth, *Journal of the American Chemical Society*, 1923, **45**, 1621–1627.

[179] M. Buerger and S. Hendricks, *Zeitschrift für Kristallogr*, 1938, **98**, 1–6.

[180] B. Naidu, M. Pandey, V. Sudarsan, R. Vatsa and R. Tewari, *Chemical Physics Letters*, 2009, **474**, 180–184.

[181] D. E. Kokkalas, D. N. Bikiaris and G. P. Karayannidis, *Journal of Applied Polymer Science*, 1995, **55**, 787–791.

[182] M. Nalin, Y. Messaddeq, S. J. L. Ribeiro, M. Poulain, V. Briois, G. Brunklaus, C. Rosenhahn, B. D. Mosel and H. Eckert, *J. Mater. Chem.*, 2004, **14**, 3398–3405.

[183] D. W. Hall, M. A. Newhouse, N. F. Borrelli, W. H. Dumbaugh and D. L. Weidman, *Applied Physics Letters*, 1989, **54**, 1293–1295.

[184] A. Chagraoui, I. Yakine, A. Tairi, A. Moussaoui, M. Talbi and M. Naji, *Journal of Materials Science*, 2011, **46**, 5439–5446.

[185] P. Petkova, M. T. Soltani, S. Petkov, J. Tacheva and V. Nedkov, *Physica Scripta*, 2012, **2012**, 014057.

[186] A. S. Pine and G. Dresselhaus, *Phys. Rev. B*, 1972, **5**, 4087–4093.

[187] M. Ceriotti, F. Pietrucci and M. Bernasconi, *Phys. Rev. B*, 2006, **73**, 104304.

[188] J. Cornette, T. Merle-Méjean, A. Mirgorodsky, M. Colas, M. Smirnov, O. Masson and P. Thomas, *Journal of Raman Spectroscopy*, 2011, **42**, 758–764.

[189] R. G. Orman, *PhD thesis*, University of Warwick, Coventry, England, 2005.

[190] D. Orosel, R. E. Dinnebier, V. A. Blatov and M. Jansen, *Acta Crystallographica Section B*, 2012, **68**, 1–7.

[191] V. L. Deringer, R. P. Stoffel and R. Dronskowski, *Crystal Growth and Design*, 2014, **14**, 871–878.

[192] I. R. Beattie and G. A. Ozin, *J. Chem. Soc. A*, 1970, 370–377.

[193] R. Konings, A. Booij and E. Cordfunke, *Chemical Physics Letters*, 1993, **210**, 380–383.

[194] G. Mestl, P. Ruiz, B. Delmon and H. Knozinger, *The Journal of Physical Chemistry*, 1994, **98**, 11276–11282.

[195] I. Degen and G. Newman, *Spectrochimica Acta Part A: Molecular Spectroscopy*, 1993, **49**, 859–887.

[196] I. R. Beattie, K. M. S. Livingston, G. A. Ozin and D. J. Reynolds, *J. Chem. Soc. A*, 1970, 449–451.

[197] A. L. J. Pereira, L. Gracia, D. Santamaría-Pérez, R. Vilaplana, F. J. Manjón, D. Errandonea, M. Nalin and A. Beltrán, *Phys. Rev. B*, 2012, **85**, 174108.

[198] S. Bahfenne and R. L. Frost, *Spectroscopy Letters*, 2010, **43**, 486–490.

[199] S. J. Gilliam, J. O. Jensen, A. Banerjee, D. Zeroka, S. J. Kirkby and C. N. Merrow, *Spectrochimica Acta Part A: Molecular and Biomolecular Spectroscopy*, 2004, **60**, 425–434.

[200] P. A. Thomas, *Journal of Physics C: Solid State Physics*, 1988, **21**, 4611.

[201] A. Mirgorodsky, T. Merle-Méjean, J.-C. Champarnaud, P. Thomas and B. Frit, *Journal of Physics and Chemistry of Solids*, 2000, **61**, 501–509.

[202] S. Blanchandin, P. Marchet, P. Thomas, J. C. Champarnaud-Mesjard, B. Frit and A. Chagraoui, *Journal of Materials Science*, 1999, **34**, 4285–4292.

[203] N. Berkaïne, E. Orhan, O. Masson, P. Thomas and J. Junquera, *Phys. Rev. B*, 2011, **83**, 245205.

[204] R. El-Mallawany, *Tellurite Glasses Handbook: Physical Properties and Data, Second Edition*, CRC Press, 2016.

[205] V. Rodriguez, M. Couzi, F. Adamietz, M. Dussauze, G. Guery, T. Cardinal, P. Veber, K. Richardson and P. Thomas, *Journal of Raman Spectroscopy*, 2013, **44**, 739–745.

[206] M. Vuković, Z. Branković, D. Poleti, A. Rečnik and G. Branković, *Journal of Sol-Gel Science and Technology*, 2014, **72**, 527–533.

[207] P. E. Blöchl, *Phys. Rev. B*, 1994, **50**, 17953–17979.

[208] G. Kresse and J. Hafner, *Phys. Rev. B*, 1993, **47**, 558–561.

[209] G. Kresse and J. Furthmüller, *Phys. Rev. B*, 1996, **54**, 11169–11186.

[210] G. Kresse and J. Furthmüller, *Computational Materials Science*, 1996, **6**, 15–50.

[211] G. Kresse and D. Joubert, *Phys. Rev. B*, 1999, **59**, 1758–1775.

[212] G. G. Long and L. Bowen, *Inorganic and Nuclear Chemistry Letters*, 1970, **6**, 837–842.

[213] P. Lippens, *Solid State Communications*, 2000, **113**, 399 – 403.

[214] G. K. Semin, T. A. Babushkina and G. G. Yakobson, *Quadrupole Resonance in Chemistry*, srael Program for Scientific Translations-John Wiley and Sons, 1975.

[215] M. Takeda, M. Takahashi, R. Ohyama and I. Nakai, *Hyperfine Interactions*, 1986, **28**, 741–744.

[216] K. S. Singwi and A. Sjölander, *Phys. Rev.*, 1960, **120**, 1093–1102.

[217] M. Hu, W. Sturhahn, T. Toellner, P. Hession, J. Sutter and E. Alp, *Nuclear Instruments and Methods in Physics Research Section A: Accelerators, Spectrometers, Detectors and Associated Equipment*, 1999, **428**, 551 – 555.

[218] M. Barucci, C. Brofferio, A. Giuliani, E. Gottardi, I. Peroni and G. Ventura, *Journal of Low Temperature Physics*, 2001, **123**, 303–314.

[219] E. Boldyreva and P. Dera, *High-Pressure Crystallography: From Fundamental Phenomena to Technological Applications*, Springer Netherlands, 2010.

[220] T. G. Worlton and R. A. Beyerlein, *Phys. Rev. B*, 1975, **12**, 1899–1907.

[221] P. McMillan, *American Mineralogist*, 1984, **69**, 622–644.

[222] R. P. Stoffel, V. L. Deringer, R. E. Simon, R. P. Hermann and R. Dronskowski, *Journal of Physics: Condensed Matter*, 2015, **27**, 085402.

[223] A. I. Chumakov, R. Rüffer, O. Leupold and I. Sergueev, *Structural Chemistry*, 2003, **14**, 109–119.

[224] H. Ogi, M. Fukunaga, M. Hirao and H. Ledbetter, *Phys. Rev. B*, 2004, **69**, 024104.

[225] A. Matsumoto, Y. Koyama, A. Togo, M. Choi and I. Tanaka, *Phys. Rev. B*, 2011, **83**, 214110.

[226] B. Sanyasinaidu, *PhD thesis*, Homi Bhabha National Institute, Mumbai, India, 2012.

[227] W. W. Cochran, *The dynamics of atoms in crystals*, New York : Crane, Russak, 1973.

[228] M. Hamzaoui, S. Azri, M. T. Soltani, R. Lebullenger and M. Poulain, *Physica Scripta*, 2013, **2013**, 014029.

[229] R. El-Mallawany and G. Saunders, *Journal of Materials Science Letters*, 1987, **6**, 443–446.

[230] C. Arnaboldi, C. Brofferio, A. Bryant, C. Bucci, L. Canonica, S. Capelli, M. Carrettoni, M. Clemenza, I. Dafinei, S. D. Domizio, F. Ferroni, E. Fiorini, Z. Ge, A. Giachero, L. Gironi, A. Giuliani, P. Gorla, E. Guardincerri, R. Kadel, K. Kazkaz, L. Kogler, Y. Kolomensky, J. Larsen, M. Laubenstein, Y. Li, C. Maiano, M. Martinez, R. Maruyama, S. Nisi, C. Nones, E. B. Norman, A. Nucciotti, F. Orio, L. Pattavina, M. Pavan, G. Pessina, S. Pirro, E. Previtali, C. Rusconi, N. D. Scielzo, M. Sisti, A. R. Smith, W. Tian, M. Vignati, H. Wang and Y. Zhu, *Journal of Crystal Growth*, 2010, **312**, 2999 – 3008.